

---

# Dissertation

submitted to the

**Combined Faculties of the Natural Sciences and Mathematics of  
the Ruperto-Carola-University of Heidelberg, Germany**

for the degree of

**Doctor of Natural Sciences**

---

Put forward by

**Dipl.-Phys. Felix Nendzig**

born in Berlin

Oral examination:  
February the 5th, 2014



# A model for the suppression of $\Upsilon$ mesons in PbPb collisions at LHC energies

Referees:

Prof. Dr. Georg Wolschin

Priv.-Doz. Dr. Klaus Reygers



## Zusammenfassung:

Es wird ein Modell für die Unterdrückung von  $\Upsilon$ -Mesonen im Quark-Gluon Plasma (QGP) vorgestellt, welches in relativistischen PbPb-Kollisionen am LHC gebildet wird. Das Modell berücksichtigt die sechs Bottomium-Zustände  $\Upsilon(nS)$ ,  $\chi_b(nP)$  mit  $n = 1, 2, 3$  und ist in drei Schritte unterteilt: Zunächst werden die Wellenfunktionen und Zerfallsbreiten im Medium in einem nichtrelativistischen, komplexen Potenzialmodell berechnet. Auf diese Weise werden die folgenden drei Prozesse berücksichtigt: Abschirmung der Farbladung, Dämpfung durch weiche Kollisionen und Gluodissoziation. Im zweiten Schritt wird eine numerische, hydrodynamische Berechnung der longitudinalen und transversalen Expansion des Feuerballs durchgeführt, wobei das QGP als ideales, relativistisches Fluid behandelt wird. Durch Einsetzen der Ergebnisse aus Schritt Eins erhält man die QGP-Unterdrückungsfaktoren  $R_{AA}^{\text{QGP}}$ , die für jeden der sechs Zustände den Anteil angeben, der den Feuerball überlebt hat. In Schritt Drei wird für die verbliebene Bottomium-Population die Zerfallskaskade innerhalb der Bottomium-Familie und in Dimuonpaare berechnet. Daraus ergeben sich die Unterdrückungsfaktoren  $R_{AA}$  der  $\Upsilon(nS)$  Mesonen. Für eine realistische Wahl der Parameter stimmt das Modell gut mit den CMS-Ergebnissen des PbPb-Runs vom November 2011 überein. Es zeigt sich jedoch, dass die Unterdrückung der angeregten Zustände  $\Upsilon(2S)$  und  $\Upsilon(3S)$ , im Vergleich zum Grundzustand  $\Upsilon(1S)$ , in diesem Modell nicht stark genug ausfällt. Es müssen daher weitere Mechanismen berücksichtigt werden, die die  $\Upsilon(nS)/\Upsilon(1S)$ -Verhältnisse modifizieren.

## Abstract:

A model for the suppression of  $\Upsilon$  mesons in the quark-gluon plasma (QGP), formed in relativistic PbPb collisions at the LHC, is presented. The model takes the six bottomium states  $\Upsilon(nS)$ ,  $\chi_b(nP)$  with  $n = 1, 2, 3$  into account and consists of three steps: First the in-medium wave functions and decay widths are calculated from a non-relativistic, complex potential model. In this approach the following three processes are taken into account: color screening, collisional damping and gluodissociation. In the second step a numerical, hydrodynamical calculation of the longitudinally and transversely expanding fireball is performed, where the QGP is modeled as a perfect, relativistic fluid. Inserting the results of step one yields QGP-suppression factors  $R_{AA}^{\text{QGP}}$ , which give for each of the six states the fraction that has survived the fireball. In step three the decay cascade is calculated for the remaining bottomium population for decays within the bottomium family and into dimuon pairs. This yields the final results for the suppression factors  $R_{AA}$  of the  $\Upsilon(nS)$  mesons. It is found that the model is in good agreement with the CMS results for the November 2011 PbPb run for a reasonable choice of parameters. However, the calculated suppression of the excited states  $\Upsilon(2S)$  and  $\Upsilon(3S)$  relative to the ground state  $\Upsilon(1S)$  is not strong enough in this model. Additional mechanisms have to be taken into account to modify the  $\Upsilon(nS)/\Upsilon(1S)$  ratios.



*Devoted to Simone, the love and light of my life.*



# Contents

<b>Contents</b>	<b>ix</b>
<b>List of Figures</b>	<b>xi</b>
<b>List of Tables</b>	<b>xiii</b>
<b>Nomenclature</b>	<b>xv</b>
<b>1 Introduction</b>	<b>1</b>
1.1 QCD and the quark-gluon plasma . . . . .	3
1.2 The bottomium family . . . . .	6
1.3 Theoretical outline, experimental input . . . . .	8
<b>2 Theoretical foundations</b>	<b>11</b>
2.1 Quantum chromodynamics . . . . .	11
2.2 Thermal modifications . . . . .	15
2.3 NRQCD and pNRQCD . . . . .	17
2.4 The long-time interaction potential . . . . .	22
<b>3 Dissociation of bottomium</b>	<b>27</b>
3.1 Bound state bottomium wave functions . . . . .	27
3.2 Gluodissociation of the Upsilon meson . . . . .	34
3.2.1 Dissociation of bottomia in the medium . . . . .	35
3.2.2 Gluodissociation at finite temperature . . . . .	41
3.2.3 Gluodissociation of pure Coulomb states . . . . .	43
<b>4 Relativistic hydrodynamics</b>	<b>49</b>
4.1 The fluid equations of motion . . . . .	49
4.2 The longitudinally co-moving frame . . . . .	52
4.3 The numerical approach . . . . .	55
4.4 The initial conditions . . . . .	60

<b>5</b>	<b>Upsilon suppression at the LHC</b>	<b>67</b>
5.1	Suppression in the quark-gluon plasma . . . . .	67
5.2	The decay cascade . . . . .	77
<b>6</b>	<b>Results and conclusions</b>	<b>85</b>
6.1	Theoretical results . . . . .	85
6.2	Comparison with other work . . . . .	88
6.3	Summary and conclusions . . . . .	92
	<b>Acknowledgments</b>	<b>95</b>
<b>A</b>	<b>Basic thermal field theory</b>	<b>97</b>
A.1	Thermal propagators . . . . .	97
A.2	The polarization tensor . . . . .	100
<b>B</b>	<b>Data tables</b>	<b>103</b>
B.1	Results from the potential model . . . . .	103
B.2	Suppression factors and double ratios . . . . .	106
	<b>Bibliography</b>	<b>115</b>

# List of Figures

3.1	Complex bottomium interaction potential . . . . .	31
3.2	Radial wave functions of the $\Upsilon(1S)$ , $\Upsilon(2S)$ , $\Upsilon(3S)$ . . . . .	31
3.3	Comparison of the high and low temperature potentials . . . . .	33
3.4	Comparison of different scales in the potential model . . . . .	33
3.5	Binding energies and rms radii as a function of temperature . . . . .	34
3.6	Singlet-octet transition . . . . .	37
3.7	Finite temperature gluodissociation cross section . . . . .	42
3.8	Partial decay widths $\Gamma_{\text{damp}}$ and $\Gamma_{\text{diss}}$ . . . . .	43
3.9	Overlap of the cross section with the gluon distribution . . . . .	44
3.10	Total decay width $\Gamma_{\text{tot}} = \Gamma_{\text{damp}} + \Gamma_{\text{diss}}$ . . . . .	45
3.11	Gluodissociation cross section for Coulomb states . . . . .	48
4.1	Coordinate system for PbPb collisions . . . . .	53
4.2	Staggered grid used in the hydrodynamical calculation . . . . .	57
4.3	Profiles of the temperature in the fireball . . . . .	63
4.4	Profiles of the transverse velocity in the fireball . . . . .	64
5.1	Anisotropic temperature $T'_{\text{eff}}(v, \theta)$ . . . . .	70
5.2	Profiles of $T$ and $T_{\text{eff},10}$ for different $p_T$ . . . . .	72
5.3	Profiles of $\Upsilon(1S)$ -damping factor $D_{10}$ and $T_{AA}D_{10}$ . . . . .	73
5.4	Two-dimensional profiles of $T_{AA}D_{10}$ and $T_{AA}D_{20}$ . . . . .	75
5.5	QGP-suppression factors $R_{AA}^{\text{QGP}}$ for the $\Upsilon(1S)$ . . . . .	76
5.6	QGP-suppression factors $R_{AA}^{\text{QGP}}$ for the different bottomium states . . . . .	78
5.7	Decays channels within the bottomium family and into dimuon pairs . . . . .	80
6.1	Results for $R_{AA}(\Upsilon(1S))$ compared with experimental data . . . . .	86
6.2	Results for $R_{AA}(\Upsilon(2S))$ compared with experimental data . . . . .	87
6.3	Results for $\frac{\Upsilon(2S)/\Upsilon(1S) _{\text{PbPb}}}{\Upsilon(2S)/\Upsilon(1S) _{\text{pp}}}$ compared with experimental data . . . . .	88
6.4	Results for $R_{AA}(\Upsilon(3S))$ . . . . .	91

6.5	Results for $\frac{\Upsilon(3S)/\Upsilon(1S) _{\text{PbPb}}}{\Upsilon(3S)/\Upsilon(1S) _{\text{pp}}}$ . . . . .	92
6.6	Results for $R_{AA}(\Upsilon(1S))$ as a function of $p_T$ . . . . .	93
A.1	Contour for the thermal propagator . . . . .	98

# List of Tables

1.1	Masses of charmonia and bottomia . . . . .	6
3.1	Melting temperatures $T_m$ of the different bottomium states . .	35
4.1	Behavior of thermodynamical quantities under reflections . . .	59
4.2	Centrality bins with boundaries and averaged $N_{\text{coll}}$ and $N_{\text{part}}$ .	61
5.1	Entries of the CD matrix $\mathcal{C}$ . . . . .	82
6.1	Minimum bias results for IC1 . . . . .	89
6.2	Minimum bias results for IC2 . . . . .	90
B.1	Data on the $\Upsilon(1S)$ from the potential model at low $T$ . . . . .	103
B.2	Data on the $\Upsilon(1S)$ from the potential model at high $T$ . . . .	103
B.3	Data on the $\chi_b(1P)$ from the potential model . . . . .	105
B.4	Data on the $\Upsilon(2S)$ from the potential model . . . . .	105
B.5	Data on the $\chi_b(2P)$ from the potential model . . . . .	106
B.6	Data on the $\Upsilon(3S)$ from the potential model . . . . .	106
B.7	Data on the $\chi_b(3P)$ from the potential model . . . . .	106
B.8	Final results as functions of centrality using IC1, $T_0 = 550$ MeV, $\tau_{nl} = 0.1 \text{ fm}/c$ . . . . .	106
B.9	Final results as functions of centrality using IC1, $T_0 = 550$ MeV, $\tau_{nl} = 0.5 \text{ fm}/c$ . . . . .	107
B.10	Final results as functions of centrality using IC1, $T_0 = 650$ MeV, $\tau_{nl} = 0.1 \text{ fm}/c$ . . . . .	107
B.11	Final results as functions of centrality using IC1, $T_0 = 650$ MeV, $\tau_{nl} = 0.5 \text{ fm}/c$ . . . . .	108
B.12	Final results as functions of centrality using IC2, $T_0 = 550$ MeV, $\tau_{nl} = 0.1 \text{ fm}/c$ . . . . .	108
B.13	Final results as functions of centrality using IC2, $T_0 = 550$ MeV, $\tau_{nl} = 0.5 \text{ fm}/c$ . . . . .	108

B.14	Final results as functions of centrality using IC2, $T_0 = 650$ MeV, $\tau_{nl} = 0.1$ fm/ $c$ . . . . .	109
B.15	Final results as functions of centrality using IC2, $T_0 = 650$ MeV, $\tau_{nl} = 0.5$ fm/ $c$ . . . . .	109
B.16	Final results as functions of $p_T$ using IC1, $T_0 = 550$ MeV, $\tau_{nl} = 0.1$ fm/ $c$ . . . . .	109
B.17	Final results as functions of $p_T$ using IC1, $T_0 = 550$ MeV, $\tau_{nl} = 0.5$ fm/ $c$ . . . . .	110
B.18	Final results as functions of $p_T$ using IC1, $T_0 = 650$ MeV, $\tau_{nl} = 0.1$ fm/ $c$ . . . . .	110
B.19	Final results as functions of $p_T$ using IC1, $T_0 = 650$ MeV, $\tau_{nl} = 0.5$ fm/ $c$ . . . . .	111
B.20	Final results as functions of $p_T$ using IC2, $T_0 = 550$ MeV, $\tau_{nl} = 0.1$ fm/ $c$ . . . . .	111
B.21	Final results as functions of $p_T$ using IC2, $T_0 = 550$ MeV, $\tau_{nl} = 0.5$ fm/ $c$ . . . . .	112
B.22	Final results as functions of $p_T$ using IC2, $T_0 = 650$ MeV, $\tau_{nl} = 0.1$ fm/ $c$ . . . . .	112
B.23	Final results as functions of $p_T$ using IC2, $T_0 = 650$ MeV, $\tau_{nl} = 0.5$ fm/ $c$ . . . . .	113

# Nomenclature

ALICE .....	A Large Ion Collider Experiment
ATLAS .....	A Toroidal LHC Apparatus
BNL .....	Brookhaven National Laboratory
BRAHMS .....	Broad Range Hadron Magnetic Spectrometers Experiment at RHIC
CD .....	Cumulative decay
CDF .....	Collider Detector at Fermilab
CERN .....	Conseil Européen pour la Recherche Nucléaire
CM .....	Center of mass
CMS .....	Compact Muon Solenoid
CNM .....	Cold nuclear matter
EFT .....	Effective field theory
HTL .....	Hard thermal loop
IC1 .....	Initial condition 1
IC2 .....	Initial condition 2
LCF .....	Longitudinally co-moving frame
LF .....	Laboratory frame
LHC .....	Large Hadron Collider
LQCD .....	Lattice QCD
NLO .....	Next-to-leading order
NRQCD .....	Non-relativistic QCD
NRQED .....	Non-relativistic QED
PDG .....	Particle data group
PHENIX .....	Pioneering High Energy Nuclear Interaction Experiment
pNRQCD .....	Potential NRQCD
pQCD .....	Perturbative QCD
QCD .....	Quantum chromodynamics

QED .....	Quantum electrodynamics
QGP .....	Quark-gluon plasma
RHIC .....	Relativistic Heavy Ion Collider
RM .....	Relative motion
rms .....	Root-mean-square
SBS .....	Strong binding scenario
SLAC .....	Stanford Linear Accelerator Center
SPS .....	Super Proton Synchrotron
STAR .....	Solenoidal Tracker at RHIC
WBS .....	Weak binding scenario

# Chapter 1

## Introduction

In this thesis we take the unique window of opportunity that has opened up with the energies available at the CERN Large Hadron Collider (LHC) to combine the physics of the bottomium states with the physics of the quark-gluon plasma (QGP) in a theoretical investigation.

Ever since the results from the CERN Super Proton Synchrotron (SPS) and the BNL Relativistic Heavy Ion Collider (RHIC) it has been clear that, for a very short interval of time, a new state of matter can be formed in relativistic heavy ion collisions, “whose description in terms of simple hadronic degrees of freedom is inappropriate” (Back et al., 2005).

This state of matter, which apparently consists of individual quarks and gluons, is commonly referred to as “quark-gluon plasma” even though many of its properties have not been anticipated or are yet unknown.

With the start of the heavy ion program of the LHC it was therefore a natural step to bring the investigation of this extreme state of matter to a new level. While AuAu runs had been conducted with a center-of-mass (CM) energy per nucleon-nucleon pair of up to  $\sqrt{s_{NN}} = 200$  GeV at RHIC, two PbPb runs have been conducted within the LHC’s heavy ion program at  $\sqrt{s_{NN}} = 2.76$  TeV in November 2010 and 2011, respectively. Further PbPb runs at the maximum CM energy of  $\sqrt{s_{NN}} = 5.5$  TeV are scheduled for the year 2015.

One of the cleanest probes for the properties of the QGP is the suppressed yield of quarkonia, heavy quark-antiquark bound states. Quarkonia, and especially bottomia, are very tightly bound so a fraction of them can survive even the QGP-phase.

The resulting suppression pattern can be measured experimentally but it is also calculable in theory. In this way it is possible to obtain an insight into the strange and very poorly understood behavior of matter under these extreme conditions.

While charmonium suppression has been studied extensively in the past as a signature for the presence of a QGP, it has not been possible to do so for the much heavier and more suitable bottomium. Only with the energies available at the LHC it is now for the first time possible to study the suppression of individual bottomium states in relativistic heavy ion collisions.

In this thesis we combine the theoretical description of bottomia and the QGP with the most recent results from the LHC experiments ALICE and CMS in a phenomenological model to calculate the suppression pattern of bottomia, in particular of the  $\Upsilon$  mesons, in PbPb collisions.

This thesis is organized as follows: In the remainder of this introductory chapter we provide a bit more information on the properties of bottomia and the QGP and outline the model for the calculation of  $\Upsilon$  suppression at the LHC.

In chapter 2 we elucidate the theoretical background needed to treat bottomia immersed in a thermal medium. We review basic properties of the theory of quantum chromodynamics (QCD), illustrate the transition from the full theory to the effective field theories (EFT's) of non-relativistic QCD (NRQCD) and potential non-relativistic QCD (pNRQCD) and further to the special case of heavy bottom-antibottom states in a thermal background medium.

In chapter 3 we employ a potential model, using the finite-temperature pNRQCD potentials augmented by some phenomenological input, to calculate the bottomium wave functions and decay widths in the medium. The complex potential model incorporates the effects of color screening and collisional damping, while the effect of gluodissociation is accounted for in a perturbative calculation.

In chapter 4 a numerical, hydrodynamical calculation is presented to simulate the evolution of temperature and expansion velocity of the fireball formed in relativistic heavy ion collisions.

In chapter 5 we combine the results of chapter 4 with the in-medium decay widths of chapter 3 to calculate QGP-suppression factors  $R_{AA}^{\text{QGP}}$ . The QGP-suppression factors give the amount of suppression of the individual bottomium states within the fireball. Subsequently a decay cascade calculation is performed for the remaining bottomium population, taking into account decays within the bottomium family and into dimuon pairs.

The final suppression factors  $R_{AA}$  for the amount of  $\Upsilon$  suppression are presented in chapter 6, where they are compared to the most recent results of ALICE and CMS. We summarize and critically review the results, compare with current literature and give an overview of future questions and challenges.

## 1.1 QCD and the quark-gluon plasma

In this thesis we investigate the properties of the strong interaction, which acts on the six quark flavors of the three generations and binds them into hadrons. Quantum chromodynamics is the accepted theory of this strong interaction. On the other hand, QCD predicts quite exotic states of matter to be formed under extreme conditions.

The theory of QCD has been inspired by its prototype quantum electrodynamics (QED), the most accurate physical theory known today. QCD is a gauge theory like QED but with the gauge group  $SU(3)$  instead of  $U(1)$ . The non-abelian nature of the gauge group  $SU(3)$  gives QCD a much richer structure and is the origin of a whole new range of phenomena which are not present in QED.

The QCD interaction is mediated by eight different species of gluons, which couple to three different types of “color charge”. Quarks carry one type of color charge, antiquarks carry anticolor charge and gluons carry color and anticolor charge, respectively. The large coupling strength and the fact that gluons carry color charge themselves makes QCD processes very diverse and complicated and theoretical calculations very involved but all the more interesting.

QCD is backed up by many experiments, both qualitatively and quantitatively, but due to theoretical and experimental complications the accuracy of QED is by far not achieved.

A key aspect of QCD is the running of the coupling strength with the momentum exchange in the interaction process. At low energies, or over large distances, the gluons couple to color charges very strongly so that all quarks and gluons are confined in the very tightly bound, color neutral hadronic states of mesons and baryons (Wilson, 1974). It is due to this fact that no individual quarks and gluons have been observed so far.

With increasing momentum exchange, corresponding to decreasing distance scales, however, the coupling strength increases. Hence, in high-energy processes the coupling is very weak and quarks and gluons behave nearly like free particles; a phenomenon called “asymptotic freedom” (Gross and Wilczek, 1973; Politzer, 1973; ’t Hooft, 1985).

Asymptotic freedom suggests that in an environment with sufficiently high energy density the color force becomes too weak to bind quarks and gluons into hadrons. Hence every hadronic medium should undergo a phase transition at some critical temperature  $T_c$  above which hadrons are dissolved and individual quarks and gluons constitute the degrees of freedom of the medium.

Such an exotic, partonic state of matter could be formed under high

pressure and low temperature in the interior of a compact star or under high pressure and high temperature in the early universe or in the fireball created in relativistic heavy ion collisions.<sup>1</sup> The last alternative is the one considered in this thesis and obviously the only one currently accessible by laboratory experiments.

Naively one would expect that this new state of matter would resemble a gas of weakly interacting quarks and gluons and as such would constitute the chromodynamical analogue of an ordinary, electromagnetic plasma: the quark-gluon plasma (Collins and Perry, 1975).

The results obtained from heavy ion collision experiments at RHIC have indeed pointed to the formation of a new state of matter with partonic degrees of freedom (Adams et al., 2005; Adcox et al., 2005; Arsene et al., 2005; Back et al., 2005). Early results from the LHC experiments ALICE, ATLAS and CMS confirm the formation of a partonic state in PbPb collisions at  $\sqrt{s_{NN}} = 2.76$  TeV (Aamodt et al., 2010a,b; Aamodt et al., 2011a; Aad et al., 2010; Chatrchyan et al., 2011).

Despite some analogs it is clear that the QGP has also quite different properties from an ordinary plasma due the peculiar nature of the strong interaction. In particular experimental results indicate a strongly interacting medium, which reaches thermal equilibrium within less than  $\lesssim 1$  fm/ $c$  and is surprisingly well described by perfect-fluid hydrodynamics as opposed to the expected gas of quasi-free quarks and gluons.

The LHC data are compatible with lattice QCD (LQCD) results from the HotQCD and RBC-Bielefeld collaborations, who predict the phase transition to occur at the critical temperature

$$\begin{aligned} T_c &= 154 \pm 9 \text{ MeV} && \text{(Bazavov et al., 2012),} \\ T_c &= 192 \pm 7 \pm 4 \text{ MeV} && \text{(Cheng et al., 2006).} \end{aligned} \quad (1.1)$$

Throughout this thesis we will use

$$T_c = 170 \text{ MeV}. \quad (1.2)$$

A number of different observables exist to verify the formation of a QGP in heavy ion collisions (the following list is not complete, see e.g. Yagi et al., 2008; Reygers, 2012, and references therein):

- Charged particle multiplicity at mid-rapidity provides a measure for the initial energy density  $\varepsilon$ , which is found to be well in excess of the critical energy density corresponding to  $T_c$ .

---

<sup>1</sup>Cold partonic matter should have properties quite different from hot partonic matter of course; not to mention the effect of strong spacetime curvature present in neutron stars as well as fast rotation (pulsars) or strong magnetic fields (magnetars).

- Transverse momentum spectra for particles of different mass reveal signatures of collective flow, well described by hydrodynamical models of the QGP.
- Jet quenching, i.e. energy loss of partons produced in hard scattering processes, provides a hard probe to determine properties of the QGP.
- Modified yields of quarkonia in heavy ion collisions as compared to the expectation from scaled yields in nucleon-nucleon collisions indicate the presence of a QGP.

We see that a lot of evidence points to the formation of a QGP. However, as already mentioned there are many experimental and theoretical difficulties in understanding the QGP so many questions remain unanswered about the properties of this very exotic state of matter.

Both quarkonia and jets are hard probes, i.e. they can only be produced in the early collision phase due to the large energies required. This makes them an ideal probe; first because the QGP is not yet formed at this point and second, because perturbative QCD (pQCD) is reliable in these hard processes.

The nuclear suppression factor  $R_{AA}$  quantifies the amount of quarkonium suppression in collisions of heavy ions with mass number  $A$ . It compares the yield  $N_{AA}(b)$  measured in heavy ion collisions with impact parameter  $b$  with the yield  $N_{NN}$  in nucleon-nucleon collisions, scaled with the number of binary collisions  $N_{\text{coll}}(b)$ ,

$$R_{AA} = \frac{N_{AA}(b)}{N_{NN}N_{\text{coll}}(b)}. \quad (1.3)$$

Charmonium suppression has been studied since 1986 in great detail both theoretically (Patra and Srivastava, 2001; Kharzeev, 2007; Kluberg and Satz, 2010) and experimentally at energies reached at the CERN SPS (Abreu et al., 2000), BNL RHIC (Atomssa et al., 2009) and at the CERN LHC (Silvestre et al., 2011; Aamodt et al., 2011a).

The suppression of individual bottomium states in relativistic PbPb collisions at the LHC has been measured recently for the first time by the CMS experiment (Khachatryan et al., 2011; Chatrchyan et al., 2011, 2012).

The model presented in this thesis investigates only the suppression of bottomia since they represent a much cleaner probe for the properties of the QGP. Before we continue to outline the model, however, we review some basic properties of the bottomium family in the next section.

Table 1.1: Masses of charmonia (left) and bottomia (right) and the lightest open charm and bottom mesons as given by the PDG (Beringer et al., 2012).

State	Mass (MeV)	State	Mass (MeV)
$J/\psi(1S)$	$3096.916 \pm 0.011$	$\Upsilon(1S)$	$9460.30 \pm 0.26$
$\chi_{c0}(1P)$	$3414.75 \pm 0.31$	$\chi_{b0}(1P)$	$9859.44 \pm 0.42 \pm 0.31$
$\chi_{c1}(1P)$	$3510.66 \pm 0.07$	$\chi_{b1}(1P)$	$9892.78 \pm 0.26 \pm 0.31$
$\chi_{c2}(1P)$	$3556.20 \pm 0.09$	$\chi_{b2}(1P)$	$9912.21 \pm 0.26 \pm 0.31$
$\psi(2S)$	$3686.109 \pm 0.014$	$\Upsilon(2S)$	$10023.26 \pm 0.31$
$D^0$	$1864.86 \pm 0.13$	$\chi_{b0}(2P)$	$10232.5 \pm 0.4 \pm 0.5$
$D^\pm$	$1869.62 \pm 0.15$	$\chi_{b1}(2P)$	$10255.46 \pm 0.22 \pm 0.50$
		$\chi_{b2}(2P)$	$10268.65 \pm 0.22 \pm 0.50$
		$\Upsilon(3S)$	$10355.2 \pm 0.5$
		$\chi_b(3P)$	$10534 \pm 9$
		$\Upsilon(4S)$	$10579.4 \pm 1.2$
		$B^\pm$	$5279.26 \pm 0.17$
		$B^0$	$5279.58 \pm 0.17$

## 1.2 The bottomium family

Quarkonium mesons consist of a heavy quark-antiquark pair, i.e.  $b\bar{b}$  (bottom-antibottom) for bottomia or  $c\bar{c}$  (charm-anticharm) for charmonia. The  $J/\psi$ , a charmonium with a mass of  $\sim 3.1$  GeV, was the first quarkonium to be discovered simultaneously at the SLAC National Accelerator Laboratory (Augustin et al., 1974) and the BNL (Aubert et al., 1974). The first bottomium to be observed was the  $\Upsilon(1S)$  meson. It was discovered only three years later at Fermilab, having a mass of roughly  $\sim 9.5$  GeV (Herb et al., 1977). The top quark was discovered in 1994 by the CDF experiment with the Tevatron at Fermilab (Abe et al., 1994). Unfortunately the top decays too fast to form bound states so there are no toponia to probe the QGP. Up-to-date masses of charmonia and bottomia as given by the particle data group (PDG) are summarized in table 1.1.

In following we will concentrate on the bottomium family but the charmonium family is structured very similarly. The lightest bottom-flavored mesons are the  $B^\pm$  mesons, where the mass of a  $B^+B^-$  pair is larger than the  $\Upsilon(1S)$  mass by  $\sim 1100$  MeV. Analogous to QED bound states, this mass gap can be thought of as some kind of binding energy in the sense that this amount of energy has to be invested into the system to separate the heavy  $b\bar{b}$  pair to infinity. The analogy should not be taken too serious, however, because the nature of the strong interaction would prevent the isolation of color charges by the creation of a light quark-antiquark pair from the invested

energy to form a color neutral  $B^+B^-$ -pair. The picture is also more complicated for the excited states as becomes apparent from the  $\Upsilon(4S)$ , whose mass lies above the  $B^+B^-$ -threshold.

Due to the large mass of the bottom quark,  $b\bar{b}$  pairs can only be produced in hard processes in the initial phase of the collision over timescales of the order  $\tau_{b\bar{b}} \sim 1/(2m_b)$ , where  $m_b$  is the mass of the bottom quark. This fact is utilized in the Color-Singlet Model, an early quarkonium production model, where the hard part of the production process is calculated in pQCD, while soft part is captured in a bottomium wave function. It is assumed that color and spin of the  $b\bar{b}$  pair do not change during the formation process so that bottomia can only be formed from  $b\bar{b}$  pairs that have been produced in a color-singlet state.<sup>2</sup> In the Color Evaporation Model, on the other hand, it is assumed that the  $b\bar{b}$  pair interacts softly with its environment during the formation process so its initial quantum numbers are not conserved and need not be related to their final values (for more information on quarkonium production see e.g. Lansberg, 2006, and references therein).

Bottomia acquire quite unusual properties as compared to light mesons or baryons due to the combination of the running coupling and the large quark masses involved.

First, the bottomium mass is mostly due to the rest-mass of its constituents whereas the mass of a light hadron results almost entirely from the binding energy. Second, the large masses result in small hadrons, i.e. the coupling strength is relatively weak inside bottomia. In this case the binding becomes similar to that of a Coulomb bound state, especially for the lowest lying bottomium states, so that potential models can be applied. Third, the relatively small coupling causes small relative velocities of the quarks in the bound state so that non-relativistic quantum mechanics is applicable.

While the binding of bottomia is still more complicated than the binding of QED bound states, their properties can be modeled theoretically much better and with much less effort than that of other QCD bounds state like baryons or light mesons. This holds especially well for bottomium states due to the much larger mass of the bottom quark. Jacobs et al. (1986), for example, have reproduced elementary properties of bottomia (and charmonia) quite well using a Schrödinger equation with the Cornell potential

$$V_{\text{Cornell}}(r) = \sigma r - \frac{\alpha_{\text{eff}}}{r}, \quad (1.4)$$

where  $\alpha_{\text{eff}}$  is an effective Coulomb-like coupling and the string tension  $\sigma$  represents the non-perturbative, phenomenological input.

---

<sup>2</sup>As we will see in chapter 2 the interaction potential of a color-octet pair is repulsive.

Matsui and Satz (1986) first proposed quarkonia as probes for the properties of the QGP. They considered static, non-relativistic charm-anticharm systems, governed by the Cornell potential (1.4). Asymptotic freedom suggests that  $\sigma$  is a decreasing function of temperature  $T$ , which vanishes in a deconfined medium where  $T > T_c$ . Hence Matsui and Satz argued that Debye screening of the color charge would change eq. (1.4) to a screened Coulomb potential,

$$V_{\text{Cornell}}(r) \xrightarrow{T > T_c} -\frac{\alpha_{\text{eff}}}{r} e^{-m_D(T)r}, \quad (1.5)$$

where  $m_D(T)$  is the Debye mass in the QGP. Such behavior is indeed backed up by LQCD results (Kaczmarek and Zantow, 2005). It follows from this argument that color screening forbids the existence of bound states above a certain melting temperature  $T_m$ . Not surprisingly it is found that the melting temperature decreases with increasing excitation of the state. Further  $T_m$  is higher for bottomia than for charmonia, with the  $\Upsilon(1S)$  being by far the most stable state.

Even though the picture is really not as simple as originally proposed by Matsui and Satz (1986), color screening remains an important effect for the suppression of quarkonia in the QGP, especially for the excited states.

### 1.3 Theoretical outline, experimental input

We outline the phenomenological model used to calculate the amount of  $\Upsilon$  suppression in LHC PbPb collisions. Subsequently we present recent CMS data that are used to test its accuracy.

The model is based on three successive steps:

1. Calculate the bottomium wave functions and decay widths from a non-relativistic, complex potential model that properly accounts for the temperature-dependent running of the coupling (chapter 3). This accounts for three processes contributing to  $\Upsilon$  suppression:
  - Color screening which prevents the formation of bottomia above the melting temperature  $T_m$
  - Collisional damping, represented by the imaginary part  $\text{Im} V$  of the complex potential
  - Gluodissociation, represented by the dipole interaction term in the pNRQCD action

2. Calculate the evolution of the QGP in the longitudinally and transversely expanding fireball, formed in relativistic heavy ion collisions, using perfect-fluid hydrodynamics (chapter 4). Interpolating the decay widths obtained in step one to the temperature values from the numerically calculated profiles yields the amount of suppression within the QGP.
3. Calculate the decay cascade within the bottomium family to find the fraction of dimuon decays,  $\Upsilon(nS) \rightarrow \mu^+\mu^-$ , that originate from surviving  $\Upsilon$  states to obtain the final suppression factors  $R_{AA}(\Upsilon(nS))$  (chapter 5).

The model separates the suppression process into two consecutive phases: within the fireball and after it has cooled. The above mentioned processes rapidly diminish the bottomium population within the QGP-lifetime of less than 10 fm/c (Aamodt et al., 2011). After the fireball has cooled the surviving bottomia fly through the detector, decaying according to their vacuum lifetimes that are of the order  $10^4$  fm/c (Beringer et al., 2012). The excited bottomium states, however, have been efficiently dissociated in the fireball so that missing feed-down to the ground state  $\Upsilon(1S)$  represents another, indirect source of suppression.

Suppression from cold-nuclear-matter (CNM) effects like the Cronin effect, nuclear absorption and (anti-) shadowing are currently not considered in this model.

Given that a lot of effort has been made up to this point, both theoretically and experimentally, to study charmonium suppression in heavy ion collisions, we should justify why only bottomia are treated in this model:

First, the theoretical treatment exploited in this work is suited for heavy quarks, whereas the charm is rather a medium-mass quark. Even for bottomia a lot of approximations are necessary and the models have to be pushed to their limits of validity when excited states are considered. This becomes very clear when the scale hierarchy of excited bottomium states in the QGP is considered (see appendix B).

Second, bottomia are more stable than charmonia. The mass gap to the open bottom/charm threshold, for example, is approximately 1100 MeV for  $\Upsilon(1S)$  and 640 MeV for  $J/\psi$ . More processes will therefore contribute significantly to charmonium suppression.

Third, the relatively large number of  $c\bar{c}$  pairs produced on average per PbPb collision at the LHC leads to a significant amount of regeneration by statistical hadronization (Braun-Munzinger et al., 1995; Braun-Munzinger and Stachel, 2010).

The following bottomium states are considered in this model:

$$\Upsilon(1S), \quad \chi_b(1P), \quad \Upsilon(2S), \quad \chi_b(2P), \quad \Upsilon(3S), \quad \chi_b(3P),$$

with masses given in tab. 1.1. The masses of the  $\chi_{bJ}(1P)$ - and  $\chi_{bJ}(2P)$ -states are averaged, weighted with their multiplicities  $2J + 1$  to yield

$$M(\chi_b(1P)) = 9899.87, \quad M(\chi_b(2P)) = 10260.24. \quad (1.6)$$

The experimental data to test the model is taken from the CMS experiment from the November 2011 PbPb-run at  $\sqrt{s_{NN}} = 2.76$  TeV, where the minimum bias suppression factors  $R_{AA}(\Upsilon(nS))$  have been measured (Chatrchyan et al., 2012),

$$\begin{aligned} R_{AA}(\Upsilon(1S)) &= 0.56 \pm 0.08 \text{ (stat)} \pm 0.07 \text{ (sys)}, \\ R_{AA}(\Upsilon(2S)) &= 0.12 \pm 0.04 \text{ (stat)} \pm 0.02 \text{ (sys)}, \\ R_{AA}(\Upsilon(3S)) &= 0.03 \pm 0.04 \text{ (stat)} \pm 0.01 \text{ (sys)}, \end{aligned} \quad (1.7)$$

and also the double ratios,

$$\begin{aligned} \frac{[\Upsilon(2S)/\Upsilon(1S)]_{\text{PbPb}}}{[\Upsilon(2S)/\Upsilon(1S)]_{pp}} &= 0.21 \pm 0.07 \text{ (stat)} \pm 0.02 \text{ (sys)}, \\ \frac{[\Upsilon(3S)/\Upsilon(1S)]_{\text{PbPb}}}{[\Upsilon(3S)/\Upsilon(1S)]_{pp}} &= 0.06 \pm 0.06 \text{ (stat)} \pm 0.06 \text{ (sys)}. \end{aligned} \quad (1.8)$$

The relative yields  $\Upsilon(nS)/\Upsilon(1S)$  in the dimuon decay channel in PbPb and  $pp$  collisions, both at the same energy, are given by

$$\begin{aligned} [\Upsilon(2S)/\Upsilon(1S)]_{pp} &= 0.56 \pm 0.13 \text{ (stat)} \pm 0.02 \text{ (sys)}, \\ [\Upsilon(2S)/\Upsilon(1S)]_{\text{PbPb}} &= 0.12 \pm 0.03 \text{ (stat)} \pm 0.02 \text{ (sys)}, \\ [\Upsilon(3S)/\Upsilon(1S)]_{pp} &= 0.41 \pm 0.11 \text{ (stat)} \pm 0.04 \text{ (sys)}, \\ [\Upsilon(3S)/\Upsilon(1S)]_{\text{PbPb}} &= 0.02 \pm 0.02 \text{ (stat)} \pm 0.02 \text{ (sys)}. \end{aligned} \quad (1.9)$$

CMS has also performed centrality dependent measurements of the two suppression factors  $R_{AA}(\Upsilon(1S))$  and  $R_{AA}(\Upsilon(2S))$  as well as the double ratio  $\frac{[\Upsilon(2S)/\Upsilon(1S)]_{\text{PbPb}}}{[\Upsilon(2S)/\Upsilon(1S)]_{pp}}$ , which are compared to the theoretical results in chapter 6.

# Chapter 2

## Theoretical foundations

In this chapter we introduce basic theoretical concepts to treat bottomia in a thermal environment. In section 2.1 we explain some basic QCD concepts and relations and introduce the QCD action. The effect of finite temperature is introduced in section 2.2. We integrate out the light quark degrees of freedom to obtain the action of a  $b\bar{b}$  system immersed in a thermal medium consisting of light quarks and gluons. In section 2.3 we sketch the derivation of the pNRQCD action for the  $b\bar{b}$  system, where the hard and soft gluon degrees of freedom have been integrated out. Finally, in section 2.4 we show how the high-temperature interaction potential of the  $b\bar{b}$  system can be derived in this formalism.

### 2.1 Quantum chromodynamics

Let  $S[\Psi, A]$  denote the QCD action, which is a functional of the quark fields, collectively denoted by  $\Psi$ , and the gluon field  $A$ . QCD is a gauge theory with the gauge group  $SU(N_c)$ , where  $N_c = 3$  is the number of colors.  $SU(N_c)$  is the non-abelian group formed by the set of complex  $N_c \times N_c$  matrices  $U$ , which are unitary and have unit determinant,

$$U^\dagger = U^{-1}, \quad \det U = 1, \quad (2.1)$$

together with matrix multiplication as group operation. As such its action  $S$  is invariant under the following local, simultaneous gauge transformation:

$$\begin{aligned} \Psi(x) &\rightarrow \Psi'(x) = U(x)\Psi(x), \\ \bar{\Psi}(x) &\rightarrow \bar{\Psi}'(x) = \bar{\Psi}(x)U^{-1}(x), \\ A(x) &\rightarrow A'(x) = \left( U(x)A(x) + \frac{1}{ig}dU(x) \right) U^{-1}(x), \end{aligned} \quad (2.2)$$

where  $U(x)$  is an arbitrary, spacetime dependent  $SU(N_c)$ -matrix,  $g$  the QCD coupling strength,  $d$  the exterior derivative and  $\bar{\Psi} = \Psi^\dagger \gamma^0$  is the Dirac conjugate of  $\Psi$  ( $\gamma^0$  is a Dirac matrix). The quark field  $\Psi$  is a Dirac spinor in spacetime and transforms as a vector in the fundamental representation of  $SU(N_c)$  in the  $N_c$ -dimensional color space. The gluon field  $A$  is a 1-form in spacetime and a matrix in color space, which transforms in the adjoint representation. Thus there are  $N_c^2 - 1 = 8$  different gluon fields,

$$A = A_\mu^a T_a dx^\mu, \quad (2.3)$$

where  $T_a$  are the traceless, hermitian generators of  $SU(N_c)$ . They satisfy the following commutation and anticommutation relations,

$$[T_a, T_b] = i f_{abc} T_c, \quad \{T_a, T_b\} = \frac{1}{N_c} \delta_{ab} + d_{abc} T_c, \quad (2.4)$$

where  $f_{abc}$  and  $d_{abc}$  are the completely antisymmetric and symmetric structure constants, respectively. In the adjoint representation we have  $(T_a^A)_{bc} = -i f_{abc}$ , whereas, in the fundamental representation of  $SU(3)$ , the generators are given in terms of the Gell-Mann matrices  $\lambda_a$  via  $T_a^F = \lambda_a/2$ .

In quantum electrodynamics (QED), the transformation ‘‘matrix’’  $U$  is simply a complex number and the structure constants of this abelian gauge-group vanish identically.

Two important identities, obeyed by the generators  $T^F$  in the fundamental representation, are given by

$$T_a^F T_a^F = \frac{N_c^2 - 1}{2N_c} \mathbb{1}_c, \quad \text{Tr } T_a^F T_b^F = \frac{1}{2} \delta_{ab}, \quad (2.5)$$

where  $\mathbb{1}_c$  is the unit matrix in color space.

The transformation law in eq. (2.2) reminds of the transformation law for a connection on a differentiable manifold and is dictated by the gauge invariance of the QCD action. It gives rise to the gauge-covariant derivative

$$D = d - igA^a T_a, \quad (2.6)$$

where the  $SU(3)$  generators  $T_a$  are given in the representation of the object on which  $D$  is acting. The covariant derivative behaves under gauge transformations according to

$$D \rightarrow D' = U D U^{-1}. \quad (2.7)$$

The QCD action may now be formulated completely analogous to the action of QED, which is most conveniently written in terms of the electromagnetic

field strength 2-form  $F = dA$ . Hence in QCD we may define a chromodynamic field strength 2-form for the gluon field,

$$F = \frac{1}{2} F_{\mu\nu}^a T_a dx^\mu \wedge dx^\nu, \quad (2.8)$$

which is defined as

$$F = \frac{i}{g} [D, D], \quad \text{or equivalently} \quad D^2 \omega = F \wedge \omega, \quad (2.9)$$

for an arbitrary differential form  $\omega$ , which transforms as a vector under gauge transformations.  $F$  is then given by

$$F = dA - igA \wedge A = \left( dA^a + \frac{g}{2} A^b \wedge A^c f_{abc} \right) T_a. \quad (2.10)$$

The quantity  $F_{\mu\nu}^a$  in eq. (2.8) is the non-abelian generalization of the electromagnetic field strength tensor  $F_{\mu\nu}$ . It represents the field strength of the 8 independent gluon fields. From  $F_{\mu\nu}^a$  we may define chromoelectric and -magnetic fields, respectively,

$$E_i = E_i^a T_a = \frac{i}{g} [D_i, D_0], \quad B^i = B^{ia} T_a = \frac{i}{2g} \varepsilon^{ijk} [D_j, D_k]. \quad (2.11)$$

From eq. (2.7) it follows that  $F$  transforms as a second rank tensor under gauge transformations,  $F \rightarrow U F U^{-1}$ . Hence we find that the three most simple, gauge invariant expressions read,

$$\begin{aligned} \bar{\Psi} \Psi &\rightarrow \bar{\Psi}' \Psi' = \bar{\Psi} \Psi, \\ \bar{\Psi} D \Psi &\rightarrow \bar{\Psi}' D' \Psi' = \bar{\Psi} D \Psi, \\ \text{Tr } F \wedge F &\rightarrow \text{Tr } F' \wedge F' = \text{Tr } F \wedge F, \\ \text{Tr } F \wedge *F &\rightarrow \text{Tr } F' \wedge *F' = \text{Tr } F \wedge *F, \end{aligned} \quad (2.12)$$

where  $*F$  means the Hodge dual of  $F$ . In the third and fourth lines we have used the cyclic property of the trace. The most simple, gauge-invariant expression of the QCD action is then given by

$$\begin{aligned} S &= S_A + S_\Psi, \\ S_A &= \text{Tr} \int F \wedge *F = -\frac{1}{4} \int d^4x F_{\mu\nu}^a F^{a\mu\nu}, \\ S_\Psi &= \sum_f \int d^4x \bar{\Psi}_f (i\not{D} - m_f) \Psi_f \end{aligned}$$

$$= \sum_f \int d^4x \bar{\Psi}_f (i\not{\partial} + g\not{A} - m_f) \Psi_f, \quad (2.13)$$

where  $f$  runs through the six quark flavors and we have used  $d\Psi = \partial\Psi$ . We have omitted  $F \wedge F$  in eqs. (2.13) since it can be rewritten as a total derivative and therefore adds only a constant to the action. More specifically, the gauge sector  $S_A$  of the QCD action is given by

$$\begin{aligned} S_A &= \frac{1}{2} \int dA^a \wedge *dA^a - \frac{g}{4} \int (dA^a \wedge *(A^b \wedge A^c) + A^a \wedge A^b \wedge *dA^c) f_{abc} \\ &\quad + \frac{g^2}{8} \int A^a \wedge A^b \wedge *(A^c \wedge A^d) f_{abc} f_{cde} \\ &= \int d^4x \left[ \frac{1}{2} A_\alpha^a (\eta^{\alpha\beta} \partial^2 - \partial^\alpha \partial^\beta) A_\beta^a \right. \\ &\quad \left. - g f_{abc} A^{\mu a} A^{\nu b} \partial_\mu A_\nu^c - \frac{g^2}{4} f_{abe} f_{cde} A_\mu^a A_\nu^b A^{\mu c} A^{\nu d} \right]. \end{aligned} \quad (2.14)$$

From this action we can perturbatively calculate the running of the coupling strength  $g$  with the four-momentum exchange  $q$  in the interaction process. Defining the strong coupling “constant”,

$$\alpha_s = \frac{g^2}{4\pi}, \quad (2.15)$$

we obtain to first order (see e.g. Srednicki, 2007; Peskin and Schroeder, 1995)

$$\alpha_s(Q) = \frac{\alpha(\mu)}{1 + \alpha(\mu) b_0 \ln \frac{Q}{\mu}}, \quad b_0 = \frac{11N_c - 2N_f}{6\pi}, \quad (2.16)$$

where  $Q = |q|$  and  $\mu$  is an arbitrary reference scale. The strong coupling  $\alpha_s$  manifestly decreases with increasing  $Q$ , giving rise to asymptotic freedom. The coupling diverges at a finite momentum scale  $\Lambda_{\text{QCD}}$ , the QCD scale,

$$\Lambda_{\text{QCD}} = \mu \exp \left[ -\frac{1}{b_0 \alpha_s(\mu)} \right], \quad (2.17)$$

which marks the brake down of perturbation theory in low-energy processes and the crossover into the non-perturbative regime of confinement.

A summary of results for higher orders in perturbation theory can be found in Bethke (2009). Using up-to-date experimental results for  $\alpha_s(M_Z)$ , the strong coupling evaluated at the mass of the  $Z$  boson,  $M_Z = 91.2$  GeV, (Beringer et al., 2012) as well as  $N_c = N_f = 3$ , we obtain for  $\Lambda_{\text{QCD}}$  (Bethke, 2013)

$$\Lambda_{\text{QCD}} = 276.3 \text{ MeV}, \quad \alpha_s(M_Z) = 0.1197, \quad (2.18)$$

where we have used the  $\alpha_s(M_Z)$ -value that result from matching to charm and bottom masses.

The full QCD action given in the first line of eqs. (2.13) represents our starting point for further development of the formalism. In the following sections we will specialize it to the case of non-relativistic  $b\bar{b}$  bound states immersed in a hot, thermal medium.

## 2.2 Thermal modifications

Let us now rewrite the QCD action (2.13) in a way that is more appropriate to treat heavy quarks moving in the thermal background medium. For this purpose we introduce finite temperature and integrate out the light fermion degrees of freedom so they appear in the resulting action as part of a thermal background medium.

The following steps in this section are explained only very briefly. More information on thermal field theory and the treatment of heavy quarks in a thermal medium can be found in Kapusta (1989); Le Bellac (2000); Beraudo et al. (2010) or in appendix A.

We want to separate the quark fields  $\Psi_f$  in eq. (2.13) into light quarks  $q_f = (u, d, s)$ , which are treated as massless, and one heavy quark species  $b$  (bottom) with a large mass  $m_b$ ,

$$S = S_A + \int d^4x \bar{b}(i\not{D} - m_b)b + \sum_f \int d^4x \bar{q}_f i\not{D}q_f. \quad (2.19)$$

As explained in sections 1.2 and 1.3, charm and top quarks are not considered in this thesis because the former is neither light nor heavy whereas the latter decays too fast to form bound states.

To investigate the properties of bottomium states in a thermal medium with temperature  $T$  we consider the partition function  $Z$  of the system,

$$Z = \int \mathcal{D}q \mathcal{D}b \mathcal{D}A e^{-S_E}, \quad (2.20)$$

where the path integral measure is normalized to the free field theory. The euclidean action  $S_E$  is obtained by performing a Wick rotation to the imaginary time  $\tau = it$  and considering fields periodic in  $\tau$  with period  $\beta = 1/T$ . The heavy quark field  $b$ , however, is not set to be periodic in  $\tau$ , since the heavy quarks might not be thermalized. The integration in position- and

momentum-space in the euclidean sector becomes

$$\int d^4x_E = \int_0^\beta d\tau \int d^3x, \quad \int \frac{d^4k_E}{(2\pi)^4} = \frac{1}{\beta} \sum_{n=-\infty}^{\infty} \int \frac{d^3k}{(2\pi)^3}. \quad (2.21)$$

Since this procedure breaks explicit Lorentz-invariance anyway, we find it convenient to make use of the Coulomb-gauge.

In the high-temperature regime the coupling strength  $g$  becomes small so we may treat the cubic and quartic terms in  $A$  in eqs. (2.19) as a perturbation and neglect them for the present case. The euclidean action then reads

$$S_E = S_{\bar{b}b} + \int d^4x_E \left[ \frac{1}{2} \left( A_0^a \Delta A_0^a + \vec{A}^a (-\partial^2) \vec{A}^a \right) + \sum_f \bar{q}_f (-i\not{D}) q_f \right],$$

$$S_{\bar{b}b} = \int d^4x_E \bar{b} (-i\not{D} + m_b) b. \quad (2.22)$$

Integrating out the light fermion degrees of freedom in the partition function (2.20) yields a functional determinant so that

$$S_E = S_{\bar{b}b} + \int d^4x_E \frac{1}{2} \left( A_0^a \Delta A_0^a + \vec{A}^a (-\partial^2) \vec{A}^a \right) - \sum_f \text{Tr} \ln \left( 1 - \frac{1}{-i\not{D}} g A^a T_a \right), \quad (2.23)$$

where we have used the fact that the path integral measure is normalized to the free field theory.

In the high temperature regime, with small  $g$ , we may approximate the logarithm to quadratic order. Since the order linear in  $A$  does not contribute we have

$$S_E = S_{\bar{b}b} + \int d^4x_E \frac{1}{2} \left( A_0^a \Delta A_0^a + \vec{A}^a (-\partial^2) \vec{A}^a \right) - \frac{1}{2} \int d^4x_E d^4y_E A_\mu^a(x) \Pi^{\mu\nu}(x, y) A_\nu^a(y), \quad (2.24)$$

where  $\Pi$  is the gluon polarization tensor,

$$\Pi^{\mu\nu}(x, y) = \int \frac{d^4k_E}{(2\pi)^4} e^{ik(x-y)} \Pi^{\mu\nu}(k),$$

$$\Pi^{\mu\nu}(k) = -\frac{g^2}{2} \int_m \frac{d^4p_E}{(2\pi)^4} \text{Tr} [S(i\omega_m, \vec{p}) \gamma^\mu S(i\omega_m - i\omega_n, \vec{p} - \vec{k}) \gamma^\nu]. \quad (2.25)$$

The momentum-space expression of the polarization tensor is calculated in appendix A.2. From the first line of eqs. (A.27) one can see that the contribution of  $\Pi^{i0}$  vanishes in Coulomb gauge so we may define the longitudinal and transverse gluon propagators, respectively, as

$$\begin{aligned}\Delta_{00}(x) &= - \int \frac{d^4 k_E}{(2\pi)^4} \frac{e^{ikx}}{\vec{k}^2 + \Pi^{00}(k)}, \\ \Delta_{\perp ij}(x) &= \delta_{ij} \int \frac{d^4 k_E}{(2\pi)^4} \frac{e^{ikx}}{k^2 - \Pi_{\perp}(k)}.\end{aligned}\quad (2.26)$$

In terms of these propagators we may rewrite the action (2.24) as

$$\begin{aligned}S_E = S_{b\bar{b}} + \frac{1}{2} \int d^4 x_E d^4 y_E \left[ A_0^a(x) (\Delta^{-1})^{00}(x-y) A_0^a(y) \right. \\ \left. + A_i^a(x) (\Delta_{\perp}^{-1})^{ij}(x-y) A_j^a(y) \right].\end{aligned}\quad (2.27)$$

We have now arrived at a euclidean action for a  $b\bar{b}$  system immersed in a thermal background medium of light quarks and gluons.

## 2.3 NRQCD and pNRQCD

In this section we concentrate on the heavy quark section of the QCD action and employ the EFT formalism (Caswell and Lepage, 1986) to make use of the non-relativistic nature of bottomium.

The  $b\bar{b}$  part,  $S_{b\bar{b}}$ , of the full QCD action (2.19) reads

$$S_{b\bar{b}} = \int d^4 x_E b^\dagger \mathcal{H} b, \quad \mathcal{H} = \gamma^0 (-i \not{D} + m_b). \quad (2.28)$$

This expression contains contributions from all momentum scales. The intermixture of different scales is very inconvenient for the treatment of bound states since the binding of a  $b\bar{b}$  pair is an effect of soft-gluon exchange. Soft gluons have a momentum of the order of the inverse radius  $\langle 1/r \rangle$  of the bound state, as measured in the CM system. Hard or ultra soft gluons with momenta of the order of the bottom mass  $m_b$  or the binding energy  $E$  do not contribute to the binding.

In an ideal case the hard, soft and ultra soft scales are well separated,

$$m_b \gg \langle 1/r \rangle \gg E, \quad (2.29)$$

which is encountered e.g. in QED bound states with their small coupling  $\alpha \approx 1/137$ . It is this scale hierarchy which is utilized in the EFT approach.

For the strong coupling, however, a large separation is rather optimistic. Fortunately, the large bottom mass  $m_b$  ensures that the scales at least satisfy

$$m_b > \langle 1/r \rangle > E \quad (2.30)$$

as long as the state under consideration is not too highly excited. In the following we will, however, assume that the relations (2.29) indeed hold.

We would like to reduce eq. (2.28) into a form that exploits this separation of scales in order to simplify the treatment of bottomia. The following scales are important for a  $b\bar{b}$  bound state in a thermal medium:

hard scale	$m_b$
soft scale	$\langle 1/r \rangle \sim m_b v$
ultra soft scale	$E \sim m_b v^2$
QCD scale	$\Lambda_{\text{QCD}}$
temperature	$2\pi T$
Debye mass	$m_D \sim T\sqrt{\alpha_s}$ ,

where  $v$  is the relative velocity in the bound state. Evidently the last two scales are not present in the absence of a thermal medium. When a hot background medium is introduced, however, thermal effects will lower the soft and ultra soft scales, bringing them closer to  $\Lambda_{\text{QCD}}$ .

We will see in the following chapters that  $m_b \gg \langle 1/r \rangle$  and  $m_b \gg 2\pi T$  always holds for the QGP created in heavy ion collisions.<sup>1</sup> The first relation justifies the non-relativistic treatment whereas the second implies that interactions with light medium particles do not change the bottomium trajectories significantly.

While Caswell and Lepage (1986) derived the NRQCD formalism from arguments based on the renormalization group, we prefer the less rigorous but more vivid method using the Foldy-Wouthuysen transformation. From NRQCD we then proceed to pNRQCD (Pineda and Soto, 1998) to obtain a formalism for the interaction of a heavy  $b\bar{b}$  pair. More information on the derivation of NRQCD and pNRQCD can be found in Braaten (1997); Ghiglieri (2012).

In a first step we want to separate the quark and antiquark Weyl spinors  $\psi$  and  $\chi$  which constitute the Dirac spinor  $b = (\psi, \chi)^T$ . Working in the Dirac-representation, where  $\gamma^0$  is diagonal, we diagonalize the Hamiltonian by a unitary transformation (Foldy and Wouthuysen, 1950),

$$U = \exp \left[ -\frac{i\vec{D}}{2m_b} \right], \quad b' = Ub, \quad (2.31)$$

---

<sup>1</sup>Or rather  $m_b > \langle 1/r \rangle$  and  $m_b > 2\pi T$ , depending on the optimism of the reader.

where slashed three-vectors  $\vec{a}$  are defined as  $\not{a} = \vec{\gamma} \vec{a}$ . In the following we only need to keep terms of order  $1/m_b$ ,

$$\begin{aligned} S_{b\bar{b}} &= \int d^4x_E b'^{\dagger} U \mathcal{H} U^{\dagger} b' \\ &= \int d^4x_E b'^{\dagger} \left( \mathcal{H} - \frac{[i\vec{D}, \mathcal{H}]}{2m_b} - \frac{[\vec{D}, [\vec{D}, \mathcal{H}]]}{8m_b^2} \right) b' + O\left(\frac{1}{m_b^2}\right). \end{aligned} \quad (2.32)$$

From the properties of the  $\gamma$ -matrices we have

$$\gamma^i \gamma^j = -\delta^{ij} - i\varepsilon^{ijk} \gamma_5 \gamma^0 \gamma_k. \quad (2.33)$$

Inserting this into eq. (2.32) yields

$$S_{b\bar{b}} = \int d^4x_E b'^{\dagger} \left( D_{\tau} + \gamma^0 \left( m_b - \frac{\vec{D}^2 + g\vec{\sigma}\vec{B}}{2m_b} \right) + \frac{ig\vec{E}}{2m_b} \right) b', \quad (2.34)$$

where  $D_{\tau} = -iD_0 = \partial_{\tau} - gA_0$ . The chromoelectric field term relates quark to antiquark Weyl spinors and hence has to be removed by another Foldy-Wouthuysen transformation,

$$U' = \exp \left[ \frac{ig\gamma^0 \vec{E}}{4m_b^2} \right], \quad b'' = U' b'. \quad (2.35)$$

Including yet another field redefinition  $b''' = \exp[-\gamma^0 m\tau] b''$  to remove the rest-mass term and renaming  $b''' \rightarrow b$  yields

$$S_{b\bar{b}} = \int d^4x_E b^{\dagger} \left( D_{\tau} - \gamma^0 \frac{\vec{D}^2 + g\vec{\sigma}\vec{B}}{2m_b} \right) b. \quad (2.36)$$

We will further drop the chromomagnetic field term since it belongs to a higher order in the quark velocity (Bodwin et al., 1995). The resulting action, written in terms of the Weyl spinors, then reads

$$S_{b\bar{b}} = \int d^4x_E \left[ \psi^{\dagger} \left( D_{\tau} - \frac{\vec{D}^2}{2m} \right) \psi + \chi^{\dagger} \left( D_{\tau} + \frac{\vec{D}^2}{2m} \right) \chi \right]. \quad (2.37)$$

The correct matching with the full, relativistic theory would require including matching coefficients which are of the order  $1 + O(\alpha)$ . This is, however, not necessary for the order of accuracy required in the following chapters.

It is appropriate to switch to the operator formalism now, where the non-relativistic Hamiltonian of the system reads

$$H_{b\bar{b}} = \int d^3x \left[ \psi^\dagger \left( -gA_0 - \frac{\vec{D}^2}{2m} \right) \psi + \chi^\dagger \left( -gA_0 + \frac{\vec{D}^2}{2m} \right) \chi \right]. \quad (2.38)$$

The non-relativistic action (2.37) or the Hamiltonian (2.38) represent the starting point for NRQCD calculations. In order to obtain an appropriate formalism for heavy quark bound states, however, we have to proceed to pNRQCD. For this purpose we project the Hamiltonian (2.38) onto a  $b\bar{b}$ -bound state and perform path-ordering (Pineda and Soto, 1998),

$$\begin{aligned} H_{b\bar{b}} &\rightarrow \text{P} \langle b\bar{b} | H_{b\bar{b}} | b\bar{b} \rangle, \\ |b\bar{b}\rangle &= \int d^3x_1 d^3x_2 \Psi(\tau, \vec{x}_1, \vec{x}_2) \psi^\dagger(\tau, \vec{x}_1) \chi(\tau, \vec{x}_2) |0\rangle, \end{aligned} \quad (2.39)$$

where P arranges operator-ordering from  $\vec{x}_1$  (left) to  $\vec{x}_2$  (right). We have chosen equal imaginary times  $\tau$  since a universal choice of time can be made in this non-relativistic context. The wave function  $\Psi$  of the  $b\bar{b}$  system is a  $2 \times 2$  matrix in spin space and a  $3 \times 3$  matrix in color space. Dropping a constant contribution, the projected Hamiltonian reads

$$\begin{aligned} H_{b\bar{b}} &= \text{P} \int d^3x_1 d^3x_2 \Psi^\dagger(\tau, \vec{x}_1, \vec{x}_2) \\ &\cdot \left[ -g(A_0(\tau, \vec{x}_1) - A_0(\tau, \vec{x}_2)) - \frac{\vec{D}_1^2 + \vec{D}_2^2}{2m} \right] \Psi(\tau, \vec{x}_1, \vec{x}_2), \end{aligned} \quad (2.40)$$

while the corresponding action reads

$$S_{b\bar{b}} = \text{P} \int d\tau d^3x_1 d^3x_2 \Psi^\dagger(\tau, \vec{x}_1, \vec{x}_2) \left[ D_\tau - \frac{\vec{D}_1^2 + \vec{D}_2^2}{2m} \right] \Psi(\tau, \vec{x}_1, \vec{x}_2). \quad (2.41)$$

In the following the gauge field  $A$  is meant to contain only contributions of ultra soft gluons. This can be accomplished by separating the original gluon field into soft and ultra soft parts,  $A = A^S + A^{US}$ , and treating  $A^S$  and  $A^{US} \rightarrow A$  as independent fields. The soft contributions may then be integrated out by completing the square for  $A^S$  under the path integral. The soft part of the gluon spectrum is then included only indirectly through an additional, non-local, potential term in the action,

$$S = S_A + S_{b\bar{b}} + (g^S)^2 \text{P Tr} \int d^4x_{E1} d^4x_{E2} \Psi^\dagger(\tau_1, \vec{x}_1, \vec{x}_2)$$

$$\cdot T_a[\Delta_{00}(\tau_1 - \tau_2, \vec{x}_1 - \vec{x}_2) - \Delta_{00}(\tau_1 - \tau_2, 0)]T_a\Psi(\tau_2, \vec{x}_1, \vec{x}_2). \quad (2.42)$$

In the lowest order, the potential term simply reads

$$\alpha_s^S \text{P Tr} \int d\tau d^3x_1 d^3x_2 \frac{\Psi^\dagger(\tau, \vec{x}_1, \vec{x}_2) T_a T_a \Psi(\tau, \vec{x}_1, \vec{x}_2)}{|\vec{x}_1 - \vec{x}_2|}, \quad (2.43)$$

with the strong coupling evaluated at the soft scale,  $\alpha_s^S = (g^S)^2/(4\pi) = \alpha_s(\langle 1/r \rangle)$ . Thermal contributions and higher order corrections to the potential may be included by inserting eq. (2.26) for the propagators.

In order to arrive at pNRQCD, however, we further have to perform a multipole expansion of the ultra soft gluon field. Defining the relative-motion (RM) and CM coordinates,

$$\vec{r} = \vec{x}_1 - \vec{x}_2, \quad \vec{R} = \frac{\vec{x}_1 + \vec{x}_2}{2}, \quad (2.44)$$

respectively, we may define the singlet and octet fields  $S$  and  $O = O^a T_a$  via

$$\begin{aligned} \Psi(\tau, \vec{r}, \vec{R}) &= \text{P exp} \left[ ig \int_{\vec{x}_2}^{\vec{x}_1} d\vec{x} \vec{A} \right] \frac{\mathbb{1}_c}{\sqrt{N_c}} S(\tau, \vec{r}, \vec{R}) \\ &\quad + \text{P exp} \left[ ig \int_{\vec{R}}^{\vec{x}_1} d\vec{x} \vec{A} \right] \sqrt{2} O(\tau, \vec{r}, \vec{R}) \text{P exp} \left[ ig \int_{\vec{x}_2}^{\vec{R}} d\vec{x} \vec{A} \right] \\ &\approx e^{ig\vec{r}\vec{A}(\tau, \vec{R})} \frac{\mathbb{1}_c}{\sqrt{N_c}} S(\tau, \vec{r}, \vec{R}) + e^{ig\vec{r}\vec{A}(\tau, \vec{R})/2} \sqrt{2} O(\tau, \vec{r}, \vec{R}) e^{ig\vec{r}\vec{A}(\tau, \vec{R})/2}, \end{aligned} \quad (2.45)$$

where  $g$  is evaluated at the ultra soft scale and the factors  $\mathbb{1}_c/\sqrt{N_c}$  and  $\sqrt{2}$  normalize the traces over color indices to one. In this prescription, the singlet and octet fields transform under gauge transformations according to

$$\begin{aligned} S(\tau, \vec{r}, \vec{R}) &\rightarrow S(\tau, \vec{r}, \vec{R}), \\ O(\tau, \vec{r}, \vec{R}) &\rightarrow g(\tau, \vec{R}) O(\tau, \vec{r}, \vec{R}) g^{-1}(\tau, \vec{R}). \end{aligned} \quad (2.46)$$

Further, the multipole expanded covariant derivatives in eq. (2.41) read

$$\begin{aligned} D_\tau \Psi &= \partial_\tau \Psi - g A_0(\tau, \vec{x}_1) \Psi + g \Psi A_0(\tau, \vec{x}_2) \\ &= \partial_\tau \Psi - g [A_0(\tau, \vec{R}), \Psi] - \frac{g\vec{r}}{2} \{ \vec{\nabla} A_0(t, \vec{R}), \Psi \}, \end{aligned}$$

$$\vec{D}_{1/2}\Psi = \left(\frac{1}{2}\vec{\nabla}_R \pm \vec{\nabla}_r\right)\Psi - ig\left(1 \pm \frac{\vec{r}}{2}\vec{\nabla}_R\right)\vec{A}(t, \vec{R})\Psi. \quad (2.47)$$

Inserting this into eq. (2.42) yields

$$\begin{aligned} S &= S_A + \int d\tau d^3R d^3r \left[ S^\dagger (\partial_\tau + H_1) S + O^{a\dagger} (D_\tau + H_8) O^a \right. \\ &\quad \left. + g\sqrt{\frac{2}{N_c}} \vec{r} \text{Tr} \left( S^\dagger \vec{E} O + \vec{E} O^\dagger S \right) + g\vec{r} \text{Tr} \left( O^\dagger \vec{E} O + O^\dagger O \vec{E} \right) \right] \\ &= S_A + \int d\tau d^3r d^3R \left[ S^\dagger (\partial_\tau + H_1) S + O^{a\dagger} (D_\tau + H_8) O^a \right. \\ &\quad \left. + \frac{g}{\sqrt{2N_c}} \vec{r} \vec{E}^a (S^\dagger O^a + O^{a\dagger} S) + \frac{g}{2} \vec{r} \vec{E}^a O^{b\dagger} O^c d^{abc} \right], \end{aligned} \quad (2.48)$$

where we have defined the singlet- and octet Hamiltonians  $H_1$  and  $H_8$ , respectively. In absence of a thermal background medium and using the lowest order expression (2.43) we have,

$$\begin{aligned} H_1 &= -\frac{\Delta_R}{4m} - \frac{\Delta_r}{m} + V_1(r), & V_1(r) &= -\frac{C_F \alpha_s^S}{r}, \\ H_8 &= -\frac{\Delta_R}{4m} - \frac{\Delta_r}{m} + V_8(r), & V_8(r) &= \frac{\alpha_s^S}{2N_c r}, \end{aligned} \quad (2.49)$$

where we have used relations (2.5) and written  $C_F = (N_c^2 - 1)/(2N_c)$ . Note the chromoelectric dipole interaction terms in the pNRQCD action (2.48). The first term describes a singlet-octet transition of the  $b\bar{b}$  pair by the emission or absorption of an ultra soft gluon. This transition, in combination with the repulsive octet potential, results in gluodissociation of the bound color-singlet state.

Now we have nearly arrived at the envisaged point. With eq. (2.48) we have obtained the right starting point to treat a non-relativistic  $b\bar{b}$  bound state. In the next section we only have to include the effect of the thermal background medium on the interaction potential.

## 2.4 The long-time interaction potential

In order to account for the influence of the QGP on bottomium states, we have to include the contribution of the gluon polarization tensor to the heavy quark interaction potential, given in eqs. (2.42).

Therefore we calculate the longitudinal gluon propagator to first order,

$$\Delta_{00}(\tau, \vec{x}) = \int \frac{d^4q}{(2\pi)^4} e^{-q^0\tau + i\vec{q}\vec{x}} \rho(q^0, \vec{q}) (\Theta(\tau) + N(q^0)), \quad (2.50)$$

where we have defined the spectral density  $\rho$  as

$$\int_{-\infty}^{\infty} \frac{dz}{2\pi} \frac{\rho(z, \vec{q})}{z - q^0} = \frac{-1}{\vec{q}^2 + \Pi^{00}(q^0, \vec{q})}, \quad (2.51)$$

or equivalently, replacing  $q^0 \rightarrow q^0 + i0^+$  in eq. (2.51),

$$\rho(q^0, \vec{q}) = \frac{2 \operatorname{Im} \Pi^{00}(q^0, \vec{q})}{(\vec{q}^2 + \operatorname{Re} \Pi^{00}(q^0, \vec{q}))^2 + (\operatorname{Im} \Pi^{00}(q^0, \vec{q}))^2}. \quad (2.52)$$

The component  $\Pi^{00}$  of the polarization tensor and the corresponding Debye mass  $m_D$  are given in eqs. (A.26) and (A.25), respectively, to first order in the hard thermal loop (HTL) approximation. Its imaginary part,  $\operatorname{Im} \Pi^{00}$ , is only non-vanishing for  $|q^0| < |\vec{q}|$ , which yields the spectral function

$$\rho(q^0, \vec{q}) = \frac{\pi m_D^2 q^0}{|\vec{q}|} \frac{\Theta(|\vec{q}| - |q^0|)}{\left(\vec{q}^2 + m_D^2 \left(1 - \frac{q^0}{2|\vec{q}|} \ln \frac{|\vec{q}| + q^0}{|\vec{q}| - q^0}\right)\right)^2 + \left(\frac{\pi m_D^2 q^0}{2|\vec{q}|}\right)^2}. \quad (2.53)$$

Since the potential is formed by soft gluons with energies of the order  $\langle 1/r \rangle$ , much larger than the bottomium binding energy  $E$ , the  $b\bar{b}$  field  $\Psi$  in eq. (2.42) varies much slower in time than the propagator  $\Delta_{00}$ . Hence we may approximate

$$\begin{aligned} & \text{P Tr} \int_0^\tau d\tau_1 d\tau_2 \int d^3r d^3R \Psi^\dagger(\tau_1, \vec{r}, \vec{R}) \\ & \quad \cdot T_a [\Delta_{00}(\tau_1 - \tau_2, \vec{r}) - \Delta_{00}(\tau_1 - \tau_2, 0)] T_a \Psi(\tau_2, \vec{r}, \vec{R}) \\ & \approx \text{P Tr} \int d^3r d^3R \frac{1}{\tau} \int_0^\tau d\tau' \left( \Psi^\dagger(\tau', \vec{r}, \vec{R}) T_a T_a \Psi(\tau', \vec{r}, \vec{R}) \right) \\ & \quad \cdot \int_0^\tau d\tau_1 d\tau_2 [\Delta_{00}(\tau_1 - \tau_2, \vec{r}) - \Delta_{00}(\tau_1 - \tau_2, 0)], \end{aligned} \quad (2.54)$$

i.e. we replace the heavy quark-field by its mean value over the imaginary time  $\tau$ . We do not integrate to  $\tau = \beta$  like for the periodic fields  $q_f$  and  $A$ , since the bottomium system is not equilibrated with its thermal environment and hence  $\Psi$  is not periodic in the imaginary time.

We perform the temporal double integral of the propagator, taking the  $\tau$ -dependence from eq. (2.50),

$$\int_0^\tau d\tau_1 d\tau_2 e^{-q^0(\tau_1 - \tau_2)} (\Theta(\tau_1 - \tau_2) + N(q^0))$$

$$= \frac{\tau}{q^0} - \frac{1 - e^{-q^0\tau} + (2 - e^{q^0\tau} - e^{-q^0\tau})N(q^0)}{q^{0^2}}. \quad (2.55)$$

We are interested in the potential governing the behavior at large times,  $t \rightarrow \infty$ , corresponding to  $\tau \rightarrow i\infty$ , where the exponential may be written as

$$\lim_{\tau \rightarrow i\infty} e^{q^0\tau} = 1 + i\pi\delta(q^0)(q^0 + q^{0^2}\tau). \quad (2.56)$$

The double integral over the propagator then yields

$$\begin{aligned} & \frac{1}{\tau} \int_0^\tau d\tau_1 d\tau_2 \Delta(\tau_1 - \tau_2, \vec{r}) \\ &= \int \frac{d^3q}{(2\pi)^3} e^{i\vec{q}\vec{r}} \left( \int \frac{dq^0}{2\pi} \frac{\rho(q^0, \vec{q})}{q^0} + \left( \frac{i}{\beta} - \frac{i}{2\tau} \right) \lim_{q^0 \rightarrow 0} \frac{\rho(q^0, \vec{q})}{q^0} \right) \\ &= \int \frac{d^3q}{(2\pi)^3} e^{i\vec{q}\vec{r}} \left( \frac{-1}{\vec{q}^2 + m_D^2} + \frac{i\pi m_D^2}{\beta |\vec{q}| (\vec{q}^2 + m_D^2)^2} \right). \end{aligned} \quad (2.57)$$

In going from the first to the second line we have neglected  $1/\tau$  as compared to  $1/\beta$  and used

$$\begin{aligned} \int \frac{dq^0}{2\pi} \frac{\rho(q^0, \vec{q})}{q^0} &= \frac{-1}{\vec{q}^2 + \Pi(0, \vec{q})} = \frac{-1}{\vec{q}^2 + m_D^2}, \\ \lim_{q^0 \rightarrow 0} \frac{\rho(q^0, \vec{q})}{q^0} &= \frac{\pi m_D^2}{|\vec{q}| (\vec{q}^2 + m_D^2)^2}, \end{aligned} \quad (2.58)$$

according to eqs. (2.51) and (2.53). Correspondingly, we obtain for the expression (2.54)

$$\begin{aligned} \text{P Tr} \int d^3r d^3R \int_0^\tau d\tau' \left( \Psi^\dagger(\tau', \vec{r}, \vec{R}) T_a T_a \Psi(\tau', \vec{r}, \vec{R}) \right) \\ \cdot \left( -\frac{m_D r + e^{-m_D r}}{4\pi r} - \frac{i\phi(m_D r)}{4\pi\beta} \right), \end{aligned} \quad (2.59)$$

where we have defined

$$\phi(x) = \int_0^\infty \frac{dz 2z}{(1+z^2)^2} \left( 1 - \frac{\sin xz}{xz} \right). \quad (2.60)$$

The function  $\phi$  takes values in the half-open interval  $[0, 1[$ . Further it obeys the differential equation

$$\left( \partial_x^2 - 1 - \frac{2}{x^2} \right) \phi(x) = -1, \quad (2.61)$$

which has the following solution:

$$\phi(x) = 1 + \text{Chi}(x) \left( \frac{\sinh x}{x} - \cosh x \right) + \text{Shi}(x) \left( \sinh x - \frac{\cosh x}{x} \right), \quad (2.62)$$

where Shi and Chi are the hyperbolic sine and cosine integrals, respectively. For large values of  $x$  a power series representation in even powers of  $1/x$  is also useful,

$$\phi(x) = \sum_{i=0}^{\infty} \frac{a_i}{x^{2i}}, \quad a_0 = 1, \quad a_{i+1} = 2((2i+1)i-1)a_i. \quad (2.63)$$

Note that this is a non-convergent, i.e. asymptotic, series since all  $a_i$  except  $a_0$  are negative and grow faster than  $1/x^{2i}$ .

The the singlet- and octet-potentials of section 2.3 are now changed to the same expressions as found earlier by Laine et al. (2007); Beraudo et al. (2008); Brambilla et al. (2008),

$$\begin{aligned} V_1(r) &= -C_F \alpha_s^S \left( m_D + \frac{e^{-m_D r}}{r} + iT\phi(m_D r) \right) + O((\alpha_s^S)^2), \\ V_8(r) &= \frac{\alpha_s^S}{2N_c} \left( m_D + \frac{e^{-m_D r}}{r} + iT\phi(m_D r) \right) + O((\alpha_s^S)^2). \end{aligned} \quad (2.64)$$

Thus we have obtained a formalism which describes a heavy, non-relativistic  $b\bar{b}$  pair immersed in a thermal medium. This represents a good background to build a model for the suppression of bottomia in the QGP created in heavy ion collisions.

It should be noted that, strictly speaking, the results of this section are valid for  $2\pi T \gg \langle 1/r \rangle$  only, which turns out to be satisfied most of the time as we will see in chapter 3. For the  $\Upsilon(1S)$  however, this relation does not hold once  $T$  drops below  $\sim 230$  MeV. In this case a different potential has to be used (Brambilla et al., 2008).



# Chapter 3

## Dissociation of bottomium in a thermal medium

In this chapter we consider the dissociation of bottomium states in a thermal medium. Section 3.1 investigates the bound state solutions and corresponding decay widths in a non-relativistic, complex potential model. The potentials used are derived from pNRQCD as introduced in chapter 2 but augmented by some phenomenological input to improve the approach in the non-perturbative regime. Section 3.2 is concerned with the process of gluodissociation, that results from the transition of a bound color-singlet state to an unbound color-octet state by emission or absorption of an ultra soft gluon. A comparison with the results of Peskin (1979); Bhanot and Peskin (1979) is also made.

### 3.1 Bound state bottomium wave functions

In this section we calculate the in-medium color-singlet wave functions from a potential approach in line with the formalism developed in chapter 2. The bound state wave function  $\psi_{nlm}$  is characterized by the well known principal, angular and magnetic quantum numbers  $n$ ,  $l$  and  $m$ , respectively, while the corresponding bottomium state is given in the notation  $(n - l, l)$ . The  $\Upsilon(nS)$  and  $\chi_b(nP)$  wave functions obey the temperature-dependent, stationary Schrödinger equation

$$\left(2m_b - \frac{\Delta}{m_b} + V_{nl}(r, T) - M_{nl}(T) + \frac{i\Gamma_{nl}(T)}{2}\right) \psi_{nlm}(\vec{x}, T) = 0, \quad (3.1)$$

where  $\Gamma_{nl}$  means the decay width,  $m_b$  the bottom mass,  $M_{nl}$  the temperature-dependent mass of the bound state and  $V_{nl}$  is a complex interaction potential.

While it is tempting to simply use the singlet potential from eqs. (2.64) we would like to modify  $V_{nl}$  such that it reduces to the Cornell potential in the limit of zero temperature,

$$\lim_{T \rightarrow 0} V_{nl}(r, T) = V_{\text{Cornell}}(r) = -\frac{\alpha_{\text{eff}}}{r} + \sigma r. \quad (3.2)$$

The Cornell potential, with its effective Coulomb- plus linear string term, has proven appropriate to treat also higher excited quarkonia at zero temperature (see e.g. Jacobs et al., 1986). Hence a combination of the potentials (2.64) and (3.2) seems appropriate. Instead of a simple, linear term, we therefore include a temperature-dependent string part which is parameterized as in Karsch et al. (1988). The full singlet potential then reads

$$\begin{aligned} V_{nl}(r, T) &= \frac{\sigma}{m_D(T)} \left( 1 - e^{-m_D(T)r} \right) \\ &\quad - C_F \alpha_{nl}(T) \left( m_D(T) + \frac{e^{-m_D(T)r}}{r} + iT\phi(m_D(T)r) \right), \\ m_D(T) &= T \sqrt{4\pi\alpha_T \frac{2N_c + N_f}{6}}, \end{aligned} \quad (3.3)$$

where the string tension equals  $\sigma = 0.192 \text{ GeV}^2$ , the function  $\phi$  is given in eq. (2.60) and the Debye mass  $m_D$ , calculated perturbatively in the HTL approximation (see appendix A), contains the number of colors and flavors, respectively, as degrees of freedom, where  $N_c = N_f = 3$ . The variables  $\alpha_T$  and  $\alpha_{nl}$  denote the strong coupling constant  $\alpha_s$  evaluated at the thermal scale  $2\pi T$  and the soft scale  $S_{nl}(T) = \langle 1/r \rangle_{nl}(T)$  of the bottomium state  $(n-l, l)$ , respectively,

$$\alpha_T = \alpha_s(2\pi T), \quad \alpha_{nl}(T) = \alpha_s(S_{nl}(T)). \quad (3.4)$$

In this thesis we use the first order expression for the strong coupling  $\alpha_s(Q)$  as given in eq. (2.16) with the QCD scale  $\Lambda_{\text{QCD}}$  for  $N_c = N_f = 3$  as given in eq. (2.18).

Obviously the potential  $V_{nl}$  reduces to eq. (3.2), in the limit  $T \rightarrow 0$ , with  $\alpha_{\text{eff}} = C_F \alpha_{nl}(0)$ . Eq. (3.3), however, includes the effects of the thermal background medium on the  $b\bar{b}$ -bindings which we arbitrarily denote by the two different terms “color screening” and “collisional damping”.

The term “color screening” is due to the analogy with the classical phenomenon of Debye screening in an electromagnetic plasma. It refers to the exponential damping in the real part of  $V_{nl}$ , which introduces a color screening length  $r_D$ , equal to the inverse of the Debye mass  $r_D = m_D^{-1}$ . As a consequence the constituents of the QGP restrict the range of the color-singlet

potential to a length of the order  $r_D$ . The color screening length decreases with increasing temperature, thus lifting all energy levels up towards the continuum. Correspondingly, for every bottomium state there exists some critical melting temperature  $T_m$  above which no bound state solutions to eq. (3.1) exist.

“Collisional damping”, named after the classical phenomenon of Landau damping, refers to the imaginary part of the potential  $V_{nl}$ . It describes the break up of the  $b\bar{b}$ -binding due to collisions with medium particles and hence introduces a decay width  $\Gamma_{nl}$  into the Schrödinger equation (3.1),

$$\begin{aligned}\Gamma_{nl}(T) &= \langle nlm | 2 \operatorname{Im} V(T) | nlm \rangle \\ &= \int d^3x |\psi_{nlm}(\vec{x})|^2 2 \operatorname{Im} V_{nl}(r, T).\end{aligned}\quad (3.5)$$

Quite frankly, the processes of color screening and collisional damping both describe soft interactions of the medium with the  $b\bar{b}$  pair and their exchange-gluons. The divide into two separate phenomena is due to historical reasons since the imaginary part of the potential arises only in quantum theory whereas Debye screening is also present in a classical plasma.

Let us now make the common separation Ansatz for central potentials,

$$\psi_{nlm}(r, \theta, \varphi, T) = \frac{g_{nl}(r, T)}{r} Y_{lm}(\theta, \varphi), \quad (3.6)$$

with the spherical harmonics  $Y_{lm}$ , and define energy levels  $E_{nl}$  such that

$$E_{nl}(T) = \begin{cases} M_{nl}(T) - 2m_b + \lim_{r \rightarrow \infty} V_{nl}(r, T), & T > 0, \\ M_{nl}(0) - 2m_b, & T = 0. \end{cases} \quad (3.7)$$

Further we define the effective potential  $V_{\text{eff},nl}$  which vanishes at infinity only for finite temperature,

$$\begin{aligned}V_{\text{eff},nl}(r, T > 0) &= \frac{l(l+1)}{m_b r^2} + V_{nl}(r, T) - \lim_{r \rightarrow \infty} V_{nl}(r, T) \\ &= \frac{l(l+1)}{m_b r^2} - \left( \frac{\sigma}{m_D(T)} + \frac{C_F \alpha_{nl}(T)}{r} \right) e^{-m_D(T)r} \\ &\quad - i C_F \alpha_{nl}(T) T \phi(m_D(T)r), \\ V_{\text{eff},nl}(r, T = 0) &= \frac{l(l+1)}{m_b r^2} + \lim_{T \rightarrow 0} V_{nl}(r, T) \\ &= \frac{l(l+1)}{m_b r^2} - \frac{C_F \alpha_{nl}(0)}{r} + \sigma r.\end{aligned}\quad (3.8)$$

The effective potential  $V_{\text{eff},nl}$  is depicted in fig. 3.1 for the 1S and 1P states for different temperatures. The counter intuitive behavior of the real part at zero temperature is due to the discontinuous transition for  $T \rightarrow 0$ .

Thus we obtain the temperature-dependent, radial Schrödinger equation,

$$\partial_r^2 g_{nl}(r, T) = m_b \left( V_{\text{eff},nl}(r, T) - E_{nl}(T) + \frac{i\Gamma_{nl}(T)}{2} \right) g_{nl}(r, T). \quad (3.9)$$

Eq. (3.9) is solved numerically for the different bottomium states and different temperatures using the modified midpoint method for second-order conservative equations (see Press et al., 2002, p. 928).

Since the coupling constant  $\alpha_{nl}(T)$  depends on the solution  $g_{nl}(r, T)$  of eq. (3.9) we have to resort to an iterative procedure. First we choose a starting value  $S^{(0)}$  for the soft scale in eq. (3.4), specific to the state and temperature, and then evaluate eq. (3.9) via a shooting method in the complex  $(E, \Gamma)$ -plane to obtain a first approximation of the wave function, energy and decay width,  $g_{nl}^{(1)}$ ,  $E_{nl}^{(1)}$  and  $\Gamma_{nl}^{(1)}$ , respectively. The so obtained solution  $g_{nl}^{(1)}$  is used to calculate the soft scale  $S_{nl}^{(1)} = \langle 1/r \rangle_{nl}^{(1)}$  which may be used together with  $E_{nl}^{(1)}$  and  $\Gamma_{nl}^{(1)}$  as initial values for the next step,

$$S^{(0)} \rightarrow g^{(1)}, S^{(1)}, E^{(1)}, \Gamma^{(1)} \rightarrow g^{(2)}, S^{(2)}, E^{(2)}, \Gamma^{(2)} \rightarrow \dots, \quad (3.10)$$

The final solution is obtained when this series in  $(g^{(n)}, S^{(n)}, E^{(n)}, \Gamma^{(n)})$  has converged to the desired degree of accuracy. Fig. 3.2 depicts the wave functions  $g_{n0}$  of the lowest lying S-states that follow from this procedure. One can see that the changes in the wave function are more pronounced for the higher excited states and that the root-mean-square (rms) radius  $\langle r^2 \rangle^{1/2}$  increases with temperature.

In this procedure, the bottom mass  $m_b$  is fixed from the zero temperature case of the ground state, where  $M_{nl}(0)$  in eq. (3.7) is set to equal the experimental  $\Upsilon(1S)$ -mass given in tab. 1.1. This yields

$$m_b = 4801 \text{ MeV}, \quad \alpha_{10}(0) = \alpha_s(1542 \text{ MeV}) = 0.3984. \quad (3.11)$$

Subsequently, for the other states and for finite temperature,  $m_b$  is held fixed at this value and both  $E$  and  $\Gamma$  are varied in order to satisfy eq. (3.9).

It has been mentioned at the end of section 2.4 that the proper choice of the potential in pNRQCD depends on the relation of soft to thermal scale. Since this phenomenological model is motivated by pNRQCD we should apply the second part of  $V_{nl}$  in eq. (3.3) only for  $\langle 1/r \rangle_{nl}(T) \ll 2\pi T$ . At low temperature, i.e. in the limit  $\langle 1/r \rangle_{nl}(T) \gg 2\pi T$ , however, we should replace the pNRQCD part in eq. (3.8) by the potential (Brambilla et al., 2008)

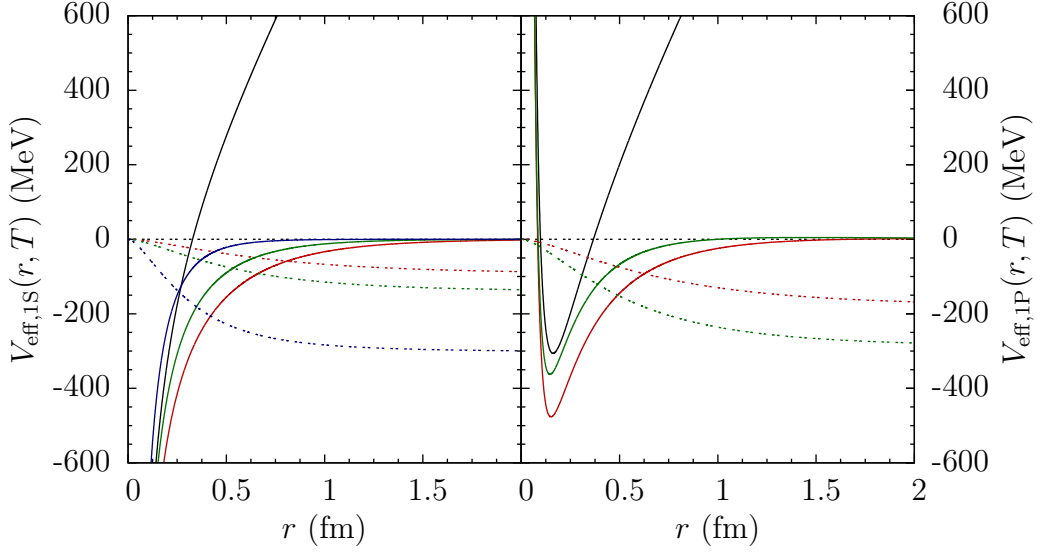


Figure 3.1: Complex bottomium interaction potential  $V_{\text{eff},nl}$  from eq. (3.8) for the  $\Upsilon(1S)$  and  $\chi_b(1P)$  states (left and right, respectively) and temperature  $T = 0$  MeV (black), 170 MeV (red), 250 MeV (green) and 500 MeV (blue). Real and imaginary parts are drawn in solid and dotted lines, respectively. The real part of the potential behaves counter intuitively at zero temperature due to the unsteady transition for  $T \rightarrow 0$ . For  $T = 500$  MeV the potential is only plotted for the 1S ground state since no excited states exist at such high temperatures.

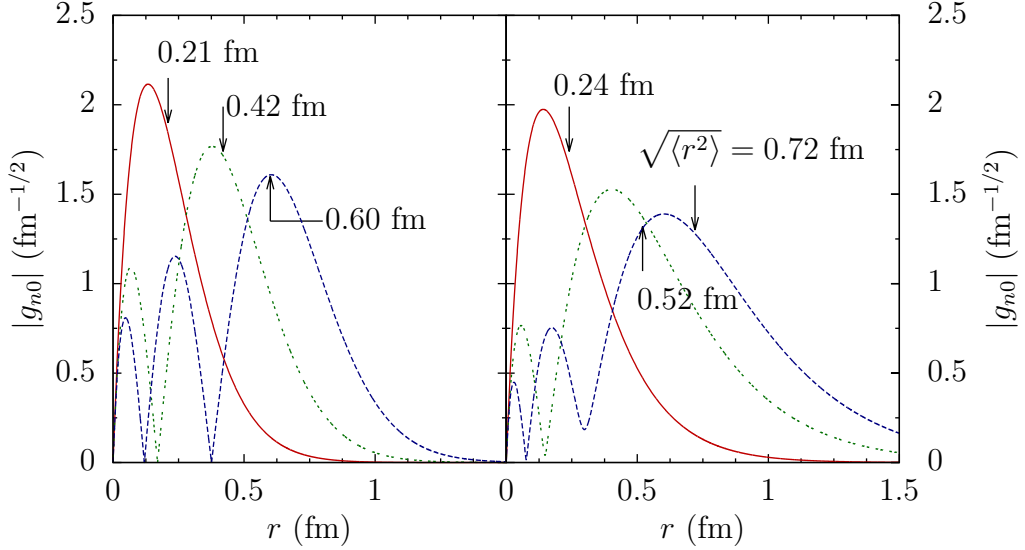


Figure 3.2: Radial wave functions of the  $\Upsilon(1S)$ ,  $\Upsilon(2S)$ ,  $\Upsilon(3S)$  states (solid, dotted, dashed curves, respectively) calculated from the Schrödinger equation (3.9) with the complex potential (3.3) for temperatures  $T = 0$  MeV (left) and 200 MeV (right). The rms radii  $\sqrt{\langle r^2 \rangle}$  of the  $\Upsilon(2S)$  and, in particular,  $\Upsilon(3S)$  state are strongly dependent on temperature, whereas the ground state remains nearly unaffected.

$$\begin{aligned}
V_{\text{eff},nl}(r, T > 0) &= \frac{l(l+1)}{m_b r^2} - \frac{\sigma}{m_D} e^{-m_D r} - \frac{C_F \alpha_{nl}}{r} \left[ 1 - \frac{N_c \alpha_{nl}}{36\pi} (2\pi r T)^2 \right. \\
&\quad \left. + \frac{3\zeta(3)}{4\pi^2} 2\pi r T (m_D r)^2 - \frac{\zeta(3) N_c \alpha_{nl}}{12\pi^3} (2\pi r T)^3 - \frac{(m_D r)^3}{6} \right] \\
&\quad - i C_F \alpha_{nl} T \left[ \frac{N_c^2 \alpha_{nl}^2}{6} - \frac{\ln 2 N_c \alpha_{nl}}{9\pi} (2\pi r T)^2 \right. \\
&\quad \left. + \frac{(m_D r)^2}{6} \left( 2 \ln \frac{T}{m_D} + 1 + 4 \ln 2 + 2 \frac{\zeta'(2)}{\zeta(2)} - 2\gamma_E \right) \right]. \quad (3.12)
\end{aligned}$$

Fig. 3.3 depicts the two potentials (3.8) and (3.12) for the  $\Upsilon(1S)$ -state. Since the limit  $r \rightarrow \infty$  of the low temperature potential (3.12) does not exist the definition (3.7) of the binding energy  $E_{nl}$  is not applicable for this potential so instead we use

$$E_{nl}(T) = M_{nl}(T) - 2m_b. \quad (3.13)$$

A comparison between the thermal scale and the soft scales as they follow from eq. (3.9) are shown in fig. 3.4. It is found that the low temperature potential (3.12) is only applicable to the  $\Upsilon(1S)$  for  $T \lesssim 230$  MeV but not for the excited states. Also the  $\Upsilon(1S)$ -wave functions that follow from the low temperature potential do not differ significantly from those of the high temperature potential (3.8) in this case.

Fig. 3.5 depicts the binding energies according to eq. (3.7) and the rms radii for all six states under consideration. For the  $\Upsilon(1S)$  the two quantities are plotted using the high and low temperature potential. While the rms radii in both cases do not differ significantly from each other, the energies values are quite different. This is, however, only due to the fact that the low temperature potential (3.12) does not vanish at infinity so the zero point is shifted. In the common picture color screening weakens the  $b\bar{b}$ -binding, causing the bound state to swell up to very large rms radii  $\sqrt{\langle r^2 \rangle}$  before it eventually dissolves. The combination of color screening and collisional damping, however, keeps  $\sqrt{\langle r^2 \rangle}$  approximately constant even down to point of dissolution at the melting temperature  $T_m$  (see tab. 3.1).

The results for the decay width  $\Gamma_{nl}$ , however, are plotted in figs. 3.8 and 3.10, where they are compared to the results for the gluodissociation decay width, that is calculated in section 3.2.

Detailed information on the temperature-dependent scales and decay widths obtained from the potential model for the different bottomium states

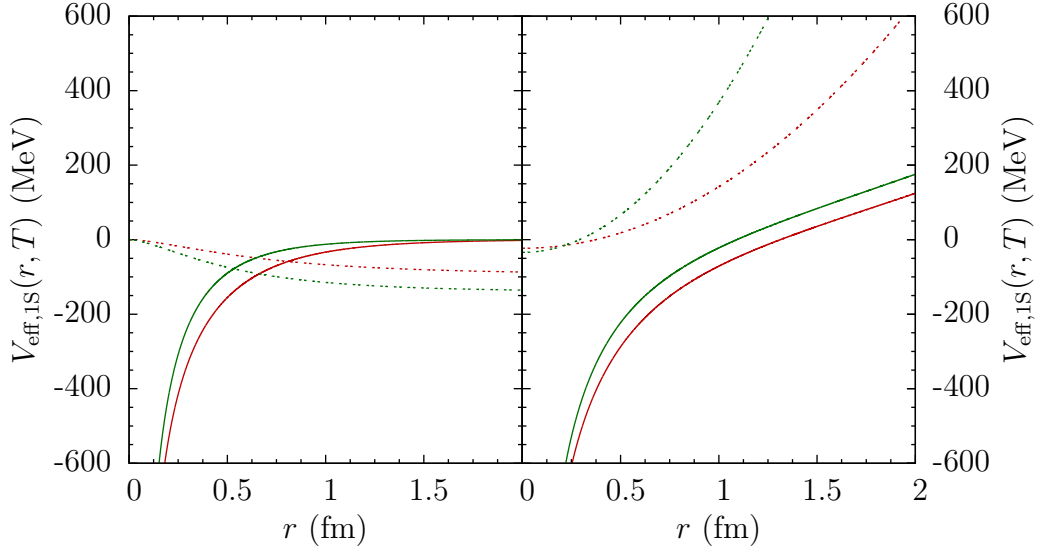


Figure 3.3: Comparison of the high and low temperature potentials (3.8) and (3.12) for the  $\Upsilon(1S)$  state (left and right, respectively) for temperature  $T = 170$  MeV (red) and  $250$  (MeV) green. Real and imaginary parts are drawn in solid and dotted lines, respectively.

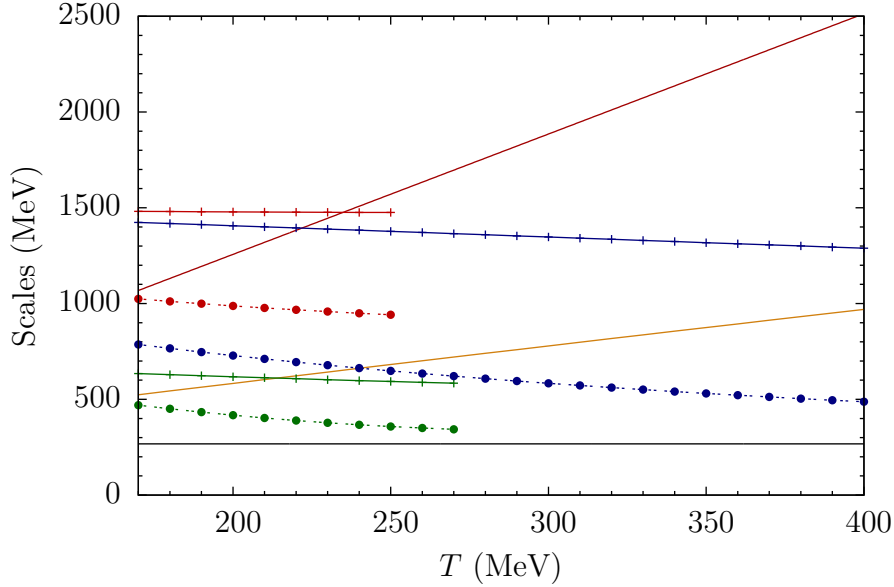


Figure 3.4: Comparison of different scales in the potential model. The thermal scale  $2\pi T$ , the Debye mass  $m_D$  and  $\Lambda_{\text{QCD}}$  are plotted in red, orange and black solid lines, respectively. Soft scales  $S_{nl}(T) = \langle 1/r \rangle_{nl}(T)$  (solid lines) and ultra soft scales  $\langle |V_{\text{eff}}| \rangle_{nl}(T)$  (dashed lines) are plotted for the  $\Upsilon(1S)$  (blue) and  $\chi_b(1P)$  (green) using the potential (3.8) and for the  $\Upsilon(1S)$  (red) using the potential (3.12) at low  $T$ .

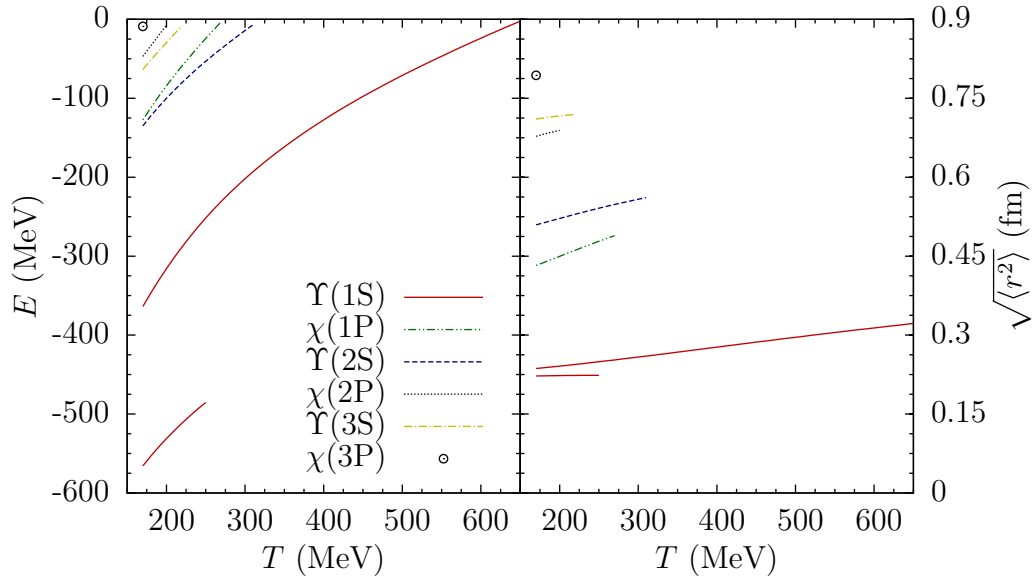


Figure 3.5: Binding energies  $E$  (left) and rms radii  $\sqrt{\langle r^2 \rangle}$  (right) of the different bottomium states as a function of temperature  $T$ . Both quantities have been calculated from the potential (3.8) for the whole  $T$ -range, using eq. (3.7) for the energy. For the  $\Upsilon(1S)$ , however, results have also been calculated for low  $T$  using the potential (3.12) and eq. (3.13) for the energy. While the energy values are strongly shifted with respect to each other due to the different zero points the effect on the rms radius is fairly small. Remarkably the combined effect of color screening and collisional damping keeps the rms radii approximately constant even for very small  $E$ .

is provided in appendix B. For the  $\Upsilon(1S)$ ,  $\chi_b(1P)$  and  $\Upsilon(2S)$  states the scale hierarchy (2.29) stays intact, with  $\langle |V_{\text{eff}}| \rangle$  replacing  $E$  as the ultra soft scale; but not so for the higher excited states. For this reason the non-perturbative string part had to be included in the interaction potentials.

## 3.2 Gluodissociation of the $\Upsilon$ meson

A long time ago Bhanot and Peskin have considered the interaction of heavy quark bound states with an external medium. One result of their work is an expression for the cross section  $\sigma_{\text{diss}}$  of the dynamic dissociation of the bound state by gluons, a process called gluodissociation. Due to the large gluon density in the fireball produced in heavy ion collisions at LHC energies, gluodissociation represents a major process contributing to the in-medium suppression of bottomia. We will derive  $\sigma_{\text{diss}}$  and the corresponding decay width  $\Gamma_{\text{diss}}$  in a generalized manner in subsection 3.2.1 and calculate finite-temperature results in subsection 3.2.2. In subsection 3.2.3 we treat the special case of Coulomb bound states.

Table 3.1: Melting temperatures  $T_m$  of the different bottomium states. Above  $T_m$  no bound state solutions to eq. (3.9) exist.

State	$T_m$ (MeV)
$\Upsilon(1S)$	655
$\chi_b(1P)$	273
$\Upsilon(2S)$	320
$\chi_b(2P)$	206
$\Upsilon(3S)$	228
$\chi_b(3P)$	$\sim 175$

It should be noted at this point that in the strict pNRQCD approach the contribution from different scales are clearly separated. Hence gluodissociation as an ultra soft processes has to be treated separately from the soft process of collisional damping that is accounted for by the potential approach. Since our phenomenological model is influenced by pNRQCD we should also treat gluodissociation separately so we do not neglect this significant contribution to the decay width.

### 3.2.1 Dissociation of bottomia in the medium

Let us consider a  $b\bar{b}$  bound state  $(n-l, l)$  with a wave function  $\psi_{nlm}$ , satisfying eq. (3.1) with one of the effective potentials  $V_{\text{eff},nl}$  from eqs. (3.8) or (3.12). The potential accounts for the soft dissociation processes of color screening and collisional damping. The latter is a result of the imaginary part of the potential and the corresponding decay width  $\Gamma_{nl}$  from section 3.1 is renamed to  $\Gamma_{\text{damp},nl}$  in the following.

Processes occurring at the ultra soft scale  $\langle |V_{\text{eff}}| \rangle$  are represented by interaction terms in the pNRQCD action (2.48) and are calculated perturbatively. At the lowest order we have the dipole interaction term

$$\frac{g}{\sqrt{2N_c}} \vec{r} \vec{E}^a (S^\dagger O^a + O^{a\dagger} S), \quad (3.14)$$

which describes the transition of a color-singlet  $b\bar{b}$  state, that might be a bound state, to a color-octet  $b\bar{b}$  state by the interaction with an ultra soft gluon. Since the color-octet potential (2.64) is repulsive, this transition corresponds to a dissociation.

In order to allow for a better comparison of our approach to the original of Bhanot and Peskin we would like to perform the following calculation in real time  $t$ , using a vacuum gluon propagator. The result for the gluodissociation

cross section  $\sigma_{\text{diss}}$  is then folded with a Bose-Einstein distribution to obtain the finite-temperature decay width  $\Gamma_{\text{diss}}$ . This procedure is possible since soft thermal processes are already encoded in the  $b\bar{b}$  wave functions.

In order to calculate the gluodissociation decay width  $\Gamma_{\text{diss}}$ , we consider the singlet and octet  $b\bar{b}$  propagators, where the singlet propagator is a solution to the Schrödinger equation (3.1) with the aforementioned potentials. The specific form of the octet potential, however, is left open for the moment. The position space propagators of the singlet and octet fields may be expressed as

$$\mathcal{S}_{fi} = \mathcal{R}_{fi} \mathcal{S}_{fi}^r, \quad \mathcal{O}_{fi}^{ab} = \delta^{ab} \mathcal{R}_{fi} \mathcal{O}_{fi}^r, \quad (3.15)$$

where  $\mathcal{S}$  and  $\mathcal{O}$  are the singlet and octet propagators, respectively,  $\mathcal{R}$  the CM propagator and  $\mathcal{S}^r$  and  $\mathcal{O}^r$  are the RM propagators. They describe the propagation of the  $b\bar{b}$  pair from the positions  $\vec{x}_{b,i}$  and  $\vec{x}_{\bar{b},i}$  at time  $t_i$  to the positions  $\vec{x}_{b,f}$  and  $\vec{x}_{\bar{b},f}$  at time  $t_f \geq t_i$  and depend on these spacetime positions in the following way:

$$\begin{aligned} \mathcal{S}_{fi} &= \mathcal{S}(t_f, \vec{x}_{b,f}, \vec{x}_{\bar{b},f}; t_i, \vec{x}_{b,i}, \vec{x}_{\bar{b},i}), \\ \mathcal{O}_{fi} &= \mathcal{O}(t_f, \vec{x}_{b,f}, \vec{x}_{\bar{b},f}; t_i, \vec{x}_{b,i}, \vec{x}_{\bar{b},i}), \\ \mathcal{R}_{fi} &= \mathcal{R}(t_f, \vec{R}_f; t_i, \vec{R}_i), \\ \mathcal{S}_{fi}^r &= \mathcal{S}^r(t_f, \vec{R}_f; t_i, \vec{R}_i), \\ \mathcal{O}_{fi}^r &= \mathcal{O}^r(t_f, \vec{R}_f; t_i, \vec{R}_i), \end{aligned} \quad (3.16)$$

where we have introduced the usual RM and CM coordinates,

$$\vec{r}_{f/i} = \vec{x}_{b,f/i} - \vec{x}_{\bar{b},f/i}, \quad \vec{R}_{f/i} = \frac{1}{2} (\vec{x}_{b,f/i} + \vec{x}_{\bar{b},f/i}). \quad (3.17)$$

The CM propagator is given by

$$\mathcal{R}_{fi} = \int \frac{d^3Q}{(2\pi)^3} e^{i\vec{Q}(\vec{R}_f - \vec{R}_i) - i\frac{\vec{Q}^2 t}{4m_b}}, \quad (3.18)$$

where we have written  $t = t_f - t_i$ . In the infinite mass limit the CM propagator approaches a  $\delta$ -function,

$$\mathcal{R}_{fi} \rightarrow \delta^3(\vec{R}_f - \vec{R}_i) \quad \text{for} \quad m_b \rightarrow \infty. \quad (3.19)$$

We may express the singlet and octet RM propagators in terms of the Schrödinger wave functions,

$$\mathcal{S}_{fi}^r = \sum_{n=1}^{\infty} \sum_{l=0}^{n-1} \sum_{m=-l}^l \psi_{nlm}(\vec{r}_f) \psi_{nlm}^*(\vec{r}_i) e^{-iE_{nl}t} + \quad (\text{continuum states}),$$

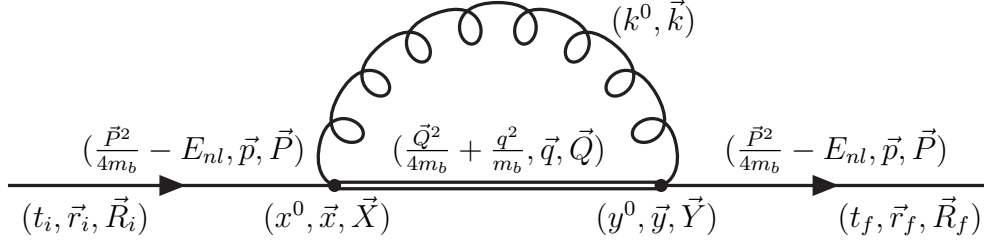


Figure 3.6: First order correction to the singlet quarkonium propagator due to the singlet-octet-transition. The single line represents a singlet and the double line an octet propagator.

$$\mathcal{O}_{fi}^r = \sum_{l=0}^{\infty} \sum_{m=-l}^l \int_0^{\infty} dq \chi_{qlm}(\vec{r}_f) \chi_{qlm}^*(\vec{r}_i) e^{-i \frac{q^2 t}{m_b}}, \quad (3.20)$$

where  $E_{nl}$  are the negative, discrete energy levels corresponding to the bound state wave function  $\psi_{nlm}(\vec{x}) = \langle \vec{x} | nlm \rangle$  from subsection 3.1 and  $q^2/m_b$  the positive, continuous energies of the scattering wave functions  $\chi_{qlm}(\vec{x}) = \langle \vec{x} | qlm \rangle$  of a repulsive potential, respectively.

For the octet wave function we now make a similar separation ansatz as in eq. (3.6) ,

$$\chi_{ql}(\vec{r}) = \frac{h_{ql}(r)}{r} Y_{lm}(\theta, \varphi). \quad (3.21)$$

These wave functions are normalized by the completeness relation,

$$\sum_{l=0}^{\infty} \sum_{m=-l}^l \int_0^{\infty} dq \chi_{qlm}(\vec{r}) \chi_{qlm}^*(\vec{r}') = \delta^3(\vec{r} - \vec{r}'), \quad (3.22)$$

which yields for the radial wave functions,

$$\int_0^{\infty} dq h_{ql}(r) h_{ql}^*(r') = \delta(r - r'). \quad (3.23)$$

The continuous part of  $\mathcal{S}^r$  has been omitted in eqs. (3.20) since only the bound state wave functions are needed in the following.

The first order correction in  $g^2$  to the singlet propagator is due to the singlet-octet dipole-vertex in eq. (2.48) and is depicted in fig. 3.6. It reads

$$\begin{aligned} \mathcal{S}_{fi}^{1-8} = & -\frac{ig^2}{2N_c} \int_{t_i}^{t_f} dx^0 dy^0 \int d^3x d^3y \mathcal{S}_{fy}^r y^i \delta^{ab} \mathcal{O}_{yx}^r x^j \mathcal{S}_{xi}^r \cdot \\ & \cdot \int d^3X d^3Y \mathcal{R}_{fy} [\partial_{x^0} \partial_{y^0} \Delta_{ij}^{ab}(y^0 - x^0, \vec{Y} - \vec{X})] \mathcal{R}_{yx} \mathcal{R}_{xi}, \end{aligned} \quad (3.24)$$

where  $g$  is evaluated at the ultra soft scale. The the ultra soft gluon propagator is given by

$$\Delta_{ij}^{ab}(x) = i\delta^{ab} \delta_{ij} \int \widetilde{dk} (\Theta(x^0) e^{ikx} + \Theta(-x^0) e^{-ikx}), \quad (3.25)$$

using  $\widetilde{dk} = d^3k/(2\pi)^3/(2|\vec{k}|)$ . In order to derive the gluodissociation cross section we have to calculate the self-energy contribution  $\Sigma$  due to the singlet-octet transition. We may calculate  $\Sigma$  from  $\mathcal{S}^{1-8}$  via

$$\begin{aligned} & -i\Sigma_{nlm}(\vec{P}) V t e^{-i(\frac{\vec{P}^2}{4m_b} + E_{nl})t} \\ & = \int d^3r_f d^3R_f d^3r_i d^3R_i e^{-i\vec{P}\vec{R}_f} \psi_{nlm}^*(\vec{r}_f) \mathcal{S}_{fi}^{1-8} \psi_{nlm}(\vec{r}_i) e^{i\vec{P}\vec{R}_i}. \end{aligned} \quad (3.26)$$

Performing the spacial integrations and using  $\delta^3(0) = V$  we obtain

$$\begin{aligned} \Sigma_{nlm} = & \frac{iC_F g^2}{t} \sum_{l'=0}^{\infty} \sum_{m'=-l'}^{l'} \int_{t_i}^{t_f} dy^0 \int_{t_i}^{y^0} dx^0 \int d^3Q dq d\widetilde{k} \vec{k}^2 |\langle nlm | \hat{r} | ql'm' \rangle|^2 \\ & \cdot \delta^3(\vec{k} + \vec{Q} - \vec{P}) \left( e^{i\Sigma_E^+(y^0-x^0)} + e^{-i\Sigma_E^-(y^0-x^0)} \right), \\ \Sigma_E^{\pm} = & \frac{\vec{P}^2 - \vec{Q}^2}{4m_b} \mp |\vec{k}| + E_{nl} - \frac{q^2}{m_b}. \end{aligned} \quad (3.27)$$

Taking the limit  $t \rightarrow \infty$  yields

$$\begin{aligned} \Sigma_{nlm} = & iC_F g^2 \sum_{l'=0}^{\infty} \sum_{m'=-l'}^{l'} \int dq d\widetilde{k} \vec{k}^2 |\langle nlm | \hat{r} | ql'm' \rangle|^2 \\ & \cdot \left( \frac{i}{\Sigma_E^+ + i0^+} - \frac{i}{\Sigma_E^- - i0^+} \right), \end{aligned} \quad (3.28)$$

where now  $\vec{P} = \vec{Q} + \vec{k}$ . The width  $\Gamma_{\text{diss}}$  for the singlet to octet plus gluon decay,  $b\bar{b}_1 \rightarrow b\bar{b}_8 + g$ , in the rest-frame of the  $b\bar{b}_1$  is given by twice the imaginary part of the self-energy, averaged over the magnetic quantum number  $m$  of the incoming state,

$$\Gamma_{\text{diss},nl} = \frac{1}{2l+1} \sum_{m=-l}^l \frac{2}{S} \text{Im} \Sigma, \quad (3.29)$$

with a symmetry factor  $S = 1$ . This yields the decay width

$$\Gamma_{\text{diss},nl} = \frac{2\pi C_F g^2}{2l+1} \sum_{m=-l}^l \sum_{l'=0}^{\infty} \sum_{m'=-l'}^{l'} \int dq d\vec{k} \vec{k}^2 |\langle nlm | \hat{r} | ql'm' \rangle|^2 \delta(\Sigma_E^-). \quad (3.30)$$

Inspecting  $\Sigma_E^\pm$  in the singlet rest-frame, where  $\vec{P} = 0$ , we see that the  $\delta$ -function in eq. (3.27) enforces

$$\Sigma_E^- = |\vec{k}| - \frac{\vec{k}^2}{4m_b} + E_{nl} - \frac{q^2}{m_b} \approx |\vec{k}| + E_{nl} - \frac{q^2}{m_b}. \quad (3.31)$$

This approximation is valid since  $|\vec{k}| \sim m_b g^4$  for ultra soft gluons, so the change in the CM-momentum due to the absorption of the gluon is negligible to this order of accuracy. Thus the CM-motion is decoupled approximately from the relative motion.

The gluodissociation cross section  $\sigma_{\text{diss}}$  is connected to  $\Gamma_{\text{diss}}$  via

$$\Gamma_{\text{diss},nl} = (N_c^2 - 1)N_c \int \frac{d^3k}{(2\pi)^3} \sigma_{\text{diss},nl}(E_g), \quad (3.32)$$

where we have renamed the gluon energy,  $E_g = |\vec{k}|$ . The factor  $(N_c^2 - 1)N_c$  accounts for the summation of outgoing gluon species and colors of the octet state included in  $\Gamma_{\text{diss}}$ . In  $\sigma_{\text{diss}}$  we keep only the average over the magnetic quantum number  $m$  of the incoming singlet state. Then, writing

$$\frac{g^2}{4\pi} = \tilde{\alpha}_{nl} = \alpha_s(\langle |V_{\text{eff},nl}| \rangle), \quad (3.33)$$

we obtain for the cross section

$$\sigma_{\text{diss},nl}(E_g) = \frac{2\pi^2 \tilde{\alpha}_{nl} E_g}{(2l+1)N_c^2} \sum_{m=-l}^l \sum_{l'=0}^{\infty} \sum_{m'=-l'}^{l'} \int_0^\infty dq |\langle nlm | \hat{r} | ql'm' \rangle|^2 \cdot \delta\left(E_g + E_{nl} - \frac{q^2}{m_b}\right). \quad (3.34)$$

Let us rewrite this expression as follows

$$\begin{aligned} \sigma_{\text{diss},nl}(E_g) &= \frac{\pi^2 \tilde{\alpha}_{nl} E_g}{N_c^2} \sqrt{\frac{m_b}{E_g + E_{nl}}} \sum_{l',m',m} \frac{|\vec{I}_{nlm}^{ql'm'}|^2}{2l+1}, \\ \vec{I}_{nlm}^{ql'm'} &= \int d^3x \psi_{nlm}^*(\vec{r}) \vec{r} \chi_{ql'm'}(\vec{r}), \end{aligned} \quad (3.35)$$

where  $q \equiv q_{nl}(E_g) = \sqrt{m_b(E_g + E_{nl})}$  is understood in the continuous indices. With wave functions  $\psi_{nlm}(\vec{r})$  and  $\chi_{ql'm'}(\vec{r})$  of the kind (3.6) and (3.21), suitable for a central potential, we can make use of the properties of the spherical harmonics to calculate the angular part of the dipole integral,

$$\begin{aligned}
& \int_{-1}^1 d \cos \theta \int_0^{2\pi} d\varphi Y_{lm}(\theta, \varphi) \vec{e}_r Y_{l'm'}^*(\theta, \varphi) \\
&= \int_{-1}^1 d \cos \theta \int_0^{2\pi} d\varphi Y_{lm}(\theta, \varphi) \left[ \frac{e^{i\varphi} \sin \theta}{2} \vec{e}_+ + \frac{e^{-i\varphi} \sin \theta}{2} \vec{e}_- + \cos \theta \vec{e}_z \right] Y_{l'm'}^*(\theta, \varphi) \\
&= \vec{e}_+ \frac{\delta_{m+1,m'}}{\sqrt{2}} \left[ \delta_{l-1,l'} \sqrt{\frac{(l-m-1)(l-m)}{(2l+1)(2l-1)}} - \delta_{l+1,l'} \sqrt{\frac{(l+m+1)(l+m+2)}{(2l+1)(2l+3)}} \right] \\
&\quad + \vec{e}_- \frac{\delta_{m-1,m'}}{\sqrt{2}} \left[ -\delta_{l-1,l'} \sqrt{\frac{(l+m-1)(l+m)}{(2l+1)(2l-1)}} + \delta_{l+1,l'} \sqrt{\frac{(l-m+1)(l-m+2)}{(2l+1)(2l+3)}} \right] \\
&\quad + \vec{e}_z \delta_{m,m'} \left[ \delta_{l-1,l'} \sqrt{\frac{(l+m)(l-m)}{(2l+1)(2l-1)}} + \delta_{l+1,l'} \sqrt{\frac{(l+m+1)(l-m+1)}{(2l+1)(2l+3)}} \right], \tag{3.36}
\end{aligned}$$

where  $\vec{e}_{\pm} = (\vec{e}_x \mp i\vec{e}_y)/\sqrt{2}$ . Inserting this expression into eqs. (3.35) and performing the sum yields

$$\begin{aligned}
\sigma_{\text{diss},nl}(E_g) &= \frac{\pi^2 \tilde{\alpha}_{nl} E_g}{N_c^2} \sqrt{\frac{m_b}{E_g + E_{nl}}} \frac{(l+1) |J_{nl}^{q,l+1}|^2 + l |J_{nl}^{q,l-1}|^2}{2l+1}, \\
J_{nl}^{q,l} &= \int_0^{\infty} dr r g_{nl}^*(r) h_{ql}(r). \tag{3.37}
\end{aligned}$$

The results obtained so far for the cross section (3.37) and decay width (3.32) are valid at zero temperature. To obtain a finite temperature decay width  $\Gamma_{\text{diss},nl}(T)$  from the zero temperature expression we need to weight the gluodissociation cross section with a suitable gluon distribution function. In fact the medium thermalizes very quickly so it seems reasonable to assume a Bose-Einstein distribution for the gluons,

$$\Gamma_{\text{diss},nl}(T) \equiv \frac{g_d}{2\pi^2} \int_0^{\infty} \frac{dE_g E_g^2 \sigma_{\text{diss},nl}(E_g)}{e^{E_g/T} - 1}, \tag{3.38}$$

where  $g_d = 16$  is number of gluon degrees of freedom. The bottomium states are thus subject to the total decay width

$$\Gamma_{\text{tot},nl}(T) = \Gamma_{\text{damp},nl}(T) + \Gamma_{\text{diss},nl}(T). \tag{3.39}$$

The collisional damping decay width obtained from eq. (3.9) is thus directly inserted into eq. (3.39) while the wave function is used to calculate the gluodissociation cross section (3.37) and decay width (3.38).

In the next subsection we will specify an octet potential and derive actual results for  $\sigma_{\text{diss}}$  and  $\Gamma_{\text{diss}}$ .

In this section we have obtained from the pNRQCD action (2.48) a generalized form of the gluodissociation cross section (3.34) that has been derived over 30 years ago in an operator product expansion (Peskin, 1979; Bhanot and Peskin, 1979). This can be made manifest by writing

$$\sigma_{\text{diss},nl}(E_g) = \frac{2\pi\tilde{\alpha}_{nl}E_g}{(2l+1)N_c^2} \cdot \sum_{m=-l}^l \text{Im} \left\{ \langle nlm | \hat{r} \frac{1}{E_g + E_{nl} - H_8 - i0^+} \hat{r} | nlm \rangle \right\}, \quad (3.40)$$

where  $H_8$  means the Hamiltonian of the intermediate octet state. Dropping now the summation over  $m$  for S-states, approximating  $H_8$  by a free Hamiltonian and taking  $|nlm\rangle$  as pure Coulomb states yields indeed the expression derived by Bhanot and Peskin (1979).

While our approach has emerged from the background of the Bhanot-Peskin result and the connection to thermal pNRQCD has only been drawn a posteriori it is inevitably similar the approach in Ghiglieri (2012); Brambilla et al. (2011), where the result (3.34) has been found independently. The difference in our approach is that the gluons are initially not treated as part of a thermal medium, i.e. the gluon propagator is represented by the vacuum expression (3.25) instead of the finite-temperature propagator of in-medium gluons. Only after the cross section is obtained a thermal average is calculated.

### 3.2.2 Gluodissociation at finite temperature

Let us now consider bottomium states in a deconfined medium where the interaction can be described by the potentials (3.8) and (3.12). We insert the numerical solutions for the radial wave functions from eq. (3.9), into eqs. (3.37). We do not consider temperature effects on the octet states, however, since we are not interested in the further evolution of the color-octet  $b\bar{b}$  state. Hence we still use the pure Coulomb octet potential from eq. (2.49) for the outgoing channel.

Results for the gluodissociation cross sections for the  $\Upsilon(1S)$ ,  $\Upsilon(2S)$ ,  $\Upsilon(3S)$  and  $\chi_b(1P)$ ,  $\chi_b(2P)$ ,  $\chi_b(3P)$  states are depicted in fig. (3.7) at the critical temperature,  $T = T_c = 170$  MeV. The critical temperature, above which the

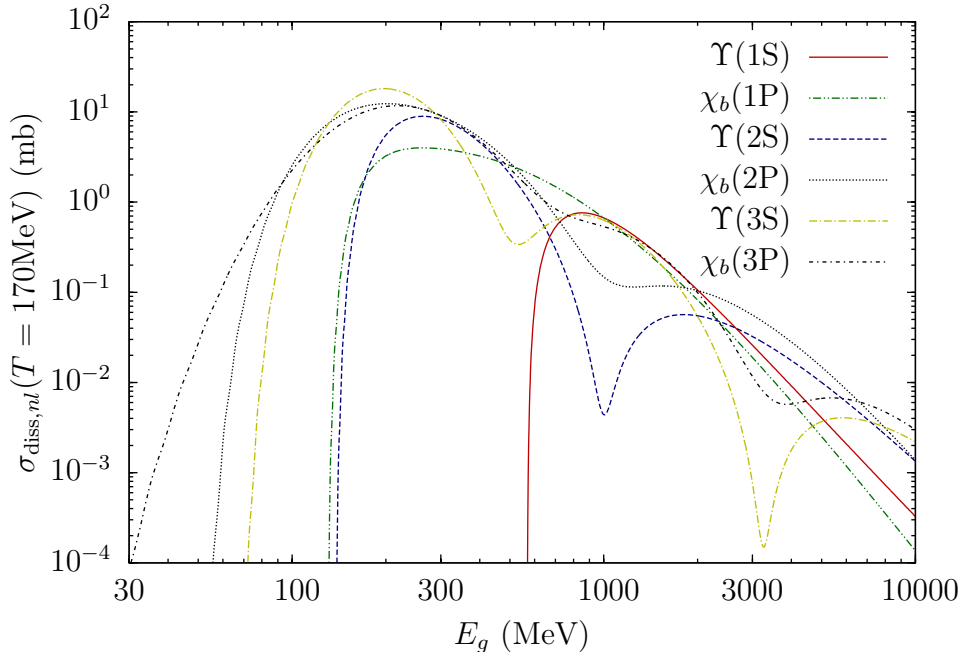


Figure 3.7: Gluodissociation cross section  $\sigma_{\text{diss},nl}$  for temperature  $T = 170$  MeV according to eqs. (3.37) using the singlet wave functions derived from eq. (3.9) for the potentials (3.8) and (3.12).

bottomium states are embedded in a QGP, is the lowest temperature that we consider in this model.

The decay widths  $\Gamma_{\text{damp},nl}$ , introduced in section 3.1, and  $\Gamma_{\text{diss},nl}$ , as obtained from eq. (3.38), are displayed in fig. 3.8. It is evident that both processes, collisional damping and gluodissociation, are important. For the excited states, however, the larger part of the total width originates from collisional damping. Whereas  $\Gamma_{\text{damp}}$  increases almost linearly with temperature,  $\Gamma_{\text{diss}}$  depends on the overlap of the gluodissociation cross section with the thermal gluon distribution. While the peak of the Bose-Einstein distribution moves to larger gluon energies with increasing temperature the opposite is the case for the shape of the cross sections (see fig. 3.9). In previous studies, where the running of the coupling was not considered in the Schrödinger equation, this behavior had made itself manifest in the shape of the width (Brezinski and Wolschin, 2012; Nendzig and Wolschin, 2013). Due to the decreasing binding energies at higher temperature, the cross section increased but its peaks also moved to lower temperatures such that the resulting width had achieved a maximum at a certain temperature. In the present model, however, the decreasing ultra soft scale enhances the coupling at higher temperatures so this behavior is obscured in the shape of the width. Only for the  $\chi_b(2P)$  and  $\Upsilon(3S)$  the shape of  $\Gamma_{\text{diss}}$  tends towards a maximum value as

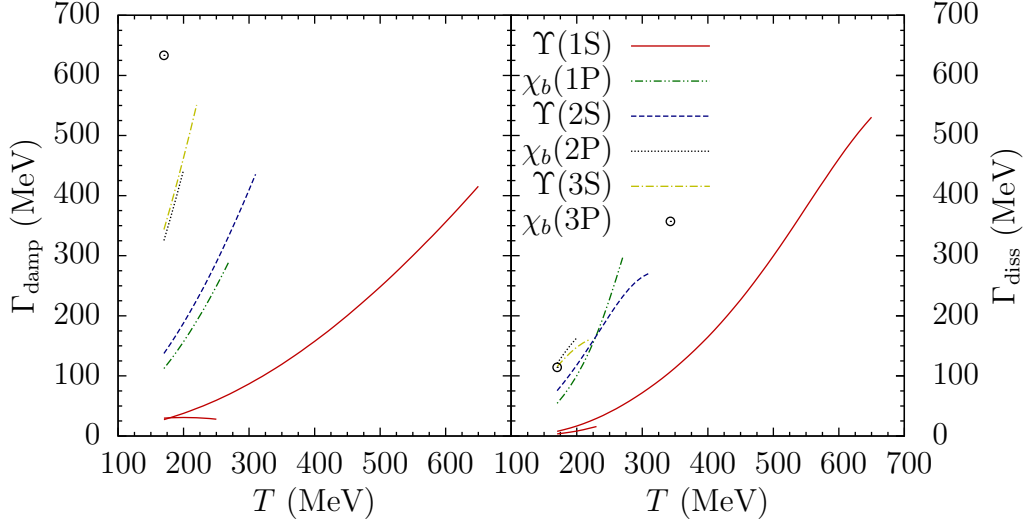


Figure 3.8: Partial decay widths  $\Gamma_{\text{damp}}$  as obtained from the Schrödinger equation (3.9) and  $\Gamma_{\text{diss}}$  as given in eq. (3.38) are plotted versus temperature  $T$  for the bottomium states  $\Upsilon(1S)$ ,  $\Upsilon(2S)$ ,  $\Upsilon(3S)$  and  $\chi_b(1P)$ ,  $\chi_b(2P)$ ,  $\chi_b(3P)$ . The  $\Upsilon(1S)$ -decay widths are plotted with the potential (3.12) at low  $T$  and with the potential (3.8) for the whole  $T$ -range.

the melting temperature  $T_m$  is approached.

Fig. 3.10 depicts the total width,  $\Gamma_{\text{tot}} = \Gamma_{\text{damp}} + \Gamma_{\text{diss}}$ , that will be combined with the results of the hydrodynamical fireball model (chapter 4) to calculate the amount of suppression of the  $\Upsilon(1S)$  ground state and the  $\Upsilon(2S)$ ,  $\Upsilon(3S)$  excited states (chapter 5 and 6).

### 3.2.3 Gluodissociation of pure Coulomb states

In this subsection we consider gluodissociation of bottomia at zero temperature using pure Coulomb potentials. This interesting special case serves as a reference for the behavior of the gluodissociation cross section for finite temperature and it enables a closer comparison to the original results of Bhanot and Peskin (1979).

The singlet and octet potentials are given by eqs. (2.49) in this case and the corresponding Coulomb wave functions read

$$\begin{aligned}
 g_{nl}(r) &= \sqrt{\frac{k_n}{n} \frac{(n+l)!}{(n-l-1)!} \frac{(2k_n r)^{l+1}}{(2l+1)!}} e^{-k_n r} M(l+1-n, 2l+2, 2k_n r), \\
 h_{ql}(r) &= \frac{|\Gamma(l+1+iz_q)|}{\sqrt{2\pi}} \frac{(2qr)^{l+1}}{(2l+1)!} e^{-iqr-\pi z_q/2} M(l+1-iz_q, 2l+2, 2iqr),
 \end{aligned} \tag{3.41}$$

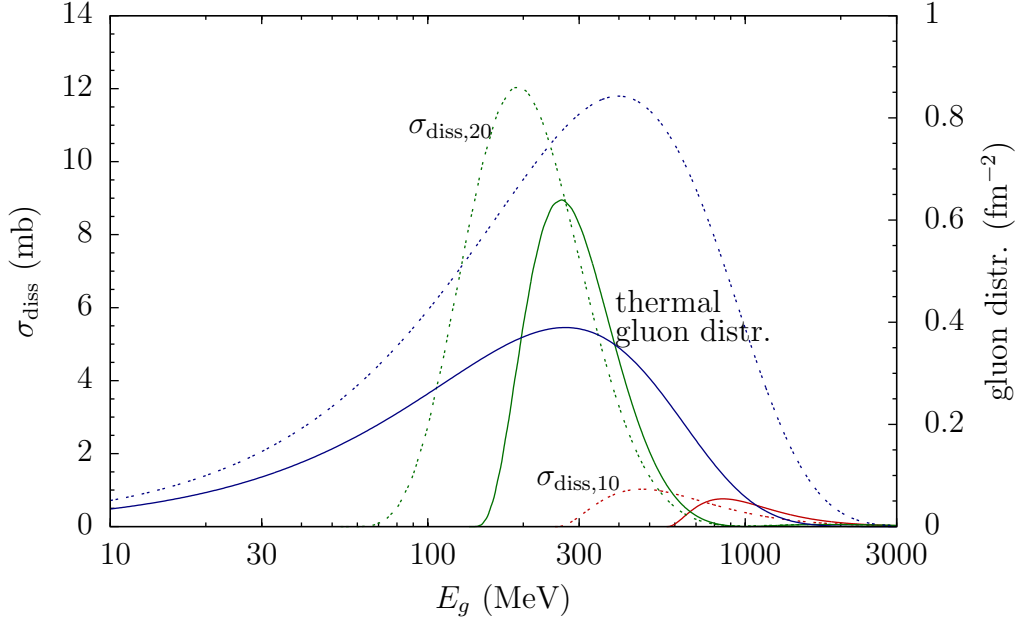


Figure 3.9: Gluodissociation cross sections  $\sigma_{\text{diss}}$  (left scale) of the  $\Upsilon(1S)$  and  $\Upsilon(2S)$  states (red and green lines, respectively) for temperatures  $T = 170$  (solid curves) and  $250$  MeV (dotted curves) as functions of the gluon energy  $E_g$ . The thermal gluon distribution (right scale; solid for  $T = 170$  MeV, dotted for  $250$  MeV) is used to obtain the decay width  $\Gamma_{\text{diss}}$  according to eq. (3.38). The shapes of the cross sections move to lower energies and the shape of the gluon distribution to higher energies as the temperature increases.

where the Kummer function  $M$  is defined as

$$M(a, b, x) = \sum_{j=0}^{\infty} \frac{\Gamma(a+j)}{\Gamma(a)} \frac{\Gamma(b)}{\Gamma(b+j)} \frac{x^j}{j!}. \quad (3.42)$$

For Coulomb states the binding energy and the coupling (3.4) are both independent of the angular momentum quantum number  $l$ ,

$$E_{nl} = E_n = -\epsilon_n, \quad \alpha_{nl} = \alpha_n. \quad (3.43)$$

The variables in eq. (3.41) then read

$$k_n = \frac{m_b C_F \alpha_n}{2n}, \quad z_q = \frac{m_b \alpha_n}{4N_c q}. \quad (3.44)$$

The coupling  $\alpha_n$  is evaluated at the soft scale  $S_n = k_n$  of the singlet state. Subsequently, the same  $\alpha_n$  is used to calculate the octet wave functions. This is because octet states emerge from the dissociation of a singlet state so at last initially the couplings should be comparable.

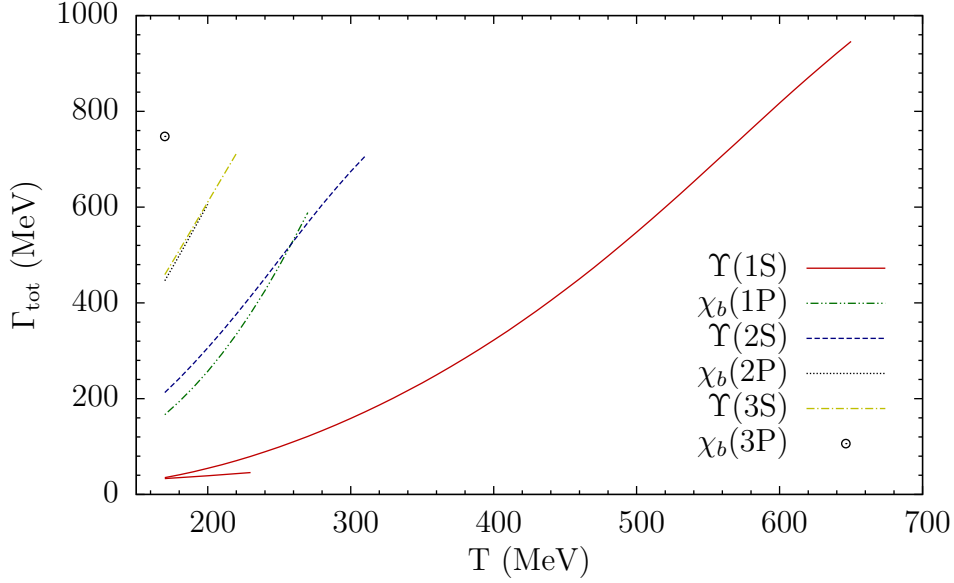


Figure 3.10: Total decay width,  $\Gamma_{\text{tot}} = \Gamma_{\text{damp}} + \Gamma_{\text{diss}}$ , plotted for the different bottomium states. The  $\Upsilon(1S)$ -width is again plotted for both potentials (3.8) and (3.12). The large widths will cause the dissolution of all excited states wherever a QGP is formed. Only the ground state  $\Upsilon(1S)$  is stable enough so that a sizable fraction can survive the QGP in the more central regions of a collision.

Let us now make the definitions

$$\begin{aligned} \epsilon_n &= m_b \left( \frac{C_F \alpha_n}{2n} \right)^2, & x_n &= k_n r, \\ Q_n &= \sqrt{\frac{E_g}{\epsilon_n}} - 1, & z_q \equiv z_n &= \frac{n}{(N_c^2 - 1)Q_n}, \end{aligned} \quad (3.45)$$

so that, for S-states, the first line of eqs. (3.37) may be reformulated to yield

$$\sigma_{\text{diss},n0} = \frac{\pi^2 \tilde{\alpha}_{n0}}{N_c^2 k_n^2} \frac{1 + Q_n^2}{Q_n} |k_n^{3/2} J_{n0}^{q1}|^2, \quad (3.46)$$

where  $q = k_n Q_n$  is understood in the indices. To calculate the cross section for the  $\Upsilon(1S)$ ,  $\Upsilon(2S)$  and  $\Upsilon(3S)$  we write down the necessary radial wave functions in terms of these new variables

$$\begin{aligned} g_{10}(r) &= 2\sqrt{k_1} x_1 e^{-x_1}, \\ g_{20}(r) &= 2\sqrt{k_2} (x_2 - x_2^2) e^{-x_2}, \\ g_{30}(r) &= 2\sqrt{k_3} \left( x_3 - 2x_3^2 + \frac{2}{3}x_3^3 \right) e^{-x_3}, \end{aligned}$$

$$h_{q1}(r) = \frac{|\Gamma(2 + iz_n)|}{\sqrt{2\pi} \Gamma(4)} (2Q_n x_n)^2 e^{-iQ_n x_n - \pi z_n/2} \cdot M(2 - iz_n, 4, 2iQ_n x_n). \quad (3.47)$$

To draw the connection to the result of Bhanot and Peskin, we approximate the octet wave function  $h_{q1}$  by a free wave function,  $z_n = 0$ , which yields

$$h_{q1}(r) = \sqrt{\frac{2}{\pi}} Q_n x_n j_1(Q_n x_n). \quad (3.48)$$

The resulting cross section for the  $\Upsilon(1S)$  reads

$$\varrho \equiv \sigma_{\text{diss},10} \Big|_{z_1=0} = \frac{512\pi \tilde{\alpha}_{10}}{N_c^2 k_1^2} \frac{Q_1^3}{(1 + Q_1^2)^5}. \quad (3.49)$$

Replacing further  $\tilde{\alpha}_{10} \rightarrow \alpha_{10}$  in eq. (3.49) and performing the large  $N_c$  limit we indeed recover the original result of Bhanot and Peskin (1979) for the 1S-state. These simplifications are not necessary, however, since we can just as well derive closed expressions for the cross section if  $z_n \neq 0$ , using the octet wave functions from eqs. (3.47).

Let us calculate the non-dimensional overlap integrals  $|k_n^{3/2} J_{n0}^{q1}|^2$  using the following integral representation of the Kummer function (Abramowitz and Stegun, 1968):

$$M(a, b, z) = \frac{\Gamma(b)}{\Gamma(b-a)\Gamma(a)} \int_0^1 dt e^{zt} t^{a-1} (1-t)^{b-a-1}, \quad (3.50)$$

which is valid for  $\text{Re } b > \text{Re } a$ . The overlap integrals may thus be written as

$$|k_n^{3/2} J_{n0}^{q1}|^2 = \frac{e^{-\pi z_n}}{2\pi} \frac{(2Q_n)^4}{|\Gamma(2 + iz_n)|^2} \cdot \left| \int_0^\infty dx_n x_n^3 k_n^{-1/2} g_{n0}(r) \int_0^1 dt e^{-iQ_n x_n(1-2t)} t^{1-iz_n} (1-t)^{1+iz_n} \right|^2. \quad (3.51)$$

We can perform the  $x$ -integration so the  $t$ -integral obtains a denominator,

$$(1 + iQ_n - 2iQ_n t)^j, \quad j = 5, 6, 7. \quad (3.52)$$

The  $t$ -integration can also be done in closed form (index  $n$  suppressed),

$$\int_0^1 dt \frac{t^{1-iz} (1-t)^{1+iz}}{(1 + iQ - 2iQt)^j} = \frac{|\Gamma(2 + iz)|^2}{\Gamma(j)(1 + Q^2)^{j-2}} \left( \frac{1 + iQ}{1 - iQ} \right)^{-iz} \quad (3.53)$$

$$\cdot \begin{cases} 2(2 + Qz), & j = 5 \\ 4(5 + 5zQ - Q^2 + z^2Q^2), & j = 6 \\ 4(30 + 45zQ - 18Q^2 + 18z^2Q^2 - 7zQ^3 + 2z^3Q^3), & j = 7 \end{cases} \quad (3.54)$$

For the  $\Upsilon(1S)$  we then obtain the following expression for the cross section, that has been found independently by Brambilla et al. (2011) and Brezinski and Wolschin (2012):

$$\begin{aligned} \sigma_{\text{diss},10} &= \varrho \cdot \left(1 + \frac{1}{2}Q_1z_1\right)^2 \frac{2\pi z_1(1+z_1^2) e^{4z_1 \arctan Q_1}}{e^{2\pi z_1} - 1} \\ &= \frac{289\pi^2 \tilde{\alpha}_{10}}{18k_1^2} \frac{Q_1^2 + \frac{1}{64}}{(1+Q_1^2)^5} \frac{e^{\arctan(Q_1)/(2Q_1)}}{e^{\pi/(4Q_1)} - 1}, \end{aligned} \quad (3.55)$$

and for the  $\Upsilon(2S)$ ,

$$\begin{aligned} \sigma_{\text{diss},20} &= \frac{8192\pi \tilde{\alpha}_{20}}{9k_2^2} \frac{Q_2^3}{(1+Q_2^2)^7} \left(1 + \frac{9}{8}Q_2z_2 + \frac{1}{4}Q_2^2z_2^2 - \frac{1}{2}Q_2^2 - \frac{1}{8}Q_2^3z_2\right)^2 \\ &\quad \cdot \frac{2\pi z_2(1+z_2^2) e^{4z_2 \arctan Q_2}}{e^{2\pi z_2} - 1} \\ &= \frac{6889\pi^2 \tilde{\alpha}_{20}}{9k_2^2} \frac{Q_2^2 + \frac{1}{16}}{(1+Q_2^2)^7} \left(1 - \frac{34}{83}Q_2^2\right)^2 \frac{e^{\arctan(Q_2)/Q_2}}{e^{\pi/(2Q_2)} - 1}. \end{aligned} \quad (3.56)$$

For the  $\Upsilon(3S)$  we have

$$\begin{aligned} \sigma_{\text{diss},30} &= \frac{61952\pi \tilde{\alpha}_{30}}{9k_3^2} \frac{Q_3^3}{(1+Q_3^2)^9} \left(1 + \frac{41}{22}Q_3z_3 + \frac{10}{11}Q_3^2z_3^2 + \frac{4}{33}Q_3^3z_3^3 \right. \\ &\quad \left. - \frac{18}{11}Q_3^2 - \frac{41}{33}Q_3^3z_3 - \frac{2}{11}Q_3^4z_3^2 + \frac{3}{11}Q_3^4 + \frac{1}{22}Q_3^5z_3\right)^2 \\ &\quad \cdot \frac{2\pi z_3(1+z_3^2) e^{4z_3 \arctan Q_3}}{e^{2\pi z_3} - 1} \\ &= \left(\frac{2581\pi}{16}\right)^2 \frac{2\tilde{\alpha}_{30}}{3k_3^2} \frac{Q_3^2 + \frac{9}{64}}{(1+Q_3^2)^9} \left(1 - \frac{2996}{2581}Q_3^2 + \frac{408}{2581}Q_3^4\right)^2 \\ &\quad \cdot \frac{e^{3 \arctan(Q_3)/(2Q_3)}}{e^{3\pi/(4Q_3)} - 1}. \end{aligned} \quad (3.57)$$

These results are plotted in fig. (3.11) for the parameter values used in chapter 3.1 together with the Bhanot-Peskin-like function  $\varrho$ . For the  $\Upsilon(1S)$  the insertion of an octet eigenstate instead of a free  $b\bar{b}$  state causes a relative deviation peaking at  $\sim 22\%$  and approaching  $1 - (17/16)^2 \approx 13\%$ . One can further see from fig. 3.11 that in this calculation the binding energy for the

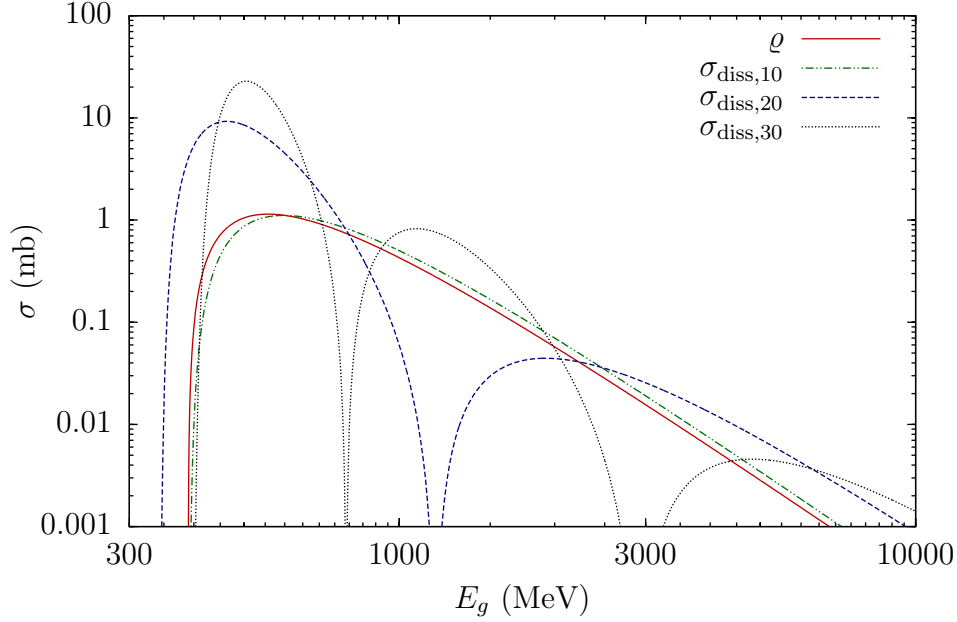


Figure 3.11: Comparison of the gluodissociation cross sections from eqs. (3.49) and (3.55)-(3.57) as they apply to pure Coulomb states with the potentials (2.49). The cross section  $\rho$  is computed for free octet states and is closely related to the Bhanot-Peskin result.

$\Upsilon(3S)$  is indeed larger than for the  $\Upsilon(1S)$ . This fact is due to the increase of the coupling constant  $\alpha_n$  with decreasing soft scale  $\langle 1/r \rangle_n$  and clearly shows that this formalism does not apply to highly excited states like the  $\Upsilon(3S)$  for pure Coulomb potentials (2.49) at zero-temperature. At finite temperature, using the potentials (3.8) and (3.12), on the other hand, figs. 3.5 and 3.7 show that the binding energy decreases with increasing principal quantum number  $n$  as expected.

It is worth to note that the gluodissociation cross section  $\sigma_{\text{diss},10}$  has been calculated for 1S Coulomb bound states at next-to-leading order (NLO) by Song and Lee (2005); Park et al. (2007). Liu et al. (2013), on the other hand, have calculated  $\sigma_{\text{diss},10}$  beyond the dipole approximation. While the resulting effect is indeed significant at  $T = T_c$  it decreases with increasing temperature.

# Chapter 4

## Relativistic hydrodynamics

In chapter 3 we have obtained results for the temperature dependent decay widths for bottomium dissociation in a QGP. In order to make use of these results we have to model the so called fireball, which is produced in relativistic PbPb collisions at the LHC.

In section 4.1 we introduce the equations of motion of a perfect, relativistic fluid. Then in section 4.2 we define a coordinate system which expands in time, parallel to the beam axis, such that it co-moves with the fireball medium in the longitudinal direction. This will give a good starting point to discretize the equations of motion and set up a numerical routine in section 4.3. Together with suitable initial conditions, introduced in section 4.4, this routine yields time-dependent profiles of temperature and transverse expansion velocity.

### 4.1 The fluid equations of motion

We will now introduce the basic hydrodynamical equations governing the expansion of the fireball. For the purpose of this thesis it will suffice to model the fireball as a relativistic perfect fluid consisting of gluons and light up-, down- and strange-quarks which are treated as massless.

The derivation of the equations of motion is performed here only very briefly. For a more detailed description the reader is referred to e.g. Yagi et al. (2008). Due to the different coordinate systems used we rely partially on coordinate-free formulations. For this purpose we make use of some concepts of differential geometry. More information on these two issues can be found in Misner et al. (1973).

The energy-momentum tensor of a relativistic, perfect fluid reads

$$T = (\varepsilon + P)u \otimes u + P, \tag{4.1}$$

where  $\varepsilon$  is the fluid's internal energy density,  $P$  the pressure and  $u$  the fluid four-velocity. From the energy-momentum tensor we may derive the equations of motion by means of the principle of energy conservation, or rather four-momentum conservation. This means that the divergence of  $T$  has to vanish,

$$\nabla \cdot T = 0, \quad (4.2)$$

where  $\nabla$  means the covariant derivative. Given a coordinate basis  $\{x^\mu\}$  and a metric  $g = (g_{\mu\nu})$ , we take the energy-momentum tensor in the form  $T = (T^\mu{}_\nu)$ , so that eq. (4.2) may be written in component notation as

$$\partial_\mu T^\mu{}_\nu + \Gamma^\mu{}_{\mu\alpha} T^\alpha{}_\nu - \Gamma^\alpha{}_{\mu\nu} T^\mu{}_\alpha = 0, \quad (4.3)$$

where the connection is given here by the Christoffel symbols  $\Gamma$ , the pendant to  $gA$  in the gauge-covariant derivative.<sup>1</sup>

The Christoffel symbols are defined such that the covariant derivative of the metric vanishes,  $\nabla_\alpha g_{\mu\nu} = 0$ , which implies

$$\Gamma^\alpha{}_{\mu\nu} = \frac{1}{2} g^{\alpha\beta} (\partial_\mu g_{\beta\nu} + \partial_\nu g_{\beta\mu} - \partial_\beta g_{\mu\nu}). \quad (4.4)$$

Inserting eq. (4.4) into eq. (4.3) yields

$$\partial_\mu T^\mu{}_\nu + T^\mu{}_\nu \partial_\mu \ln \det \sqrt{|g|} = \frac{1}{2} T^{\mu\alpha} \partial_\nu g_{\mu\alpha}, \quad (4.5)$$

where we have used the symmetry of the energy-momentum tensor together with

$$\Gamma^\mu{}_{\mu\alpha} = \frac{1}{2} g^{\mu\beta} \partial_\alpha g_{\mu\beta} = \frac{1}{2} \text{Tr}(g^{-1} \partial_\alpha g) = \frac{1}{2} \partial_\alpha \text{Tr} \ln |g|. \quad (4.6)$$

Making now use of the identity

$$\text{Tr} \ln M = \ln \det M, \quad (4.7)$$

valid for a general matrix  $M$  with non-vanishing determinant, we obtain eq. (4.5). Let us further rewrite eq. (4.5) to read

$$\frac{1}{\sqrt{|\det g|}} \partial_\mu \left( \sqrt{|\det g|} T^\mu{}_\nu \right) = \frac{1}{2} T^{\mu\alpha} \partial_\nu g_{\mu\alpha}. \quad (4.8)$$

---

<sup>1</sup>Compare with e.g. eq. (2.6) or the first line of eqs. (2.47).

This equation represents a good starting point once a specific coordinate system has been chosen. But let us now return again to the coordinate-free notation for a moment.

The equations of motion are obtained by inserting eq. (4.1) into eq. (4.2),

$$\begin{aligned} \nabla \cdot ((\varepsilon + P)u \otimes u) = \\ u \nabla \cdot ((\varepsilon + P)u) + (\varepsilon + P)\nabla_u u = -\nabla P, \end{aligned} \quad (4.9)$$

where we have introduced the directional derivative  $\nabla_u = u \cdot \nabla$ . Projecting eq. (4.2) parallel and perpendicular to the fluid four-velocity yields the energy and Euler equations, respectively,

$$\begin{aligned} u \cdot (\nabla \cdot T) = 0 & \Leftrightarrow \nabla_u \varepsilon = -(\varepsilon + P)\Theta, \\ h \cdot (\nabla \cdot T) = 0 & \Leftrightarrow (\varepsilon + P)\nabla_u u = -h \cdot \nabla P, \end{aligned} \quad (4.10)$$

where we have defined the four-volume expansion  $\Theta = \nabla \cdot u$  and the projector  $h = 1 + u \otimes u$ . Both eqs. (4.9) and (4.10) could be used for further hydrodynamical calculations. However, we would rather combine the two sets to form yet another set of four independent equations. Hence we consider both sets in the following steps.

The system of equations of motion, either in the form of eq. (4.9) or eqs. (4.10), is closed by adding the equation of state, appropriate for a perfect, relativistic fluid,

$$P = c_s^2 \varepsilon, \quad c_s = \frac{1}{\sqrt{3}}, \quad \varepsilon = \varepsilon_0 T^4. \quad (4.11)$$

Eq. (4.9) may then be reformulated as follows:

$$\nabla \cdot (T^4 u \otimes u) = -\frac{1}{4} \nabla T^4, \quad (4.12)$$

whereas eqs. (4.10) read

$$\begin{aligned} \nabla \cdot (T^3 u) = 0, \\ \nabla_u (T u) + \nabla T = 0. \end{aligned} \quad (4.13)$$

Since the entropy density is given by  $s = s_0 T^3$  for the equation of state (4.11) it becomes apparent that the first line of eqs. (4.13) expresses the conservation of entropy along the fluid worldlines as is typical for a perfect fluid.

From eq. (4.8) we infer that eq. (4.12) may be written in the index notation as follows:

$$\frac{1}{\sqrt{|\det g|}} \partial_\mu (\sqrt{|\det g|} T^4 u^\mu u_\alpha) = -\frac{1}{4} \partial_\alpha T^4 + \frac{1}{2} T^4 u^\mu u^\nu \partial_\alpha g_{\mu\nu}, \quad (4.14)$$

while eqs. (4.13) read

$$\begin{aligned}\partial_\mu(\sqrt{|\det g|} T^3 u^\mu) &= 0, \\ u^\mu \partial_\mu(T u_\alpha) + \partial_\alpha T &= \frac{1}{2} T u^\mu u^\nu \partial_\alpha g_{\mu\nu}.\end{aligned}\quad (4.15)$$

With the two sets of equations (4.14) and (4.15), we can now proceed by specifying a suitable reference frame in order to perform the actual hydrodynamical calculations.

## 4.2 The longitudinally co-moving frame

Let us consider two Pb-ions colliding in the laboratory frame (LF). The hot fireball produced in these relativistic heavy ion collisions is rapidly expanding along the beam axis, which represents the symmetry axis of this system. Only gradually the high temperature of the medium drives the transverse expansion of the fireball. While the transverse extend of the Pb-ions is approximately  $2R_{\text{Pb}}$ , they are strongly Lorentz contracted along the beam axis to form “pancakes” of thickness  $2R_{\text{Pb}}/\gamma_{\text{beam}}$ . In a two-parameter Wood-Saxon model (de Vries et al., 1987) and for LHC PbPb collisions at  $\sqrt{s_{NN}} = 2.76$  TeV we have

$$R_{\text{Pb}} = 6.62 \text{ fm}, \quad \gamma_{\text{beam}} = 1476, \quad \frac{R_{\text{Pb}}}{\gamma_{\text{beam}}} \approx 4 \cdot 10^{-3} \text{ fm}. \quad (4.16)$$

Hence the location along the beam axis as well as the moment of the collision are essentially localized in the LF. Let us now define coordinates  $(x^0, x^1, x^2, x^3)$  for the LF. The  $x^3$ -axis is chosen to coincide with the beam axis, where  $x^3 = 0$  is positioned at the center of the collision. The time coordinate  $x^0$  is chosen with  $x^0 = 0$  at the moment of the collision. The fireball has an almond-like shape in the transverse plane and the  $x^1$ - and  $x^2$ -axis are chosen as depicted in fig. 4.1.

In the model of Bjorken (1983) the fireball expands only in the longitudinal direction, i.e. transverse components of the fluid velocity are set to vanish. Hence physical fields, like temperature, particle populations etc. are homogenous in the transverse plane. The medium experiences a Hubble like longitudinal expansion with velocity  $v^3$  and rapidity  $y$ ,

$$v^3 = \tanh y = \frac{x^3}{x^0}, \quad (4.17)$$

as measured in the LF. Hence every fluid element sees all other fluid elements recede with a velocity proportional to the distance along the beam axis. The

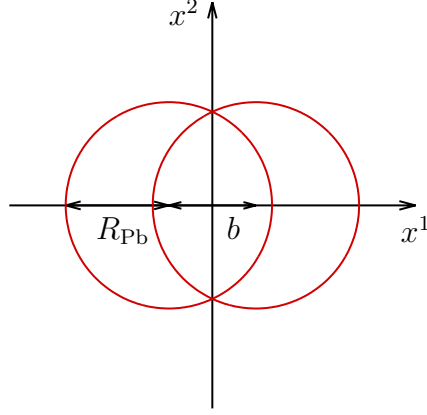


Figure 4.1: Sketch of the collision geometry in the transverse plane of PbPb collisions with Wood-Saxon radius  $R_{\text{Pb}}$ , impact parameter  $b$  and the  $x^1$ ,  $x^2$  coordinates.

four-velocity of a fluid element, as measured in the LF, may then be written as

$$u_{\parallel} = \cosh(y) e_0 + \sinh(y) e_3. \quad (4.18)$$

According to eq. (4.17) the particles in the plasma should be strictly sorted by their rapidity  $y$  along the beam axis at every instant of time. This assumption is valid due to the small spatial extension of the system along the beam axis in the momentum of the collision. Longitudinal relative velocities can only be of the order  $2R_{\text{Pb}}/(\gamma_{\text{beam}}x^0)$ . This is already fairly small at times  $x^0 \sim 0.1 \text{ fm}/c$  where we expect bottomium states to be formed. Hence we consider all sorts of particles, be they light or heavy, to be co-moving with the fluid in the beam direction.

Let us now introduce another coordinate system  $(\tau, x^1, x^2, y)$ , the longitudinally co-moving frame (LCF), which utilizes the fact that the rapidity  $y$  is a bijective function of  $x^3$ . The velocity component  $v^3$  vanishes locally in this frame, i.e. the LCF stretches along the beam axis such that it co-moves with the longitudinal motion of each individual fluid element. The tetrad of the of the LCF thus reads

$$e_{\tau} = u_{\parallel}(y), \quad e_y = \partial_y u_{\parallel}(y), \quad (4.19)$$

while  $e_1$  and  $e_2$  stay the same as in the LF. Consider now the worldline  $L$  of a given fluid element which passes through the event  $(\tau, x^1, x^2, y)$ ,

$$L(\tau, x^1, x^2, y) = \tau e_{\tau}(y) + x^1 e_1 + x^2 e_2. \quad (4.20)$$

We may derive from the total differential  $dL$  of this expression a metric  $g$ , which is valid on the future light cone of the collision plane,

$$\begin{aligned} g &= \eta(dL, dL) = -d\tau^2 + \tau^2 dy^2 + g_{\perp}, \\ g_{\perp} &= (dx^1)^2 + (dx^2)^2, \end{aligned} \quad (4.21)$$

where  $\eta$  is the Minkowski metric,

$$\eta = -(dx^0)^2 + (dx^1)^2 + (dx^2)^2 + (dx^3)^2. \quad (4.22)$$

In these coordinates the determinant of the metric becomes

$$\det g = -\tau^2 \det g_{\perp}. \quad (4.23)$$

In a realistic situation the fireball will also expand in the transverse direction of course. The corresponding fluid velocity  $u$  is then obtained from  $u_{\parallel}$  by an active boost,

$$\begin{aligned} u &= \gamma_{\perp}(e_{\tau} + v^1 e_1 + v^2 e_2), \\ \gamma_{\perp} &= \frac{1}{\sqrt{1 - (v^1)^2 - (v^2)^2}}. \end{aligned} \quad (4.24)$$

Note that with this definition the same transverse velocity components  $v^1$  and  $v^2$  are measured in the LCF as well as the LF. Hence experimental results on  $p_T$ -dependent quantities measured in the LF can be directly transferred to the LCF where the numerical results are obtained and vice versa.

With the metric (4.21) and the fluid velocity (4.24), we have  $\det g_{\perp} = 1$  so the equations of motion (4.13) read

$$\begin{aligned} \partial_{\tau}(\tau T^3 \gamma_{\perp}) + \partial_1(\tau T^3 \gamma_{\perp} v^1) + \partial_2(\tau T^3 \gamma_{\perp} v^2) &= 0, \\ \partial_y T &= 0, \\ \gamma_{\perp}(\partial_{\tau} + v^1 \partial_1 + v^2 \partial_2)(T \gamma_{\perp} v^1) + \partial_1 T &= 0, \\ \gamma_{\perp}(\partial_{\tau} + v^1 \partial_1 + v^2 \partial_2)(T \gamma_{\perp} v^2) + \partial_2 T &= 0. \end{aligned} \quad (4.25)$$

In the Bjorken model, where we have vanishing transverse expansion,  $v^1 = v^2 = 0$ , eqs. (4.25) yield the solution

$$T(\tau, x^1, x^2, y) = T(\tau) = T_0 \left( \frac{\tau_0}{\tau} \right)^{1/3}. \quad (4.26)$$

For the important special case of a central collision Gubser and Yarom have found an analytical solution to eqs. (4.25). In this case the fireball has cylindrical symmetry about the  $x^3$ -axis so we can use polar coordinates  $(R, \varphi)$  in

the transverse plane and have  $v^\varphi = 0$  for symmetry reasons. The determinant of the transverse metric in eq. (4.23) then reads  $\det g_\perp = R^2$  and eqs. (4.25) become

$$\begin{aligned}\partial_\tau(\tau RT^3 \gamma_\perp) + \partial_R(\tau RT^3 \gamma_\perp v^R) &= 0, \\ \partial_y T &= 0, \\ \partial_\tau(T \gamma_\perp v^R) + \partial_R(T \gamma_\perp) &= 0, \\ \partial_\varphi T &= 0.\end{aligned}\tag{4.27}$$

These equations have the solution (Gubser, 2010; Gubser and Yarom, 2011)

$$\begin{aligned}v^R &= \frac{2q^2 \tau R}{1 + q^2(\tau^2 + R^2)}, \\ T &= \frac{T^0}{\tau^{1/3}} \frac{(2q)^{2/3}}{[1 + q^2(\tau^2 + R^2) + q^4(\tau^2 - R^2)^2]^{1/3}},\end{aligned}\tag{4.28}$$

with a free parameter  $q \geq 0$ . This analytical solution has been used by Kind (2013) to test our numerical routine for solving the hydrodynamical equations of motion.

### 4.3 The numerical approach

For the numerical evaluation of eq. (4.2) a conservative form of the equations of motion is most suitable. We follow Hujerit et al. (2008) and choose the three spatial components of eq. (4.12) as momentum equations and the first line of eqs. (4.13) as energy equation. With the metric (4.21) and four-velocity (4.24), choosing cartesian coordinates in the transverse plane, we obtain the following equations of motion:

$$\begin{aligned}\partial_\mu(\tau T^4 u^\mu u_a) &= -\frac{\tau}{4} \partial_a T^4, \\ \partial_\mu(\tau T^3 u^\mu) &= 0,\end{aligned}\tag{4.29}$$

where  $a = 1, 2, 3$ . Excluding the trivial  $y$ -component,  $\partial_y T = 0$ , we define the entropy density-, pressure and momentum density-related quantities

$$\mathcal{S} = \tau T^3 \gamma_\perp, \quad \mathcal{P} = \frac{\tau}{4} T^4, \quad \mathcal{M}_a = \tau T^4 \gamma_\perp u_a,\tag{4.30}$$

and their corresponding currents,

$$\mathcal{J}_S^a = \mathcal{S} v^a, \quad \mathcal{J}_{\mathcal{M}^a_b} = \mathcal{M}_b v^a,\tag{4.31}$$

where  $a, b = 1, 2$ . Thus we finally arrive at the following system of equations

$$\begin{aligned}\partial_\tau \mathcal{S} + \partial_1 \mathcal{J}_S^1 + \partial_2 \mathcal{J}_S^2 &= 0, \\ \partial_\tau \mathcal{M}_1 + \partial_1 (\mathcal{J}_M^1 + \mathcal{P}) + \partial_2 \mathcal{J}_M^2 &= 0, \\ \partial_\tau \mathcal{M}_2 + \partial_1 \mathcal{J}_M^1 + \partial_2 (\mathcal{J}_M^2 + \mathcal{P}) &= 0.\end{aligned}\tag{4.32}$$

These three equations are well suited for a numerical treatment. They describe the evolution of  $\mathcal{S}$  and  $\mathcal{M}_a$  in the LCF time  $\tau$ . Temperature  $T$  and transverse velocity  $v^a$  are connected to these quantities via

$$\begin{aligned}v^a &= \frac{\mathcal{M}_a}{\mathcal{M}_\perp} \frac{\mathcal{K}}{3} \left[ -1 + 2 \cosh \left( \frac{1}{3} \operatorname{arcosh} \left( \frac{27}{2\mathcal{K}^2} - 1 \right) \right) \right], \\ T &= \left( \frac{\mathcal{S}}{\tau \gamma_\perp} \right)^{1/3},\end{aligned}\tag{4.33}$$

where  $\mathcal{K} = \tau \mathcal{M}_\perp^3 / \mathcal{S}^4$  and  $\mathcal{M}_\perp = \sqrt{\mathcal{M}_1^2 + \mathcal{M}_2^2}$ .

For the numerical evaluation of eqs. (4.32) we define a  $N \times N$  grid of two-dimensional cells, depicted in fig. 4.2, where densities  $\mathcal{S}$ ,  $\mathcal{P}$  and  $\mathcal{M}_b$  are evaluated at the cell centers and currents  $\mathcal{J}_S^a$  and  $\mathcal{J}_M^a$  at the cell faces. The cell grid is thus divided into three sub-grids: One sub-grid comprises  $N \times N$  points located at the cell centers where the densities are defined, then there is a staggered  $(N + 1) \times N$  grid for currents in the  $x^1$ -direction and a staggered  $N \times (N + 1)$  grid for currents in the  $x^2$ -direction.

We use indices  $n, j, k$  to identify time and grid points according to

$$\tau_n = \epsilon_n + \tau_{n-1}, \quad x_j^1 = jd, \quad x_k^2 = kd,\tag{4.34}$$

with a constant grid spacing  $d$  and variable time steps  $\epsilon_n$ . Typical dimensions of  $d$  and the grid size  $N$  are

$$d = 0.1 - 0.4 \text{ fm}, \quad N = 25 - 100.\tag{4.35}$$

The relative location of a grid point  $(j, k)$  for the cell centers and faces is shown in fig. 4.2. In the following we use the abbreviated notation

$$\begin{aligned}\mathcal{S}_{j,k}^n &= \mathcal{S}(\tau_n, x_j^1, x_k^2) = \mathcal{S}(\tau_n, jd, kd), \\ (\mathcal{J}_S^1)_{j,k}^n &= \mathcal{J}_S^1(\tau_n, (x_j^1 + x_{j-1}^1)/2, x_k^2) = \mathcal{J}_S^1(\tau_n, (j - 1/2)d, kd), \\ (\mathcal{J}_S^2)_{j,k}^n &= \mathcal{J}_S^2(\tau_n, x_j^1, (x_k^2 + x_{k-1}^2)/2) = \mathcal{J}_S^2(\tau_n, jd, (k - 1/2)d),\end{aligned}\tag{4.36}$$

and analogous for the other quantities. Note that for  $(\mathcal{J}_M^a)_{j,k}^n$  only the index  $a$  determines on which cell faces it is defined according to eq. (4.36), but not the index  $b$ .

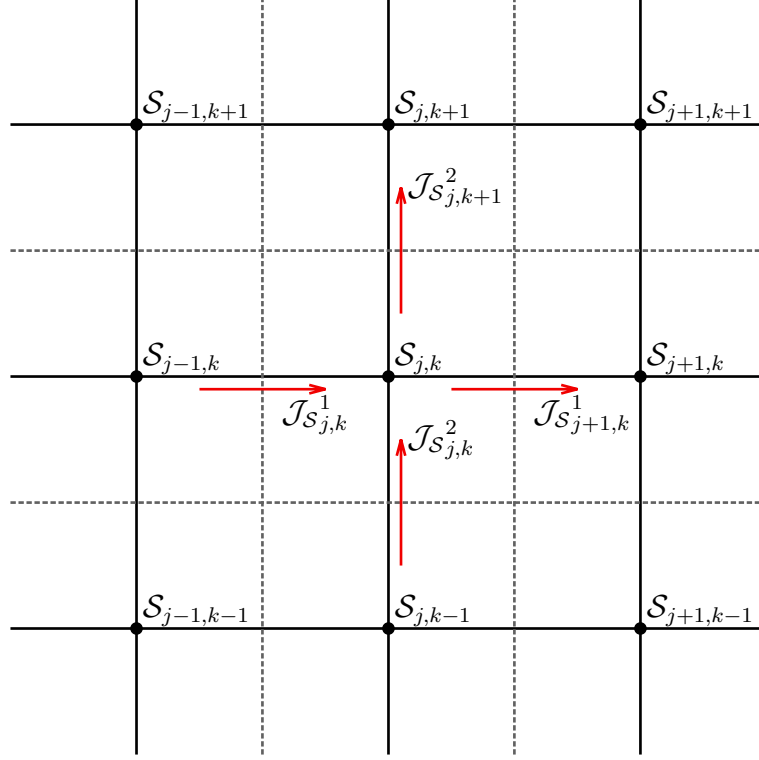


Figure 4.2: Staggered grid discretization used in the hydrodynamical calculation. Densities  $\mathcal{S}$ ,  $\mathcal{P}$  and  $\mathcal{M}_b$  are defined at the cell centers (black dots) and the corresponding currents  $\mathcal{J}_{\mathcal{S}^a}$  and  $\mathcal{J}_{\mathcal{M}^a b}$ ,  $a, b = 1, 2$ , on the cell faces (dashed gray lines).

The discretized version of eqs. (4.32) thus reads

$$\begin{aligned}
 \mathcal{S}_{j,k}^{n+1} &= -\frac{\epsilon_n}{d} [(\mathcal{J}_{\mathcal{S}^1})_{j+1,k}^n - (\mathcal{J}_{\mathcal{S}^1})_{j,k}^n + (\mathcal{J}_{\mathcal{S}^2})_{j,k+1}^n - (\mathcal{J}_{\mathcal{S}^2})_{j,k}^n], \\
 \mathcal{M}_{1,j,k}^{n+1} &= -\frac{\epsilon_n}{d} [(\mathcal{J}_{\mathcal{M}^1 1})_{j+1,k}^n - (\mathcal{J}_{\mathcal{M}^1 1})_{j,k}^n + (\mathcal{J}_{\mathcal{M}^2 1})_{j,k+1}^n - (\mathcal{J}_{\mathcal{M}^2 1})_{j,k}^n \\
 &\quad + (d\mathcal{P}_1)_{j,k}^n], \\
 \mathcal{M}_{2,j,k}^{n+1} &= -\frac{\epsilon_n}{d} [(\mathcal{J}_{\mathcal{M}^1 2})_{j+1,k}^n - (\mathcal{J}_{\mathcal{M}^1 2})_{j,k}^n + (\mathcal{J}_{\mathcal{M}^2 2})_{j,k+1}^n - (\mathcal{J}_{\mathcal{M}^2 2})_{j,k}^n \\
 &\quad + (d\mathcal{P}_2)_{j,k}^n], \tag{4.37}
 \end{aligned}$$

where the discretized pressure gradient  $d\mathcal{P}_a$  reads

$$\begin{aligned}
 (d\mathcal{P}_1)_{j,k}^n &= \frac{1}{2} (\mathcal{P}_{j+1,k}^n - \mathcal{P}_{j-1,k}^n), \\
 (d\mathcal{P}_2)_{j,k}^n &= \frac{1}{2} (\mathcal{P}_{j,k+1}^n - \mathcal{P}_{j,k-1}^n). \tag{4.38}
 \end{aligned}$$

Note that we have used a centered differencing scheme in eqs. (4.37) as well

as eq. (4.38), since the currents are defined on the cell faces and the pressure at the cell centers.

To solve eqs. (4.37) we need to impose initial conditions on temperature  $T$  and transverse velocity  $v^a$ , both defined at the cell centers. Since the initial transverse velocity is set to vanish, we only need to calculate the initial temperature profile from the fireball model. We explain the numerical procedure first, however, and postpone the closer specification of the initial conditions to section 4.4.

With given profiles of  $T$  and  $v^a$  at time  $\tau_n$  we readily calculate  $\mathcal{S}$ ,  $d\mathcal{P}_a$  and  $\mathcal{M}_a$  from eqs. (4.30) and (4.38). Further we define two velocity fields  $v_C^a \equiv v^a$  and  $v_F^a$  defined at the cell centers and faces, respectively,

$$\begin{aligned} (v_C^1)^n_{j,k} &= v_C^1(\tau_n, x_j^1, x_k^2), \\ (v_C^2)^n_{j,k} &= v_C^2(\tau_n, x_j^1, x_k^2), \\ (v_F^1)^n_{j,k} &= v_F^1(\tau_n, (x_j^1 + x_{j-1}^1)/2, x_k^2) := \frac{1}{2} \left( (v_C^1)^n_{j,k} + (v_C^1)^n_{j-1,k} \right), \\ (v_F^2)^n_{j,k} &= v_F^2(\tau_n, x_j^1, (x_k^2 + x_{k-1}^2)/2) := \frac{1}{2} \left( (v_C^2)^n_{j,k} + (v_C^2)^n_{j,k-1} \right). \end{aligned} \quad (4.39)$$

The new time step  $\epsilon_n$  is then calculated in the following way:

$$\epsilon_n = \text{CFL} \frac{d}{\max \left( |v_C|, \sqrt{|d\mathcal{P}/T^4|} \right) \Big|_{\tau=\tau_n}}, \quad \text{CFL} = \frac{1}{4}, \quad (4.40)$$

where CFL, the Courant number, ensures that the Courant-Friedrichs-Lewy condition is satisfied (Courant et al., 1928). Hence the next time step  $\epsilon_n$  is always chosen small enough so that the right-hand sides of eqs. (4.37) are very unlikely to exceed  $2\text{CFL} = 1/2$ . Subsequently the currents are calculated in an upwind-scheme,

$$\begin{aligned} (\mathcal{J}^{\mathcal{S}^1})^n_{j,k} &= \begin{cases} \mathcal{S}^n_{j-1,k} (v_F^1)^n_{j,k} & \text{for } (v_F^1)^n_{j,k} > 0 \\ \mathcal{S}^n_{j,k} (v_F^1)^n_{j,k} & \text{for } (v_F^1)^n_{j,k} \leq 0 \end{cases}, \\ (\mathcal{J}^{\mathcal{S}^2})^n_{j,k} &= \begin{cases} \mathcal{S}^n_{j,k-1} (v_F^2)^n_{j,k} & \text{for } (v_F^2)^n_{j,k} > 0 \\ \mathcal{S}^n_{j,k} (v_F^2)^n_{j,k} & \text{for } (v_F^2)^n_{j,k} \leq 0 \end{cases}, \end{aligned} \quad (4.41)$$

and analogous for  $\mathcal{J}^{\mathcal{M}^a}$ . Eqs. (4.37) may then be evaluated for  $\mathcal{S}$  and  $\mathcal{M}_a$  at time  $\tau_{n+1}$  so  $T$  and  $v_C^a$  can be updated from eqs. (4.33).

Due to the symmetry of the system we infer that all physical quantities under consideration are either symmetric or antisymmetric under the reflections  $x^1 \leftrightarrow -x^1$  and  $x^2 \leftrightarrow -x^2$ . The quantities  $\mathcal{S}$ ,  $T$  and  $\mathcal{P}$ , for example, are symmetric under both reflections. The velocity component  $v_C^1$ , on the other

Table 4.1: Behavior of relevant thermodynamical quantities under the two reflections  $x^1 \leftrightarrow -x^1$  and  $x^2 \leftrightarrow -x^2$ .

Quantity	$x^1 \leftrightarrow -x^1$	$x^2 \leftrightarrow -x^2$
$\mathcal{S}, \mathcal{P}, T$	symmetric	symmetric
$\mathcal{J}_S^1, v_C^1, v_F^1, d\mathcal{P}_1, \mathcal{M}_1$	antisymmetric	symmetric
$\mathcal{J}_S^2, v_C^2, v_F^2, d\mathcal{P}_2, \mathcal{M}_2$	symmetric	antisymmetric
$\mathcal{J}_M^1, \mathcal{J}_M^2$	symmetric	symmetric
$\mathcal{J}_M^1, \mathcal{J}_M^2$	antisymmetric	antisymmetric

hand, is antisymmetric under  $x^1 \leftrightarrow -x^1$  but symmetric under  $x^2 \leftrightarrow -x^2$  and vice versa for  $v_C^2$ . Tab. 4.1 lists the behavior of all relevant thermodynamical quantities under these reflections. It is hence possible to solve eqs. (4.37) for positive  $x^1, x^2$  only. The following boundary conditions are then imposed on  $\mathcal{J}_S^a$  and  $\mathcal{J}_M^a$  at the inner boundary:

$$\begin{aligned}
(\mathcal{J}_S^1)^{n+1}_{0,k} &= -(\mathcal{J}_S^1)^n_{1,k}, & (\mathcal{J}_S^2)^{n+1}_{j,0} &= -(\mathcal{J}_S^2)^n_{j,1}, \\
(\mathcal{J}_M^1)^{n+1}_{0,k} &= +(\mathcal{J}_M^1)^n_{1,k}, & (\mathcal{J}_M^2)^{n+1}_{j,0} &= -(\mathcal{J}_M^2)^n_{j,1}, \\
(\mathcal{J}_M^1)^{n+1}_{0,k} &= -(\mathcal{J}_M^1)^n_{1,k}, & (\mathcal{J}_M^2)^{n+1}_{j,0} &= +(\mathcal{J}_M^2)^n_{j,1},
\end{aligned} \tag{4.42}$$

while at the outer boundary we set

$$\begin{aligned}
(\mathcal{J}_S^1)^{n+1}_{N,k} &= \begin{cases} \mathcal{S}^{n_{N-1,k}}(v_F^1)^n_{N,k} & \text{for } (v_F^1)^n_{N,k} > 0 \\ 0 & \text{for } (v_F^1)^n_{N,k} \leq 0 \end{cases}, \\
(\mathcal{J}_S^2)^{n+1}_{j,N} &= \begin{cases} \mathcal{S}^{n_{j,N-1}}(v_F^2)^n_{j,N} & \text{for } (v_F^2)^n_{j,N} > 0 \\ 0 & \text{for } (v_F^2)^n_{j,N} \leq 0 \end{cases}, \\
(\mathcal{J}_M^1)^{n+1}_{N,k} &= \begin{cases} \mathcal{M}_1^{n_{N-1,k}}(v_F^1)^n_{N,k} & \text{for } (v_F^1)^n_{N,k} > 0 \\ 0 & \text{for } (v_F^1)^n_{N,k} \leq 0 \end{cases}, \\
(\mathcal{J}_M^2)^{n+1}_{j,N} &= \begin{cases} \mathcal{M}_1^{n_{j,N-1}}(v_F^2)^n_{j,N} & \text{for } (v_F^2)^n_{j,N} > 0 \\ 0 & \text{for } (v_F^2)^n_{j,N} \leq 0 \end{cases}, \\
(\mathcal{J}_M^1)^{n+1}_{N,k} &= \begin{cases} \mathcal{M}_2^{n_{N-1,k}}(v_F^1)^n_{N,k} & \text{for } (v_F^1)^n_{N,k} > 0 \\ 0 & \text{for } (v_F^1)^n_{N,k} \leq 0 \end{cases}, \\
(\mathcal{J}_M^2)^{n+1}_{j,N} &= \begin{cases} \mathcal{M}_2^{n_{j,N-1}}(v_F^2)^n_{j,N} & \text{for } (v_F^2)^n_{j,N} > 0 \\ 0 & \text{for } (v_F^2)^n_{j,N} \leq 0 \end{cases}.
\end{aligned} \tag{4.43}$$

The conditions at the inner boundary implement the reflection (anti-) symmetry while the conditions at the outer boundary simply state that energy, momenta etc. may be carried out of the domain of calculation.

## 4.4 The initial conditions

As explained in section 4.3 we need to impose initial conditions on  $T$  and  $v^a$  at some initial LCF-time  $\tau_{\text{init}}$  in order to solve eqs. (4.37). The transverse velocity is simply set to vanish initially,  $v^a(\tau_{\text{init}}) = 0$ , so we only have to consider the initial temperature profile.

We model the number density of a lead nucleus in its rest frame by a two parameter Woods-Saxon potential,

$$n_{\text{Pb}}(\vec{x}) = \frac{n_0}{1 + e^{(|\vec{x}| - R_{\text{Pb}})/a}}, \quad \int d^3x n_{\text{Pb}}(\vec{x}) = A, \quad (4.44)$$

where  $R_{\text{Pb}} = 6.62$  fm,  $a = 0.546$  fm (de Vries et al., 1987) and  $n_0$  normalizes  $n_{\text{Pb}}$  to the nucleon number of lead,  $A = 208$ . Using the number density  $n_{\text{Pb}}$  we can define the nuclear thickness and overlap  $T_A^\pm$  and  $T_{AA}$ , respectively, as

$$\begin{aligned} T_A^\pm(b, x^1, x^2) &= \int dx^3 n_{\text{Pb}}(x^1 \pm b/2, x^2, x^3), \\ T_{AA}(b, x^1, x^2) &= T_A^+(b, x^1, x^2) T_A^-(b, x^1, x^2). \end{aligned} \quad (4.45)$$

The nuclear overlap is an important quantity in the fireball model since it is proportional to the number of collisions  $N_{\text{coll}}$  and thus proportional to the number of  $b\bar{b}$  pairs  $N_{b\bar{b}}$  produced at a given point  $(x^1, x^2)$  in the transverse plain,

$$N_{b\bar{b}}(b, x^1, x^2) \propto N_{\text{coll}}(b, x^1, x^2) \propto T_{AA}(b, x^1, x^2).$$

The number of inelastic binary collisions  $N_{\text{coll}}$  and the number of participants  $N_{\text{part}}$ , nucleons which underwent at least one inelastic collision, are given by

$$\begin{aligned} N_{\text{coll}}(b) &= \sigma_{\text{inel},pp} \int d^2x T_{AA}(b, x^1, x^2), \\ N_{\text{part}}(b) &= \int d^2x \frac{T_A^+(b, x^1, x^2)}{A} \left( 1 - \left( 1 - \sigma_{\text{inel},pp} \frac{T_A^-(b, x^1, x^2)}{A} \right)^A \right) \\ &\quad + \int d^2x \frac{T_A^-(b, x^1, x^2)}{A} \left( 1 - \left( 1 - \sigma_{\text{inel},pp} \frac{T_A^+(b, x^1, x^2)}{A} \right)^A \right), \end{aligned} \quad (4.46)$$

respectively. The cross section for inelastic  $pp$ -collisions at  $\sqrt{s} = 2.76$  TeV amounts to  $\sigma_{\text{inel},pp} = 64$  mb (Nakamura et al., 2010). Since all these quantities depend neither on  $x^0$  nor  $x^3$  they may simply be transferred to the LCF, where the numerical calculation is conducted.

Table 4.2: Centrality bins  $c$  with their lower boundaries  $b_c$  and corresponding bin-averaged number of collisions  $\langle N_{\text{coll}} \rangle_c$  and participants  $\langle N_{\text{part}} \rangle_c$ , respectively.

Centrality bin	$b_c$ (fm)	$\langle N_{\text{coll}} \rangle_c$	$\langle N_{\text{part}} \rangle_c$
0 - 5 %	0	1740	379.5
5 - 10 %	3.4	1384	326.2
10 - 20 %	4.9	990.3	257.9
20 - 30 %	7.0	610.3	183.8
30 - 40 %	8.6	349.2	124.8
40 - 50 %	9.9	183.0	80.0
50 - 100 %	11.1	26.8	17.5

To compare with measurements we have to average the theoretical results over centrality bins. A quantity is averaged over the centrality bin  $c$  by integrating over the impact parameter in the interval  $b_c \leq b < b_{c+1}$ , weighted with  $d\sigma_{\text{inel},AA}/db$ , where  $\sigma_{\text{inel},AA}$  is the cross section for an inelastic nucleon-nucleon collision to occur in a heavy ion collision,

$$\langle f \rangle_c = \frac{\int_{b_c}^{b_{c+1}} db \frac{d\sigma_{\text{inel},AA}}{db}(b) f(b)}{\int_{b_c}^{b_{c+1}} db \frac{d\sigma_{\text{inel},AA}}{db}(b)}, \quad (4.47)$$

where  $d\sigma_{\text{inel},AA}/db$  and  $\sigma_{\text{inel},AA}$  are calculated as follows:

$$\begin{aligned} \frac{d\sigma_{\text{inel},AA}}{db}(b) &= 2\pi b (1 - e^{-N_{\text{coll}}(b)}), \\ \sigma_{\text{inel},AA}(b) &= \int_0^b db' \frac{d\sigma_{\text{inel},AA}}{db'}. \end{aligned} \quad (4.48)$$

A centrality bin  $c$  is then determined by a lower bound  $b_c$  such that the fraction

$$\frac{\sigma_{\text{inel},AA}(b_c)}{\sigma_{\text{inel},AA}(\infty)} \quad (4.49)$$

takes a certain value. Here we use the same seven centrality bins as in the CMS experiment, so that the above fraction amounts to 0, 0.05, 0.1, 0.2, 0.3, 0.4 and 0.5. The corresponding lower boundaries on the impact parameter  $b_c$  as well as averages of  $N_{\text{coll}}$  and  $N_{\text{part}}$  according to eq. (4.47) are listed in tab. 4.2.

Since the transverse temperature profile in the fireball produced in relativistic heavy ion collisions is quite uncertain, we will consider two scenarios with different initial conditions, IC1 and IC2, respectively. In the first

scenario we consider the temperature distribution to scale with the energy liberated in binary collisions and in the second we consider a similar scaling for the entropy instead. Since  $s \propto T^3$  this yields in the LCF

$$T(b, \tau_{\text{init}}, x^1, x^2) = T_0 \frac{N_{\text{coll}}(b, x^1, x^2)}{N_{\text{coll}}(0, 0, 0)}, \quad (\text{IC1})$$

$$T(b, \tau_{\text{init}}, x^1, x^2) = T_0 \left( \frac{N_{\text{mix}}(b, x^1, x^2)}{N_{\text{mix}}(0, 0, 0)} \right)^{1/3}, \quad (\text{IC2}) \quad (4.50)$$

respectively. Here we have introduced  $N_{\text{mix}}$ , which combines the number of binary collisions  $N_{\text{coll}}$  and participants  $N_{\text{part}}$ ,

$$N_{\text{mix}}(b, x^1, x^2) = \frac{1-f}{2} N_{\text{part}}(b, x^1, x^2) + f N_{\text{coll}}(b, x^1, x^2), \quad (4.51)$$

where  $f = 0.145$  as determined from fits of the charged particle multiplicity (Back et al., 2004; Aamodt et al., 2011b). For a pure Bjorken-flow one can insert eqs. (4.50) into eq. (4.26) to obtain the LCF-temperature in absence of transverse expansion,

$$T_{\text{long}}(b, \tau, x^1, x^2) = T_c \frac{N_{\text{coll}}(b, x^1, x^2)}{N_{\text{coll}}(0, 0, 0)} \left( \frac{\tau_{\text{QGP}}}{\tau} \right)^{1/3}, \quad (\text{IC1})$$

$$T_{\text{long}}(b, \tau, x^1, x^2) = T_c \left( \frac{N_{\text{mix}}(b, x^1, x^2)}{N_{\text{mix}}(0, 0, 0)} \right)^{1/3} \left( \frac{\tau_{\text{QGP}}}{\tau} \right)^{1/3}, \quad (\text{IC2}) \quad (4.52)$$

where  $T_c = 170$  MeV as usual and  $\tau_{\text{QGP}}$  is the maximum lifetime of the QGP as measured in the LCF, i.e. the lifetime along the beam axis for a central collision.

For the numerical solution of eqs. (4.37) we choose an initial time  $\tau_{\text{init}}$  in the LCF, typically of the order 0.1 fm/c, and then use one the eqs. (4.50) as initial condition for  $T$ . Typical values of the initial core temperature in central collisions are:  $T_0 = 550 - 650$  MeV.

Representative solutions for  $T$  and  $v^a$  are plotted in figs. 4.3 and 4.4, respectively, both for a central collision ( $b = 0$ ) and a peripheral collision ( $b = 8$  fm) using IC1 and IC2 from eqs. (4.50) with  $\tau_{\text{init}} = 0.1$  fm/c and  $T_0 = 650$  MeV. For a purely longitudinal flow we would have to set  $\tau_{\text{QGP}} = 5.6$  fm/c to obtain  $T_{\text{long}}(0, \tau_{\text{init}}, 0, 0) = T_0$ . The QGP-lifetime is of course always smaller for a fireball expanding in the transverse and longitudinal direction than for purely longitudinal expansion. Larger QGP-lifetimes can be obtained by either increases  $\tau_{\text{init}}$  or  $T_0$ .

Fig. 4.3 depicts temperature profiles for a pure Bjorken-flow as given in eq. (4.26) and for the numerical solution of eqs. (4.37). Evidently the

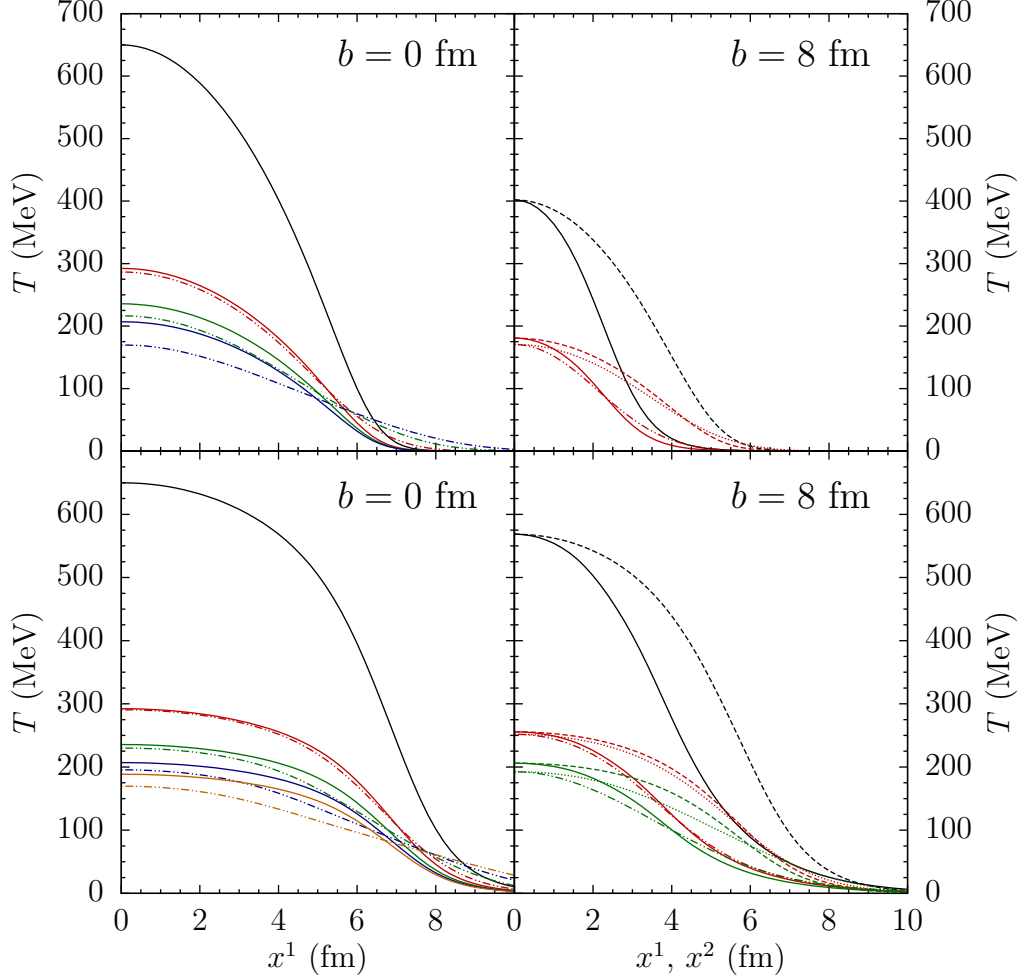


Figure 4.3: Profiles of the temperature  $T$  in the fireball for a central collision ( $b = 0$ , left) and a peripheral collision ( $b = 8$  fm, right) for times  $\tau = 0.1$  (black), 1.1 (red), 2.1 (green), 3.1 fm/c (blue) and 4.1 fm/c (orange), respectively. Left plots:  $T$  is plotted along the  $x^1$ -axis for a pure Bjorken-flow (4.26) in solid lines together with the numerical solution of eqs. (4.37) in dash-dot-dotted lines using IC1 (top) and IC2 (bottom). Right plots:  $T$  is plotted for a pure Bjorken-flow along the  $x^1$ - and  $x^2$ -axis in solid and dashed lines, respectively, as well as in dash-dot-dotted and dotted lines for the corresponding numerical solution, using IC1 (top) and IC2 (bottom). See text for more information.

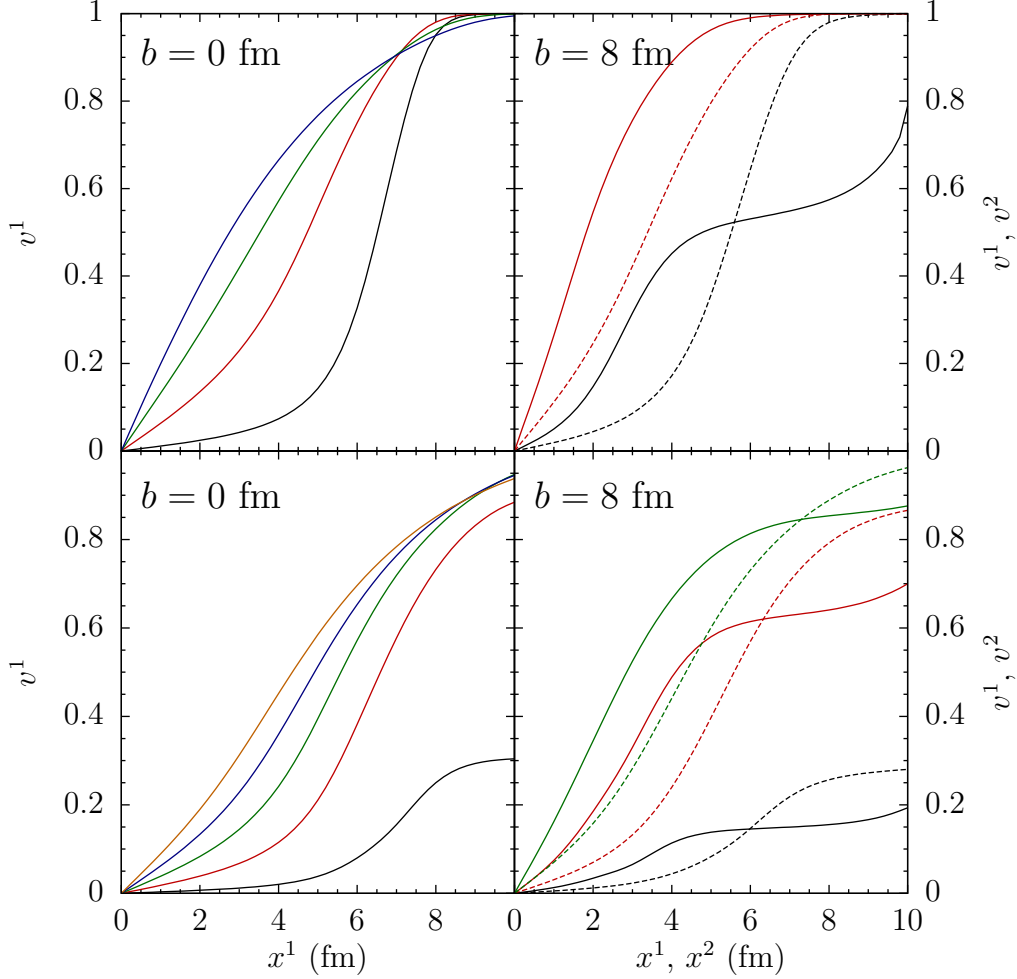


Figure 4.4: Profiles of the transverse velocity  $v_C^a \equiv v^a$ ,  $a = 1, 2$ , in the fireball from eqs. and (4.33) and (4.37) for a central collision ( $b = 0$ , left) and a peripheral collision ( $b = 8$  fm, right) for times  $\tau = 0.3$  (black), 1.1 (red), 2.1 (green), 3.1 fm/c (blue) and 4.1 fm/c (orange), respectively. Left plots:  $v^1$  is plotted along the  $x^1$ -axis using IC1 (top) and IC2 (bottom). Right plots:  $v^1$  and  $v^2$  are plotted along the  $x^1$ - and  $x^2$ -axis in solid and dash-dot-dotted lines, respectively, using IC1 (top) and IC2 (bottom). See text for more information.

transverse expansion of the fireball speeds up the cooling of the QGP due to the additional increase in volume. Using IC1 yields shorter QGP-lifetimes than IC2 since the latter results in a much broader temperature distribution. A comparison between the temperature profiles along the  $x^1$ - and  $x^2$ -axis is also drawn for the peripheral collision, where the system has no cylindrical symmetry about the  $x^3$ -axis. Clearly the contribution of transverse expansion is larger for more central collisions due to the longer QGP-lifetime.

The transverse velocity components are depicted in fig. 4.4. Apparently the velocity grows very quickly in the more peripheral regions of the collision and approaches the speed of light very closely. This is due to the rapidly decreasing energy density at large distance from the collision center, which makes the applicability of hydrodynamics doubtful in this region. This effect becomes visible especially at early times at the outer boundaries. It does not represent a problem for the numerical approach, however, since these remote regions do not contribute significantly to the final results (see chapter 5) and the transverse velocity is always directed outwards so no information from the outer region can flow towards the center.



# Chapter 5

## $\Upsilon$ suppression in PbPb collisions at the LHC

We have obtained results for the in-medium bottomium decay width and melting temperatures in chapter 3 and time-dependent fireball temperature and velocity profiles in chapter 4. Thus we are now well prepared to calculate the suppression of  $\Upsilon$  mesons in relativistic PbPb collisions at the LHC.

In section 5.1 we calculate the amount of suppression that occurs within the QGP and present the subsequent decay cascade calculation in section 5.2. The final results that include the decay cascade, however, are presented and discussed in chapter 6.

### 5.1 Suppression in the quark-gluon plasma

Let us quantify the amount of suppression within the QGP of bottomium states  $(n - l, l)$  with transverse momentum  $p_T$ , as measured in the LF, in terms of the QGP-suppression factor  $R_{AA, nl}^{\text{QGP}}(c, p_T)$  for PbPb collisions in the centrality bin  $c$ .

Since we have defined a  $p_T$ -dependent quantity here, let us recall from chapter 4 that the same transverse momenta  $p_T$  are measured in the LF and the LCF. Hence we may perform  $p_T$ -dependent calculations in the LCF and readily transfer the results to the LF, where the experimental data have been measured.

The QGP-suppression factor is not directly measurable since it accounts only for the amount of suppression inside the fireball due to the three processes of color screening, collisional damping and gluodissociation. It is given by the ratio of the number of bottomia that have survived the fireball to the number of produced bottomia. As mentioned in chapter 4 the num-

ber of produced bottomia at a given point in the transverse plain scales with the number of binary collisions and hence with the nuclear overlap,  $N_{b\bar{b}} \propto N_{\text{coll}} \propto T_{AA}$ . Thus we write  $R_{AA}^{\text{QGP}}$  as follows:

$$R_{AA,nl}^{\text{QGP}}(c, p_T) = \frac{\int_{b_c}^{b_{c+1}} db b \int d^2x T_{AA}(b, x^1, x^2) D_{nl}(b, p_T, x^1, x^2)}{\int_{b_c}^{b_{c+1}} db b \int d^2x T_{AA}(b, x^1, x^2)}. \quad (5.1)$$

Let us first consider the denominator in eq. (5.1): We integrate the nuclear overlap  $T_{AA}$  over the transverse plain which gives a result that scales with the number of bottomia produced per transverse slice in the fireball. Since this number does not depend on  $x^3$ , or  $y$  for that matter, it also scales with the total number of bottomia produced in the fireball for this impact parameter  $b$ . The integration over  $b$  then yields a result which scales with the total number of bottomia produced in the fireball for collisions in the centrality bin  $c$ . Up to a constant factor the denominator in eq. (5.1) thus gives the bottomium yield for  $pp$ -collisions scaled with  $T_{AA}$ ; i.e. it treats PbPb collisions like many mutually independent  $pp$ -collisions.

A heavy ion collision is more than just a large number of nucleon-nucleon-collisions since a hot medium is produced which is not present in  $pp$ -collisions. Hence the same calculation is performed in the numerator in eq. (5.1), whereas now a damping factor  $D_{nl}$  has been inserted.  $D_{nl}(b, p_T, x^1, x^2)$  gives the fraction of bottomia of state  $(n-l, l)$  that have been produced at  $(x^1, x^2)$  with transverse momentum  $p_T$  in a collision with impact parameter  $b$  and have survived until the fireball has cooled. The numerator of eq. (5.1) thus scales with the total number of surviving bottomia for collisions in the centrality bin  $c$ .

The damping factor  $D_{nl}$  is given by the temporal integral over the total decay width  $\Gamma_{\text{tot},nl}$  from eq. (3.39),

$$D_{nl}(b, p_T, x^1, x^2) = \exp \left[ - \int_{\tau_{F,nl}}^{\infty} \frac{d\tau \Gamma_{\text{tot},nl}}{\gamma_{T,nl}(p_T)} \right],$$

$$\Gamma_{\text{tot},nl} = \Gamma_{\text{tot},nl}(T_{\text{eff},nl}(b, p_T, \tau, x^1, x^2)),$$

$$\gamma_{T,nl}(p_T) = \sqrt{1 + \frac{p_T^2}{M_{nl}^2}}, \quad (5.2)$$

where  $\tau_{F,nl}$  is the formation time in the bottomium rest-frame,  $\gamma_{T,nl}(p_T)$  the Lorentz-factor due to transverse motion in the LCF,  $M_{nl}$  the experimentally measured bottomium vacuum mass and  $T_{\text{eff}}$  is an effective temperature properly defined below.

The decay width depends indirectly on impact parameter, transverse momentum and spacetime coordinates through the temperature distribution. This allows us to use eq. (3.39) to obtain  $\Gamma_{\text{tot},nl}$  as a function of spacetime. The integral is performed in the LCF where the evolution of temperature is calculated, but its result is Lorentz-invariant. The decay width, however, is evaluated in the bottomium rest frame and therefore a corresponding Lorentz-factor has been included in the integrand.

We have written  $T_{\text{eff}}$  instead of  $T$  in eqs. (5.2) to capture the effect of a finite relative velocity between the bottomium states and the medium. In the following we will consider all bottomia to flow in the same direction as the medium with momentum  $p = p_T v_{\perp}/|v_{\perp}|$ , energy  $E_{nl} = (M_{nl}^2 + p_T^2)^{1/2}$  and velocity  $\beta_{nl} = p/E_{nl}$  in the LCF, where  $v_{\perp}$  is the transverse medium velocity,

$$v_{\perp} = v^1 e_1 + v^2 e_2, \quad (5.3)$$

with the same components  $v^1, v^2$  as in eq. (4.24).

Bottomium states are too inert to experience substantial change of their momenta by collisions with the light medium particles. In addition they are also color-neutral on large scales so the strong force can not mediate momentum exchange very effectively. Hence  $p$  is constant, whereas the magnitude of the medium velocity  $v_{\perp}$  is obviously changing in time. This yields a finite relative velocity

$$v_{\text{rel},nl} = \frac{v_{\perp}}{|v_{\perp}|} \frac{|v_{\perp}| - |\beta_{nl}|}{1 - |v_{\perp}| |\beta_{nl}|}. \quad (5.4)$$

If there exists a finite relative velocity  $v_{\text{rel},nl}$  between the QGP and the  $b\bar{b}$  state, the relativistic Doppler shift will result in an angle-dependent, effective temperature (Escobedo et al., 2011),

$$T'_{\text{eff}}(v, \theta) = T \frac{\sqrt{1 - v^2}}{1 - v \cos \theta}, \quad (5.5)$$

where  $v \equiv v_{\text{rel},nl}$  for clarity and  $\theta$  is the angle between  $v$  and the line of sight. The behavior of  $T'_{\text{eff}}$  as a function of  $\theta$  is depicted in fig. 5.1 for different  $v$ . In general  $T'_{\text{eff}}$  results in a blue-shifted effective temperature in the forward direction and a red-shifted one in the backward direction. The effect of red- and blue-shift gets more and more pronounced with increasing velocity  $v$  but the red-shifted region is growing, while the blue-shifted region is restricted to smaller and smaller angles  $\theta$ ; a fact that has already been pointed out by Escobedo et al. (2013).

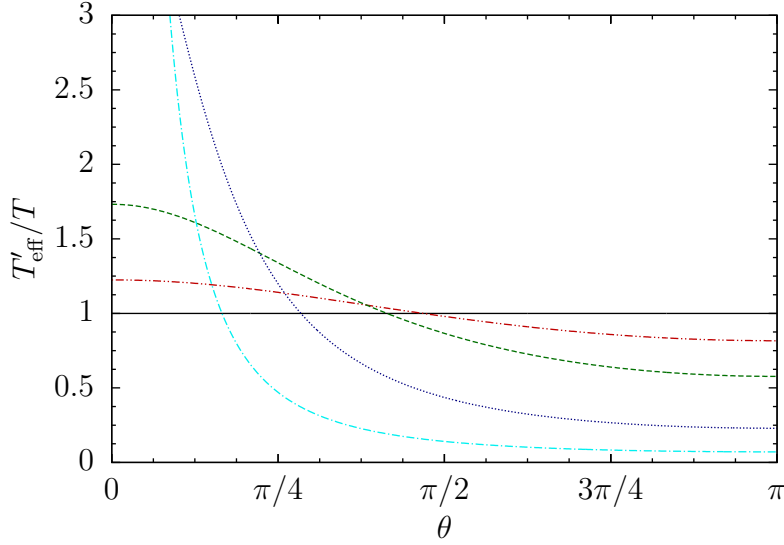


Figure 5.1: Anisotropic temperature  $T'_{\text{eff}}(v, \theta)$  for  $v = 0$  (black, solid), 0.2 (red, dash-dot-dotted), 0.5 (green, dashed), 0.9 (blue, dotted), 0.99 (cyan, dash-dotted).

In this thesis we will not use eq. (5.5), however, but limit ourselves to an approximation of the overall effect of this non-isotropic effective temperature. For this purpose we define an isotropic effective temperature  $T_{\text{eff}}(v)$  by averaging  $T'_{\text{eff}}(v, \theta)$  over the solid angle,

$$\begin{aligned} T_{\text{eff}}(v) &= \frac{1}{4\pi} \int d\Omega T'_{\text{eff}}(v, \theta) \\ &= T \sqrt{1-v^2} \frac{\text{artanh } v}{v} \leq T. \end{aligned} \quad (5.6)$$

Thus we find that the effect of red-shift dominates over blue-shift for all relative velocities  $v > 0$ . To be more specific we reveal all dependencies by writing  $T_{\text{eff}}$  including all its arguments,

$$\begin{aligned} T_{\text{eff},nl}(b, p_T, \tau, x^1, x^2) &= T(b, \tau, x^1, x^2) \sqrt{1-v^2} \frac{\text{artanh } v}{v}, \\ v \equiv v_{\text{rel},nl}(b, p_T, \tau, x^1, x^2) &= \frac{v_{\perp} |v_{\perp}| \sqrt{M_{nl}^2 + p_T^2} - p_T}{|v_{\perp}| \sqrt{M_{nl}^2 + p_T^2} - |v_{\perp}| p_T}, \\ v_{\perp} &= v_{\perp}(b, \tau, x^1, x^2), \end{aligned} \quad (5.7)$$

where  $T(b, \tau, x^1, x^2)$  and  $v_{\perp}(b, \tau, x^1, x^2)$  are calculated numerically from the hydrodynamical model of chapter 4.

To get a better understanding of the implications of this effective temperature we have plotted in fig. 5.2 profiles of  $T$  and  $T_{\text{eff}}$  for the  $\Upsilon(1S)$  along

the  $x^1$ -axis in a central collision ( $b = 0$ ), using IC1 of eqs. (4.50),  $T_0 = 650$  MeV,  $\tau_{\text{init}} = 0.1$  fm/ $c$  and a formation time of  $\tau_{F,10} = 0.1$  fm/ $c$ . The effective temperature is plotted for  $\Upsilon(1S)$  states moving with  $p_T = 0, 6$  and  $12$  GeV/ $c$  through the QGP, respectively. One can very nicely see how the spatially varying red-shift causes the  $\Upsilon(1S)$  to see a reduced effective temperature. Maximum red-shift is attained in the collision center, where the plasma is locally at rest in the LCF. With growing distance to the center, however,  $T_{\text{eff}}$  approaches  $T$  and zero red-shift is achieved on a surface in the peripheral regions of the collision where the QGP is locally co-moving with the bottomia. At larger distances the transverse QGP velocity exceeds the bottomium velocity so the red-shift increases again. This causes  $T_{\text{eff}}$  to achieve a maximum outside the collision center for large values of  $p_T$ . Obviously location and shape of this zero-red-shift surface vary with state,  $b$ ,  $p_T$  and  $\tau$ .

Finally, to obtain the right expression for the damping factor  $D_{nl}$  we note that a bottomium state with finite  $p_T$  will not stay at the location  $(x^1, x^2)$  where it was initially produced but instead move with the aforementioned velocity  $\beta_{nl}$ . Inserting all this into eq. (5.2) yields

$$D_{nl}(b, p_T, x^1, x^2) = \exp \left[ - \int_{\tau_{F,nl} \gamma_{T,nl}(p_T)}^{\infty} \frac{d\tau \Gamma_{\text{tot},nl}}{\gamma_{T,nl}(p_T)} \right],$$

$$\Gamma_{\text{tot},nl} = \Gamma_{\text{tot},nl}(T_{\text{eff},nl}(b, p_T, \tau, x^1 + \beta_{nl}^1 \tau, x^2 + \beta_{nl}^2 \tau)). \quad (5.8)$$

Fig. 5.3 depicts profiles of the  $\Upsilon(1S)$ -damping factor  $D_{10}$  and the weighted damping factor  $T_{AA}D_{10}$  that appears in the integrand of the numerator in eq. (5.1). The two quantities are plotted for transverse momentum  $p_T = 0$  and  $6$  GeV/ $c$ , respectively, along the  $x^1$ -axis for a central collision ( $b = 0$ ), while the other collision parameters are the same as before. In general bottomia dissolve very rapidly near the collision center, where the decay width is large. As the fireball cools, however, the dissociation rate decreases strongly. Time dilation causes bottomia moving with  $p_T = 6$  GeV/ $c$  to be formed at a later time where the QGP has already cooled down a bit in addition to the red-shifted effective temperature seen by the bottomia. In general the amount of suppression decreases with increasing  $p_T$ .

The weighted damping factor  $T_{AA}D_{10}$  in the numerator in eq. (5.1) directly scales with the number of surviving bottomia in the transverse plane. Hence it is very instructive to take a look at the two-dimensional plots of  $T_{AA}D_{10}$  depicted in fig. 5.4, where again IC1,  $T_0 = 650$  MeV,  $\tau_{\text{init}} = 0.1$  fm/ $c$  and  $\tau_{F,10} = 0.1$  fm/ $c$  have been used. The transverse  $T_{AA}D_{10}$ -distributions of the  $\Upsilon(1S)$  and  $\Upsilon(2S)$  are displayed for central ( $b = 0$ ) and peripheral collision ( $b = 8$  fm) for  $p_T = 0$  and  $6$  GeV/ $c$ , respectively. Most bottomia are formed

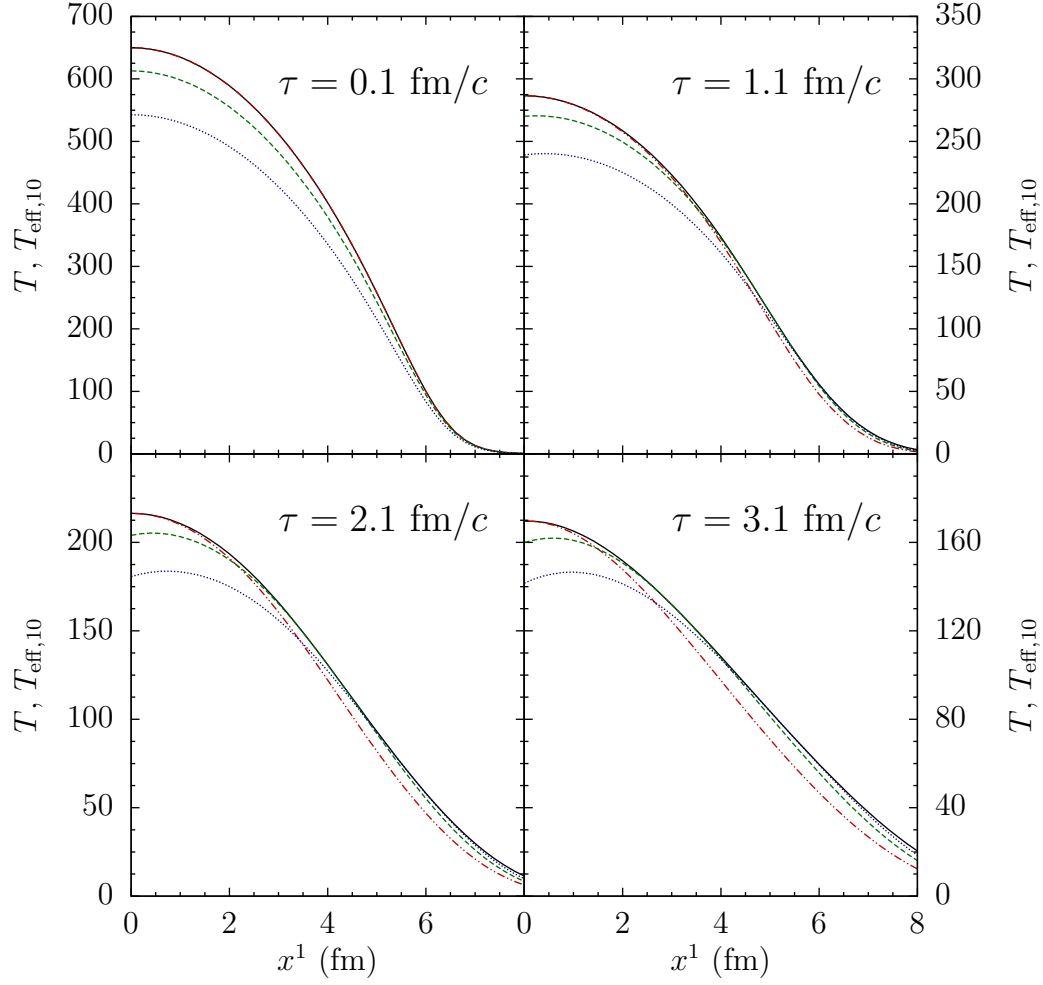


Figure 5.2: Profiles of temperature  $T$  (black lines) and  $\Upsilon(1S)$ -effective temperature  $T_{\text{eff},10}$  are plotted along the  $x^1$ -axis for a central collision ( $b = 0$ ) for transverse momenta  $p_T = 0, 6$  and  $12$  GeV/ $c$  in red, green and blue lines, respectively, at times  $\tau = 0.1$  (top left),  $1.1$  (top right),  $2.1$  (bottom left) and  $3.1$  fm/ $c$  (bottom right). See text for more information.

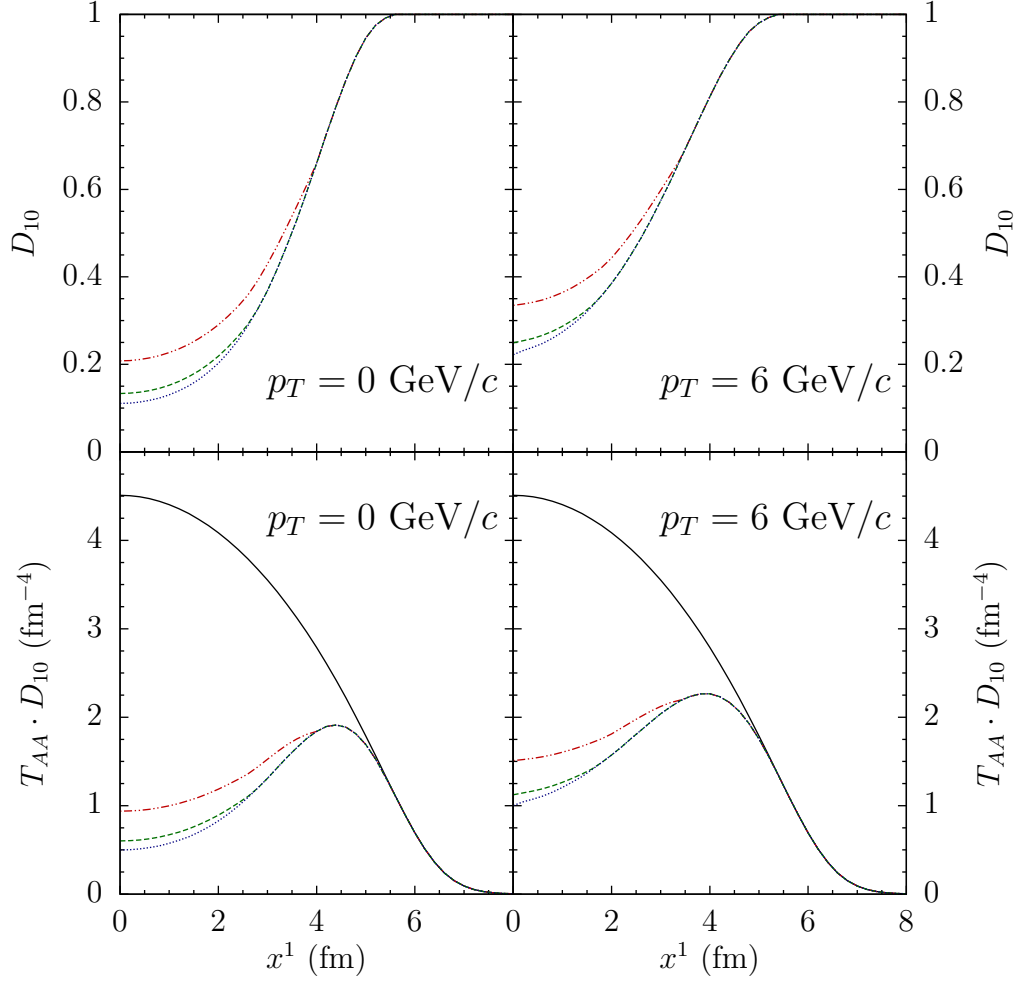


Figure 5.3: Profiles of  $\Upsilon(1S)$ -damping factor  $D_{10}$  (top) and  $T_{AA}D_{10}$  (bottom) for  $p_T = 0$  (left) and 6 GeV/c (right), respectively, plotted along the  $x^1$ -axis for a central collision ( $b = 0$ ) at times  $\tau = 0.1$  (black), 1.1 (red), 2.1 (green) and 3.1 fm/c (blue). See text for more information.

in the center of the heavy ion collision, where most binary nucleon-nucleon collisions occur. Due to the high central temperatures, however, strong suppression changes the shape of the surface from cone-like (peripheral) into volcano-like (central). Evidently, the  $\Upsilon(2S)$  is suppressed much more efficiently than the more stable  $\Upsilon(1S)$ , whereas large transverse momenta lead to significantly less suppression. Also one should note that it is the action of color screening that forbids the formation of bound  $b\bar{b}$  states above the melting temperature  $T_m$  and thus discontinuously enforces  $D_{nl} = 0$  within a certain proximity to the collision center. This does not occur for the  $\Upsilon(1S)$  in this example since its melting temperature (see tab. 3.1) is slightly higher than the maximum fireball temperature,  $T_m > T_0$ . Choosing a higher  $T_0$ , however, would lead to complete suppression of even the  $\Upsilon(1S)$  in the core of the most central collisions.

Results for the QGP-suppression factor are depicted for the  $\Upsilon(1S)$  in fig. 5.5, using IC1 and IC2 of eqs. (4.50), different choices of the initial core temperature  $T_0 = 550, 650$  MeV,  $\tau_{\text{init}} = 0.1$  fm/ $c$ , formation times  $\tau_{F,10} = 0.1, 0.5$  fm/ $c$  and transverse momenta  $p_T = 0, 6, 12$  GeV/ $c$  as well as  $p_T$ -averaged results. The  $p_T$ -average has been calculated, in the way explained below, from results for  $p_T = 0$  up to 28 GeV/ $c$  in steps of 2 GeV/ $c$ . We have plotted  $R_{AA,10}^{\text{QGP}}$  not as continuous function of centrality but instead averaged over centrality bins (see tab. 4.2) to achieve a better comparability with CMS data. The plots confirm the intuitive expectation that higher temperatures and shorter formation times increase the amount of suppression. On the other hand, the amount of suppression decreases with increasing  $p_T$  due to the stronger red-shift of the effective temperature and the dilated formation times. Also there is much less suppression for IC1 since the temperature decreases much faster with growing distance from the center than for the much broader distribution of IC2 (see fig. 4.3).

Using the bottomium production cross section  $\sigma_{nl}(p_T)$  as measured by CMS (Khachatryan et al., 2011), the average over transverse momenta is performed as follows:

$$\langle f \rangle_{nl} = \frac{\int_0^\infty dp_T \sigma_{nl}(p_T) f(p_T)}{\int_0^\infty dp_T \sigma_{nl}(p_T)}. \quad (5.9)$$

The CMS experiment has measurement transverse momenta in the range  $0 \leq p_T \leq 30$  GeV/ $c$  and correspondingly the production cross section is set to vanish above this threshold,  $\sigma_{nl}(p_T > 30 \text{ GeV}/c) = 0$ . The same production cross section is assumed for the  $\chi_b(nP)$  states as for the corresponding  $\Upsilon(nS)$  state.

A comparison of  $R_{AA}^{\text{QGP}}$  for the different bottomium states is depicted in fig. 5.6 using IC1 for  $T_0 = 650$  MeV,  $\tau_{\text{init}} = 0.1$  fm/ $c$  for transverse

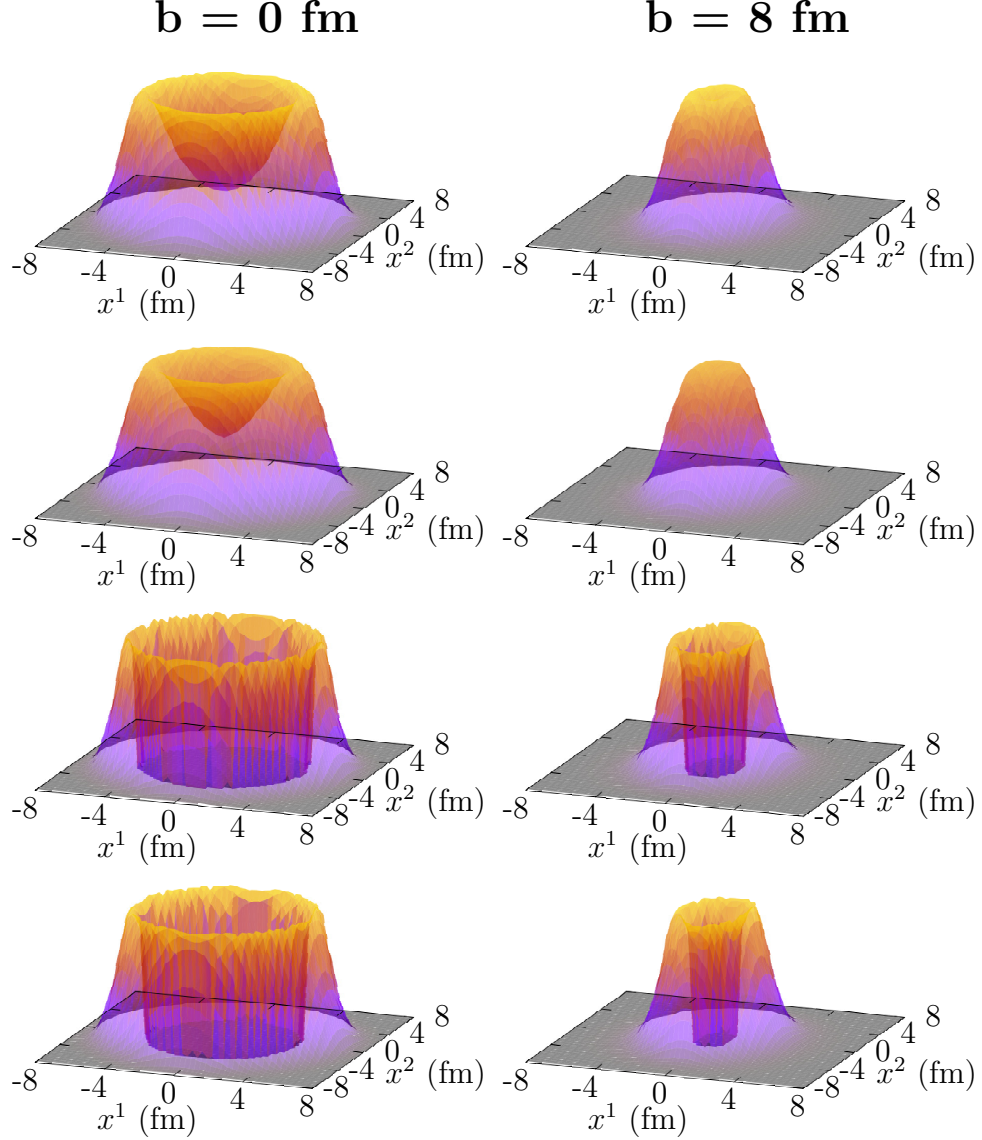


Figure 5.4: Two-dimensional profiles of  $T_{AA}D_{n0}$  for the  $\Upsilon(1S)$  and  $\Upsilon(2S)$  for central ( $b = 0$ , left-hand side) and peripheral collisions ( $b = 8$  fm, right-hand side) with  $p_T = 0$  and  $6$  GeV/ $c$ , respectively. From top to bottom we have: ( $\Upsilon(1S)$ ,  $p_T = 0$ ), ( $\Upsilon(1S)$ ,  $p_T = 6$  GeV/ $c$ ), ( $\Upsilon(2S)$ ,  $p_T = 0$ ), ( $\Upsilon(2S)$ ,  $p_T = 6$  GeV/ $c$ ). The profiles scale with the fraction of  $\Upsilon(1S)$  and  $\Upsilon(2S)$  that survive suppression throughout the lifetime of the QGP due to the three processes of color screening, collisional damping and gluodissociation. High central temperatures cause strong suppression and thus change the shape of the surface from cone-like (peripheral) into volcano-like (central). See text for more information.

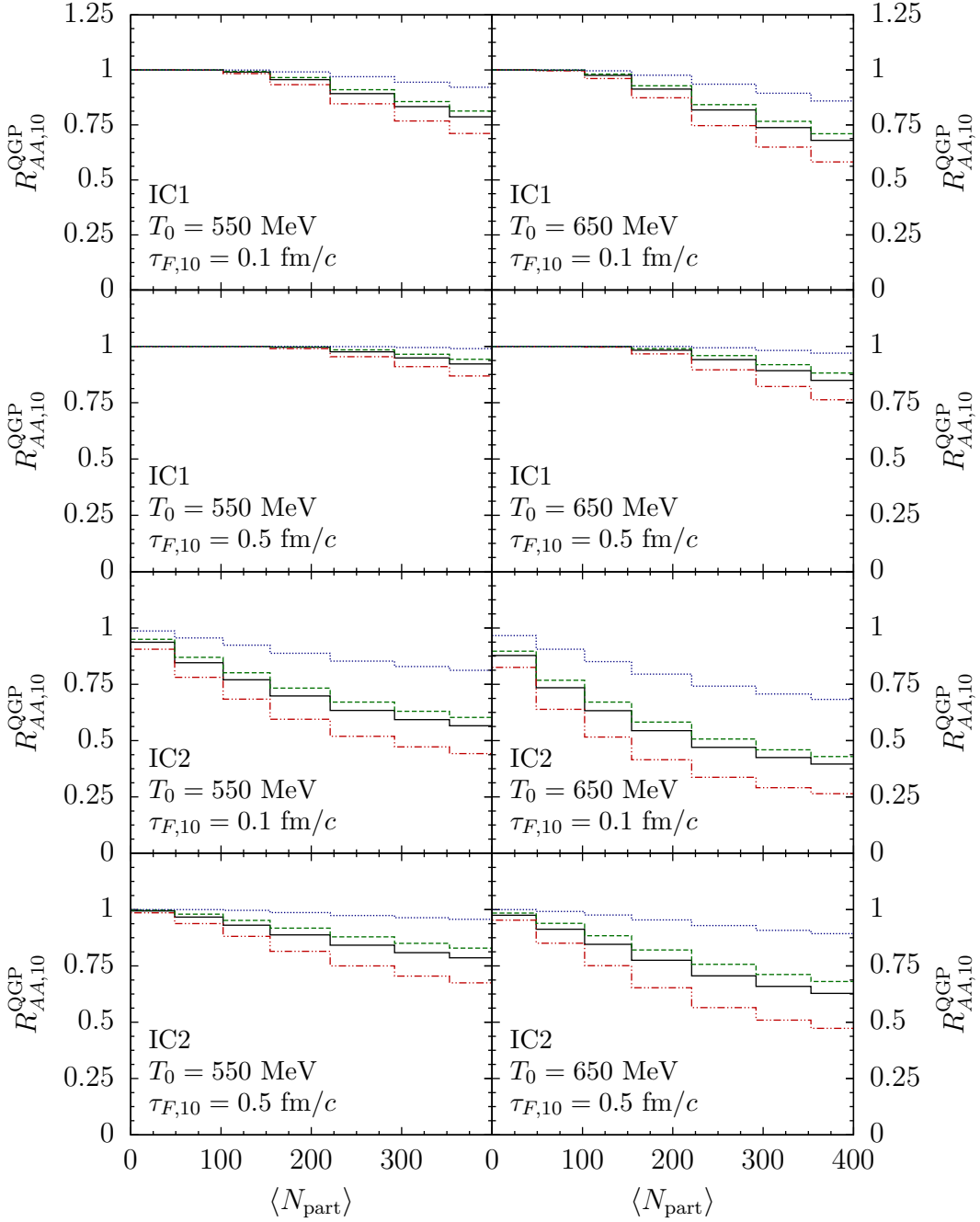


Figure 5.5: QGP-suppression factor  $R_{AA,10}^{\text{QGP}}$  for the  $\Upsilon(1S)$  using IC1 and IC2, initial core temperatures  $T_0 = 550$  and  $650$  MeV,  $\tau_{\text{init}} = 0.1$  fm/c and bottomium formation times  $\tau_F = 0.1$  and  $0.5$  fm/c, respectively, in the combinations noted in the plots. For every parameter combination the QGP-suppression  $R_{AA,10}^{\text{QGP}}$  is displayed for  $p_T = 0, 6, 12$  GeV/c (red, green and blue lines, respectively) and averaged over all  $p_T$ -values (black lines). In general the  $p_T$ -averaged results are close to the result for  $p_T = 6$  GeV/c  $\approx \langle p_T \rangle$ .

momenta  $p_T = 0, 6, 12$  GeV/ $c$  and  $p_T$ -averaged, using the same formation time of  $\tau_{F,nl} = 0.1$  fm/ $c$  for all states. Again, the  $p_T$ -average has been calculated from results for  $p_T = 0$  up to 28 GeV/ $c$  in steps of 2 GeV/ $c$ . The ground state  $\Upsilon(1S)$  is significantly less suppressed in the QGP than the excited bottomia. Further the  $R_{AA}^{\text{QGP}}$ -profiles are very similar among states of equal principal quantum number  $n$ , but especially for the three states  $\chi_b(2P)$ ,  $\Upsilon(3S)$  and  $\chi_b(3P)$ . The large in-medium decay widths of these highly excited states result in almost complete suppression in the QGP so the overall QGP-suppression factor is non-zero only due to contributions from the peripheral collision regions where no QGP is formed. This explains the similarity in the suppression pattern since the survival zone of these three states is basically given by the collision geometry. Only for higher  $p_T$ -values a difference among the excited states can be noted since some fraction is created in the boundary region of the QGP and can escape the plasma, seeing a strongly red-shifted, effective temperature.

## 5.2 The decay cascade

In chapter 3 we have calculated bottomium wave functions and considered the effect of color screening, collisional damping and gluodissociation in order to obtain decay widths. Then in chapter 4 we have set up a numerical routine for hydrodynamic simulations of the QGP in the fireball. Finally, in the previous section we have combined the results of these two steps to calculate the QGP-suppression factor  $R_{AA}^{\text{QGP}}$ .

To obtain the experimentally measured suppression factor  $R_{AA}(\Upsilon(nS))$  from the QGP-suppression factors we need to calculate the fraction of  $\Upsilon(nS)$  that decay into dimuon pairs. Therefore we consider in this section the decay cascade of excited  $b\bar{b}$  states within the bottomium family. The corresponding decay channels are depicted in fig. 5.7 with their branching ratios as given by the PDG (Beringer et al., 2012). Since the branching ratios of the  $\chi_b(3P)$  have not been measured so far we resort to theoretical predictions of the partial widths (Daghighian and Silverman, 1987),

$$\begin{aligned}\Gamma_{\chi_b(3P) \rightarrow \Upsilon(3S)} &= 10.33 \text{ keV}, \\ \Gamma_{\chi_b(3P) \rightarrow \Upsilon(2S)} &= 3.36 \text{ keV}, \\ \Gamma_{\chi_b(3P) \rightarrow \Upsilon(1S)} &= 3.16 \text{ keV},\end{aligned}\tag{5.10}$$

which are obtained from the widths for  $\chi_{bJ}(3P)$ -decays by averaging over total angular momentum  $J$ , weighted with the multiplicity  $2J + 1$ . The partial widths for the decays  $\chi_b(3P) \rightarrow \chi_b(1P)$  and  $\chi_b(3P) \rightarrow \chi_b(2P)$  have

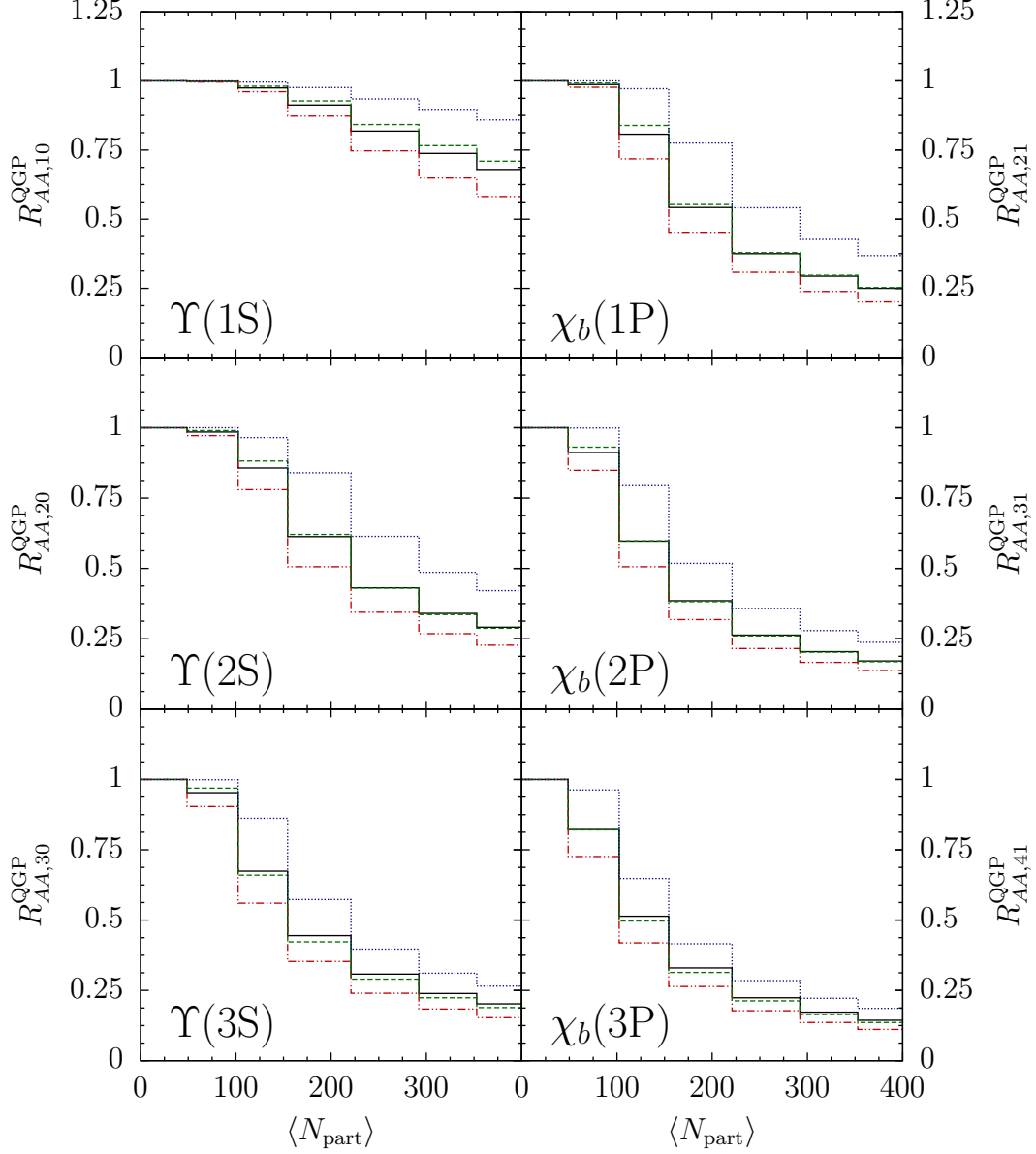


Figure 5.6: QGP-suppression factors  $R_{AA}^{\text{QGP}}$  for the different bottomonium states for IC1,  $T_0 = 650$  MeV,  $\tau_{\text{init}} = 0.1$  fm/c,  $\tau_{F,nl} = 0.1$  fm/c (for all states) with transverse momentum  $p_T = 0, 6, 12$  GeV/c (red, green and blue lines, respectively) and averaged over all  $p_T$ -values (black lines). The stable  $\Upsilon(1S)$ -ground state is significantly less suppressed than the higher excited states. In general the  $p_T$ -averaged results are close to the result for  $p_T = 6$  GeV/c  $\approx \langle p_T \rangle$ . See text for more information.

not been calculated. Assuming they are much smaller than the width for  $\chi_b(3P)$  decaying into  $\Upsilon(nS)$ , they are simply set to  $10^{-7}$  keV in this thesis. The total decay width of the  $\chi_b(3P)$  is also undetermined, experimentally as well as theoretically, and hence only the relative sizes of the  $\chi_b(3P)$ -branching ratios are known. The absolute values are obtained by scaling with a common factor. However, we will see later that it is possible to absorb this factor into the initial conditions so it cancels out in the final results. Consequently our ignorance about the value of the total width does not introduce another free parameter into the model.

Let  $N_I^0$  and  $N_n^\mu$  denote the number of bottomium states  $I$  produced initially on average in a collision event ( $pp$  or PbPb) and the number of dimuon pairs that originate from the decay  $\Upsilon(nS) \rightarrow \mu^+\mu^-$ , respectively. The bottomium states  $(n-l, l)$  are identified with  $I$  by means of the following enumeration:

$$\begin{aligned} 1S &\hat{=} 1, & 2P &\hat{=} 4, \\ 1P &\hat{=} 2, & 3S &\hat{=} 5, \\ 2S &\hat{=} 3, & 3P &\hat{=} 6. \end{aligned} \quad (5.11)$$

Let further  $\mathcal{M}$  denote the  $3 \times 6$ -matrix that connects  $N_I^0$  to  $N_n^\mu$  via

$$N_n^\mu = \sum_I \mathcal{M}_{nI} N_I^0. \quad (5.12)$$

Let us postpone the specific definition of  $\mathcal{M}$  for the moment. With given  $N_I^0$  the linear system of equations (5.12) may be solved for  $N_n^\mu$ . On the other hand, we may also solve for  $N_I^0$  if the dimuon yields  $N_n^\mu$  are given together with data on the  $\chi_b(nP)$ -states (keep in mind that  $\mathcal{M}$  is not a square matrix). Given the initially produced bottomia  $N_I^0$  in  $pp$ -collisions, the numbers of initially produced bottomia in PbPb collisions should then be the same, up to a factor of proportionality. This is due to the fact that bottomia are produced in the very early collision phase, where only the number of binary collisions should play a role but no medium effects. Since the calculation of  $R_{AA}$  involves a ratio, the factor of proportionality will cancel out so we can directly use the  $pp$ -results for  $N_I^0$  in the PbPb case.

The amount of suppression in the QGP in PbPb collisions can be included in the calculation by inserting  $R_{AA}^{\text{QGP}}$  in eq. (5.12),

$$N_n^\mu(c, p_T) = \sum_I \mathcal{M}_{nI} N_I^0 R_{AA,I}^{\text{QGP}}(c, p_T), \quad (5.13)$$

i.e. we calculate the decay cascade with the reduced population  $N_I^0 R_{AA,I}^{\text{QGP}}$ . Thus we are ready to properly write down the observable suppression factor

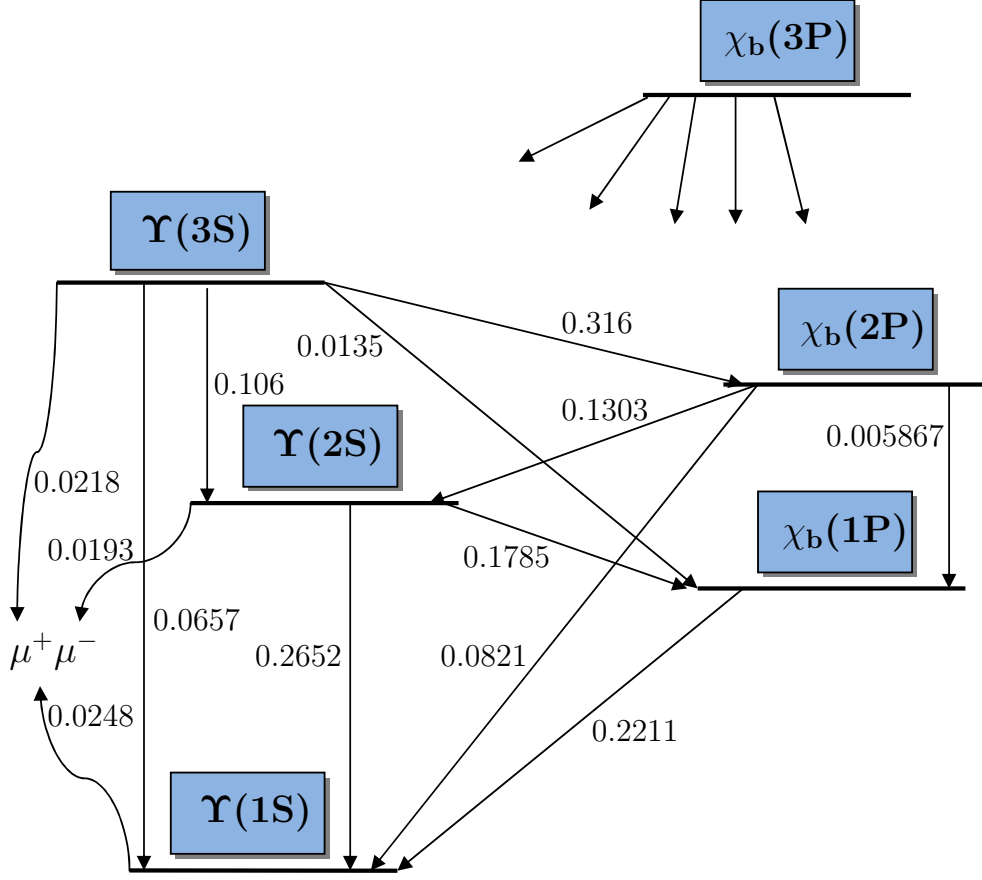


Figure 5.7: Schematic illustration of the decay channels within the bottomium family and from  $\Upsilon(nS)$  into dimuon pairs. The corresponding branching ratios are taken from the PDG (Beringer et al., 2012). The partial widths of the  $\chi_b(3P)$ , which has recently been discovered at ATLAS (Aad et al., 2012), are not yet measured but are taken from a theoretical model (Daghighian and Silverman, 1987). Its total width is also unknown but cancels out in the final result.

$R_{AA} = R_{AA}(\Upsilon(nS), c, p_T)$ , which compares the dimuon yields  $N_n^\mu$  in PbPb- and  $pp$ -collisions for  $\Upsilon(nS)$  states measured in the centrality bin  $b_c \leq b < b_{c+1}$  with transverse momentum  $p_T$ ,

$$R_{AA}(\Upsilon(nS), c, p_T) = \frac{\sum_I \mathcal{M}_{nI} N_I^0 R_{AA,I}^{\text{QGP}}(c, p_T)}{\sum_I \mathcal{M}_{nI} N_I^0}. \quad (5.14)$$

Let us now concentrate on the matrix  $\mathcal{M}$ , which describes the decay of  $\Upsilon(nS)$  states into dimuon pairs, given an initial bottomium population  $N_I^0$ . Considering decays within the bottomium family and into dimuon pairs, we

have the following rate equations in the bottomium rest-frame:

$$\begin{aligned}\frac{dN_I}{dt}(t) &= -\Gamma_I N_I(t) + \sum_{J>I} \Gamma_{IJ} N_J(t), \\ \frac{dN_n^\mu}{dt}(t) &= \Gamma_{\mu,nS} N_{nS}(t),\end{aligned}\tag{5.15}$$

where  $N_I(0) = N_I^0$ ,  $t$  is the time coordinate in the bottomium rest-frame,  $\Gamma_I$  and  $\Gamma_{IJ}$  are the total width of state  $I$  and partial widths for the decay  $J \rightarrow I$ , respectively, and  $\Gamma_{\mu,nS}$  is the partial width for the decay  $\Upsilon(nS) \rightarrow \mu^+ \mu^-$ . A state  $I = (n - l, l)$  is considered "smaller" than a state  $J = (n' - l', l')$  if

$$I < J \quad \Leftrightarrow \quad (n < n') \vee (n = n' \wedge l > l').\tag{5.16}$$

The meaning of the first line of eqs. (5.15) is therefore quite intuitively that the number of bottomium states  $I$  decreases through various decay channels with total width  $\Gamma_I$  while at the same time it receives contributions from higher excited states  $J$  through channels with partial width  $\Gamma_{IJ}$ .

Let us further rewrite eqs. (5.15) in terms of the branching ratios

$$B_{IJ} = \frac{\Gamma_{IJ}}{\Gamma_J}, \quad \text{for } I < J,\tag{5.17}$$

so that

$$\begin{aligned}\Gamma_I N_I(t) &= -\frac{dN_I}{dt}(t) + \sum_{J>I} B_{IJ} \Gamma_J N_J(t), \\ \frac{dN_n^\mu}{dt}(t) &= B_{\mu^\pm, nS} \Gamma_{nS} N_{nS}(t).\end{aligned}\tag{5.18}$$

It is now apparent that the first line of eqs. (5.18) gives a recursive relation, expressing the number of states  $I$  in terms of its rate of change  $dN_I/dt$  and the numbers of higher excited states. For the  $\chi_b(3P)$ , the highest excited state known to lie below the  $B\bar{B}$ -threshold, the first line of eqs. (5.18) reads

$$\Gamma_6 N_6(t) = -\frac{dN_6}{dt}(t).\tag{5.19}$$

Hence we are able to define a "cumulative-decay" (CD) matrix  $\mathcal{C}$  such that

$$\Gamma_I N_I(t) = -\sum_J \mathcal{C}_{IJ} \frac{dN_J}{dt}(t),\tag{5.20}$$

Table 5.1: Entries of the CD matrix  $\mathcal{C}$  derived from the branching ratios given by the PDG (Beringer et al., 2012). Transitions including the  $\chi_b(3P)$  are only determined up to a common factor given by its total decay width  $\Gamma_6$ .

	$\Upsilon(1S)$	$\chi_b(1P)$	$\Upsilon(2S)$	$\chi_b(2P)$	$\Upsilon(3S)$	$\chi_b(3P)$
$\Upsilon(1S)$	1	0.2211	0.3047	0.1231	0.1399	$5.627/\Gamma_6[\text{keV}]$
$\chi_b(1P)$	0	1	0.1785	0.02913	0.04163	$1.029/\Gamma_6[\text{keV}]$
$\Upsilon(2S)$	0	0	1	0.1303	0.1472	$4.876/\Gamma_6[\text{keV}]$
$\chi_b(2P)$	0	0	0	1	0.316	$3.265/\Gamma_6[\text{keV}]$
$\Upsilon(3S)$	0	0	0	0	1	$10.33/\Gamma_6[\text{keV}]$
$\chi_b(3P)$	0	0	0	0	0	1

where (Vaccaro, 2013)

$$\mathcal{C}_{IJ} = \begin{cases} \sum_{K=I+1}^J B_{IK} \mathcal{C}_{KJ}, & I < J \\ 1, & I = J \\ 0, & I > J \end{cases}. \quad (5.21)$$

The CD matrix describes the decay of a state  $J$  into a lower lying state  $I$ , accumulating contributions from all possible channels within the bottomium family, including intermediate states  $K$  with  $J \geq K > I$ . Its entries are listed in tab. 5.1 as calculated from the branching ratios given by the PDG (Beringer et al., 2012). As already mentioned, transitions including the  $\chi_b(3P)$  are only determined up to a common factor given by its total decay width  $\Gamma_6$ .

We may now insert eq. (5.20) into the second line of eqs. (5.18) and integrate from 0 to  $\infty$  to solve for the number of dimuon pairs  $N^\mu(\infty)$ . Since no dimuon pairs from  $\Upsilon(nS)$ -decays are present initially,  $N_n^\mu(0) = 0$ , and no bottomium states survive in the limit  $t \rightarrow \infty$ ,  $N_I(\infty) = 0$ , we obtain

$$N_n^\mu(\infty) = B_{\mu^\pm, nS} \sum_J \mathcal{C}_{nS, J} N_J^0. \quad (5.22)$$

Comparing with eq. (5.12) shows that the matrix  $\mathcal{M}$  is given in terms of the CD matrix by

$$\mathcal{M}_{nI} = B_{\mu^\pm, nS} \mathcal{C}_{nS, I}. \quad (5.23)$$

To match the yields from eqs. (1.9), measurement by the CMS experiment, we define scaled dimuon- and initial bottomium-numbers,  $\mathcal{N}_n^\mu$  and  $\mathcal{N}_I^0$  via

$$\mathcal{N}_n^\mu = \frac{N_n^\mu(\infty)}{N_1^\mu(\infty)}, \quad \mathcal{N}_I^0 = \frac{N_I^0}{N_1^\mu(\infty)}, \quad (5.24)$$

which yields for the LHC  $pp$  run at  $\sqrt{s_{NN}} = 2.76$  TeV (Chatrchyan et al., 2012)

$$\mathcal{N}_1^\mu = 1, \quad \mathcal{N}_2^\mu = 0.56, \quad \mathcal{N}_3^\mu = 0.41. \quad (5.25)$$

In order to solve for the initial populations we make use of the CDF results for  $\Upsilon(1S)$ -feed down from  $\chi_b(nP)$  states in  $p\bar{p}$  collisions at  $\sqrt{s} = 1.8$  TeV. It has been found that  $[27.1 \pm 6.9$  (stat)  $\pm 4.4$  (sys)]% of the  $\Upsilon(1S)$  mesons come from  $\chi_b(1P)$ -decays, while  $[10.5 \pm 4.4$  (stat)  $\pm 1.4$  (sys)]% come from  $\chi_b(2P)$ -decays and the contribution from  $\chi_b(3P)$ -decays is estimated to be less than 6% (Affolder et al., 2000). In this thesis we will assume the  $\chi_b(3P)$ -contribution to be at the estimated upper limit,

$$\mathcal{M}_{12}\mathcal{N}_2^0 = 0.271, \quad \mathcal{M}_{14}\mathcal{N}_4^0 = 0.105, \quad \mathcal{M}_{16}\mathcal{N}_6^0 = 0.06. \quad (5.26)$$

With these input data we obtain the following, scaled initial populations:

$$\begin{aligned} \mathcal{N}_1^0 &= 13.8, & \mathcal{N}_2^0 &= 43.7, & \mathcal{N}_3^0 &= 17.7, \\ \mathcal{N}_4^0 &= 45.6, & \mathcal{N}_5^0 &= 10.9, & \mathcal{N}_6^0 &= 7.7 \Gamma_6[\text{keV}]. \end{aligned} \quad (5.27)$$

We find that the total width  $\Gamma_6$  indeed cancels out since  $\mathcal{N}_6^0$  is always multiplied by a factor  $\mathcal{M}_{n6}$  in the calculations.

Vaccaro et al. (2013) have found that the inclusion of the  $\chi_b(3P)$  state decreases the  $\Upsilon(1S)$  suppression factor at most by 7%.

The final results may now be obtained by inserting the QGP-suppression factors from section 5.1 into the cascade calculation outlined in this section. However, we postpone the presentation of the theoretical results to the next chapter, where they are compared to experimental results and their implications are discussed.



# Chapter 6

## Results and conclusions

In this chapter the final results of the thesis are present and discussed. In section 6.1 we present theoretical results for the suppression factors  $R_{AA}(\Upsilon(nS))$  as well as the  $\Upsilon(2S)$ - and  $\Upsilon(3S)$ -double ratios, both as functions of centrality and minimum bias values, and compare with experimental data. In section 6.2 we compare our results with other work in the literature. In section 6.3 we give a short summary of the model and discuss the implications of the results.

### 6.1 Theoretical results

We present theoretical results for  $R_{AA}(\Upsilon(1S))$ ,  $R_{AA}(\Upsilon(2S))$ ,  $R_{AA}(\Upsilon(3S))$ ,  $\frac{\Upsilon(2S)/\Upsilon(1S)|_{\text{PbPb}}}{\Upsilon(2S)/\Upsilon(1S)|_{pp}}$  and  $\frac{\Upsilon(3S)/\Upsilon(1S)|_{\text{PbPb}}}{\Upsilon(3S)/\Upsilon(1S)|_{pp}}$  in figs. 6.1 - 6.5 as  $p_T$ -averaged functions of centrality. The suppression factor  $R_{AA}(\Upsilon(1S))$  is also displayed in fig. 6.6 as centrality-averaged function of  $p_T$ .

As in figs. 5.5 and 5.6 we have plotted the theoretical results as average over centrality bins (see tab. 4.2) and not as continuous functions of centrality, because the latter would be misleading in the comparison with experimental data.

The centrality dependent results for  $R_{AA}(\Upsilon(1S))$ ,  $R_{AA}(\Upsilon(2S))$  and also  $\frac{\Upsilon(2S)/\Upsilon(1S)|_{\text{PbPb}}}{\Upsilon(2S)/\Upsilon(1S)|_{pp}}$  are compared with CMS data (Chatrchyan et al., 2012). Recent ALICE data (Manceau, 2013) is also displayed in fig. 6.1. Note, however, that ALICE has measured at rapidity  $2.5 < y < 4$  and CMS at  $y < 2.4$ . Also ALICE data is given for the centrality bins 0 - 20% and 20 - 90%, respectively, as opposed to the CMS centrality bins, which have been used for the theoretical results.

All theoretical results in this chapter have been calculated using  $\tau_{\text{init}} = 0.1$  fm/c and equal formation times  $\tau_{F,nl}$  for all states. We have calculated results

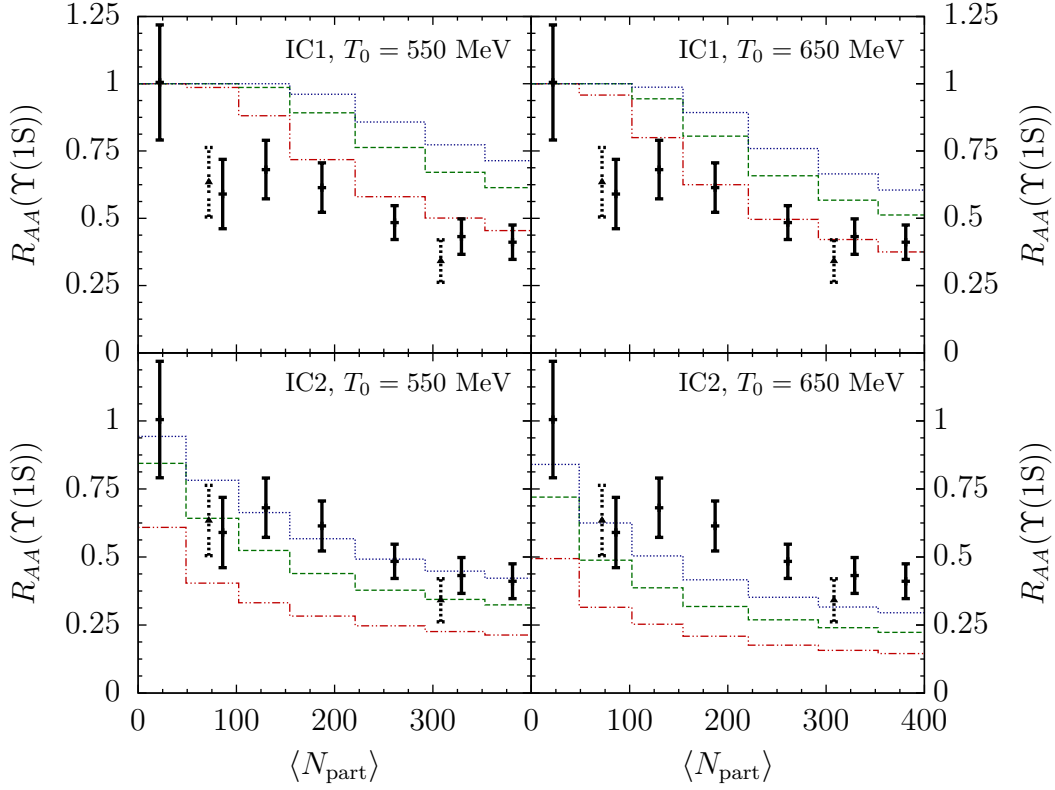


Figure 6.1: Results for  $R_{AA}(\Upsilon(1S))$  as a function of centrality, averaged over  $p_T$ , plotted for  $\tau_{F,nl} = 0.1, 0.3, 0.5$  fm/c (red, green, blue lines, respectively). CMS (Chatrchyan et al., 2012) and ALICE (Manceau, 2013) data are plotted in solid and dotted black, respectively.

for all combinations of initial conditions IC1, IC2, initial core temperatures  $T_0 = 550, 650$  MeV and formation times  $\tau_{F,nl} = 0.1, 0.3, 0.5$  fm/c. The average over transverse momentum has been calculated from results for  $p_T = 0$  up to 28 GeV/c in steps of 2 GeV/c.

The numerical calculation has been performed on a staggered grid with  $51 \times 51$  cell centers and a grid spacing of 0.2 fm (see chapter 4). While this appears to be a small grid, regarding e.g. the temperature profile for IC2 in fig. 4.3, it has been found that the final results do not change even within one order of magnitude more than the desired accuracy, if a larger grid is chosen.

It becomes apparent from figs. 6.1, 6.2 and 6.3 that the best agreement with experimental data is achieved for the two parameter combinations

$$\begin{array}{ll}
 \text{IC1} & \text{IC2} \\
 T_0 = 650 \text{ MeV} & T_0 = 550 \text{ MeV} \\
 \tau_{F,nl} = 0.1 \text{ fm/c} & \tau_{F,nl} = 0.5 \text{ fm/c}, \quad (6.1)
 \end{array}$$

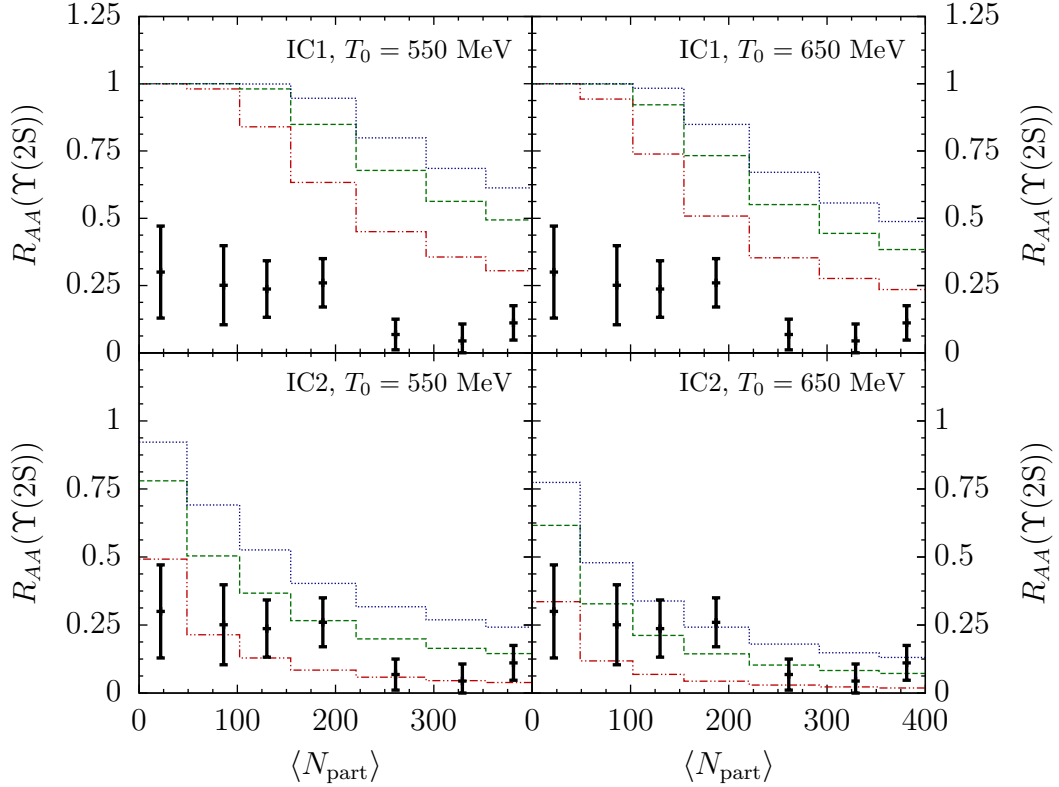


Figure 6.2: Results for  $R_{AA}(\Upsilon(2S))$  as a function of centrality, averaged over  $p_T$ , plotted for  $\tau_{F,nl} = 0.1, 0.3, 0.5$  fm/c (red, green, blue lines, respectively). CMS data (Chatrchyan et al., 2012) are plotted in black.

respectively, where slightly larger  $T_0$  or smaller  $\tau_{F,nl}$  for IC2 might improve the agreement even more. The theoretical minimum bias results are presented in tabs. 6.1 and 6.2, including  $R_{AA}(\Upsilon(3S))$  and  $\frac{\Upsilon(3S)/\Upsilon(1S)|_{\text{PbPb}}}{\Upsilon(3S)/\Upsilon(1S)|_{pp}}$ , where the best agreement with CMS data is achieved for the above combinations as well. The relative strength of the suppression of the  $\Upsilon(1S)$  ground state compared to the excited  $\Upsilon(2S)$  and  $\Upsilon(3S)$  states is better reproduced using IC2, which becomes evident from the plots of the  $\Upsilon(2S)$ -double ratio depicted in fig. 6.3.

Results for  $R_{AA}(\Upsilon(3S))$  and  $\frac{\Upsilon(3S)/\Upsilon(1S)|_{\text{PbPb}}}{\Upsilon(3S)/\Upsilon(1S)|_{pp}}$  as functions of centrality are depicted in figs. 6.4 and 6.5, respectively. However, no centrality dependent data are available from experiment.

There are two peculiarities in the centrality dependent CMS data for  $R_{AA}(\Upsilon(2S))$  (see fig. 6.2), however, which can not be reproduced by the model. First, there is strong suppression in the most peripheral bin, whereas the model predicts  $R_{AA}(\Upsilon(2S))$  to be close to one in this region. Second, there is a jump in the  $R_{AA}(\Upsilon(2S))$ -data from the 10 - 20% to the 20 - 30%

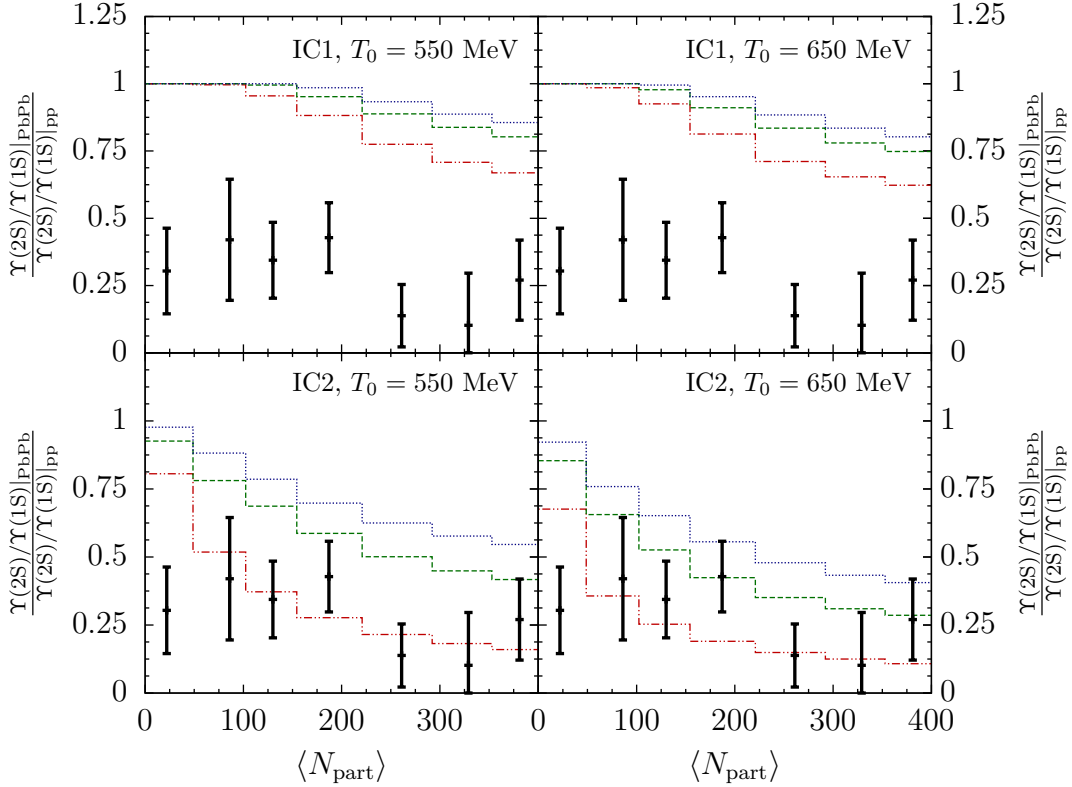


Figure 6.3: Results for  $\frac{\Upsilon(2S)/\Upsilon(1S)|_{\text{PbPb}}}{\Upsilon(2S)/\Upsilon(1S)|_{\text{pp}}}$  as a function of centrality, averaged over  $p_T$ , plotted for  $\tau_{F,nl} = 0.1, 0.3, 0.5$  fm/c (red, green, blue lines, respectively). CMS data (Chatrchyan et al., 2012) are plotted in black.

centrality bin. Experimental data of the double ratio  $\frac{\Upsilon(2S)/\Upsilon(1S)|_{\text{PbPb}}}{\Upsilon(2S)/\Upsilon(1S)|_{\text{pp}}}$  shows corresponding. Both points represent quite counter-intuitive results, which lack an explanation. Hence it is not unexpected that this model but also other theoretical approaches do not account for this behavior.

## 6.2 Comparison with other work

In the following we compare our results with recent, complementary work in the literature:

Emerick et al. (2012) have modeled bottomium suppression at RHIC and LHC following an earlier approach (Grandchamp et al., 2006; Zhao and Rapp, 2010; Zhao and Rapp, 2011). Bottomium properties are investigated in a weak and a strong binding scenario (WBS and SBS, respectively), where potential model parameters and spectral functions are checked against LQCD results.

Table 6.1: Minimum bias results for  $R_{AA}(\Upsilon(nS))$  and  $\frac{(\Upsilon(nS)/\Upsilon(1S))_{PbPb}}{(\Upsilon(nS)/\Upsilon(1S))_{pp}}$  using IC1,  $\tau_{\text{init}} = 0.1$  fm/c and different core temperatures  $T_0$  and formation times  $\tau_{F,nl}$ .

	$\tau_{F,nl}$ (fm/c)	0.1	0.3	0.5	CMS (Chatrchyan et al., 2012)
$T_0 = 550$ MeV	$R_{AA}(\Upsilon(1S))$	0.61	0.77	0.84	$0.56 \pm 0.08$ (stat) $\pm 0.07$ (sys)
	$R_{AA}(\Upsilon(2S))$	0.49	0.69	0.79	$0.12 \pm 0.04$ (stat) $\pm 0.02$ (sys)
	$R_{AA}(\Upsilon(3S))$	0.38	0.59	0.71	$0.03 \pm 0.04$ (stat) $\pm 0.01$ (sys)
	$\frac{(\Upsilon(2S)/\Upsilon(1S))_{PbPb}}{(\Upsilon(2S)/\Upsilon(1S))_{pp}}$	0.81	0.90	0.93	$0.21 \pm 0.07$ (stat) $\pm 0.02$ (sys)
	$\frac{(\Upsilon(3S)/\Upsilon(1S))_{PbPb}}{(\Upsilon(3S)/\Upsilon(1S))_{pp}}$	0.62	0.77	0.85	$0.06 \pm 0.06$ (stat) $\pm 0.06$ (sys)
$T_0 = 650$ MeV	$R_{AA}(\Upsilon(1S))$	0.53	0.68	0.76	$0.56 \pm 0.08$ (stat) $\pm 0.07$ (sys)
	$R_{AA}(\Upsilon(2S))$	0.40	0.58	0.68	$0.12 \pm 0.04$ (stat) $\pm 0.02$ (sys)
	$R_{AA}(\Upsilon(3S))$	0.31	0.49	0.60	$0.03 \pm 0.04$ (stat) $\pm 0.01$ (sys)
	$\frac{(\Upsilon(2S)/\Upsilon(1S))_{PbPb}}{(\Upsilon(2S)/\Upsilon(1S))_{pp}}$	0.77	0.86	0.90	$0.21 \pm 0.07$ (stat) $\pm 0.02$ (sys)
	$\frac{(\Upsilon(3S)/\Upsilon(1S))_{PbPb}}{(\Upsilon(3S)/\Upsilon(1S))_{pp}}$	0.59	0.72	0.79	$0.06 \pm 0.06$ (stat) $\pm 0.06$ (sys)

In the WBS bottomium properties are temperature dependent, with values according to a screened Cornell potential, whereas they remain constant at their vacuum values in the SBS. In-medium dissociation and regeneration is calculated using a rate equation approach, where regeneration is found to give significant contribution in the SBS only.

The processes under consideration are gluodissociation and “quasi-free dissociation”, the latter being the pendant to collisional damping. The evolution of the fireball is not modeled by a hydrodynamical approach but as an isentropically expanding, isotropic firecylinder.

Suppression by CNM effects is also regarded and found to play a moderate role, weaker at the LHC than at RHIC. Direct feed-down to the  $\Upsilon(1S)$  is considered in the calculation of the suppression factors, but not the complete decay cascade.

The authors agree with us about the fact that even at the LHC the  $\Upsilon(1S)$  is very stable against color screening. On the other hand, the authors argue that gluodissociation becomes inefficient for weakly bound quarkonium states, which contradicts our findings.

It has been pointed out in subsection 3.2.2 that the gluodissociation width  $\Gamma_{\text{diss}}$  of the  $\Upsilon(1S)$  is indeed relatively small, compared to  $\Gamma_{\text{damp}}$ , and achieves a maximum at a temperature  $T < T_m$ , when a constant coupling  $\alpha_{\text{eff}}$  is used. The running coupling, however, increases with temperature as the soft and ultra soft scales decrease. This results in higher melting temperatures and

Table 6.2: Minimum bias results for  $R_{AA}(\Upsilon(nS))$  and  $\frac{(\Upsilon(nS)/\Upsilon(1S))_{PbPb}}{(\Upsilon(nS)/\Upsilon(1S))_{pp}}$  using IC2,  $\tau_{\text{init}} = 0.1$  fm/c and different core temperatures  $T_0$  and formation times  $\tau_{F,nl}$ .

	$\tau_{F,nl}$ (fm/c)	0.1	0.3	0.5	CMS (Chatrchyan et al., 2012)
$T_0 = 550$ MeV	$R_{AA}(\Upsilon(1S))$	0.27	0.41	0.52	$0.56 \pm 0.08$ (stat) $\pm 0.07$ (sys)
	$R_{AA}(\Upsilon(2S))$	0.08	0.24	0.36	$0.12 \pm 0.04$ (stat) $\pm 0.02$ (sys)
	$R_{AA}(\Upsilon(3S))$	0.03	0.13	0.24	$0.03 \pm 0.04$ (stat) $\pm 0.01$ (sys)
	$\frac{(\Upsilon(2S)/\Upsilon(1S))_{PbPb}}{(\Upsilon(2S)/\Upsilon(1S))_{pp}}$	0.30	0.57	0.68	$0.21 \pm 0.07$ (stat) $\pm 0.02$ (sys)
	$\frac{(\Upsilon(3S)/\Upsilon(1S))_{PbPb}}{(\Upsilon(3S)/\Upsilon(1S))_{pp}}$	0.12	0.29	0.43	$0.06 \pm 0.06$ (stat) $\pm 0.06$ (sys)
$T_0 = 650$ MeV	$R_{AA}(\Upsilon(1S))$	0.20	0.30	0.39	$0.56 \pm 0.08$ (stat) $\pm 0.07$ (sys)
	$R_{AA}(\Upsilon(2S))$	0.05	0.14	0.22	$0.12 \pm 0.04$ (stat) $\pm 0.02$ (sys)
	$R_{AA}(\Upsilon(3S))$	0.02	0.07	0.13	$0.03 \pm 0.04$ (stat) $\pm 0.01$ (sys)
	$\frac{(\Upsilon(2S)/\Upsilon(1S))_{PbPb}}{(\Upsilon(2S)/\Upsilon(1S))_{pp}}$	0.22	0.44	0.55	$0.21 \pm 0.07$ (stat) $\pm 0.02$ (sys)
	$\frac{(\Upsilon(3S)/\Upsilon(1S))_{PbPb}}{(\Upsilon(3S)/\Upsilon(1S))_{pp}}$	0.09	0.22	0.32	$0.06 \pm 0.06$ (stat) $\pm 0.06$ (sys)

larger decay widths. It is evident from fig. (3.4) and tab. B.2 that at least for the  $\Upsilon(1S)$  the scale hierarchy stays intact up to the melting temperature of  $T_m = 655$  MeV  $\approx 3.9 T_c$  and that  $\Gamma_{\text{diss}}$  may not be neglected.

Song et al. (2011, 2012) propose a model for bottomium suppression in heavy ion collisions, which calculates in-medium production and dissociation from a rate equation. The cross section is taken from NLO results for gluodissociation (Song and Lee, 2005; Park et al., 2007). Wave functions and decay widths are calculated from a screened Cornell potential, i.e. the real part of the first line of eqs. (3.3).

The fireball is modeled as a viscous, cylindrically symmetric fluid and transversely averaged quantities are calculated. The inclusion of viscosity allows for lower temperatures at the same QGP lifetime as compared to perfect-fluid hydrodynamics.

The two effects of bottomium regeneration and gluonic (anti-) shadowing are also included in the model, but both effects are found to have only small impact on the final results. This finding supports the assumptions, made in this thesis, that CNM effects may be neglected for bottomia.

However, the model does not include an imaginary part in the potential to account for the significant contribution of collisional damping to the total width. Also the running of the strong coupling  $\alpha_s$  is not considered, which has the results mentioned above.

Strickland (2011); Strickland and Bazow (2012) model bottomium sup-

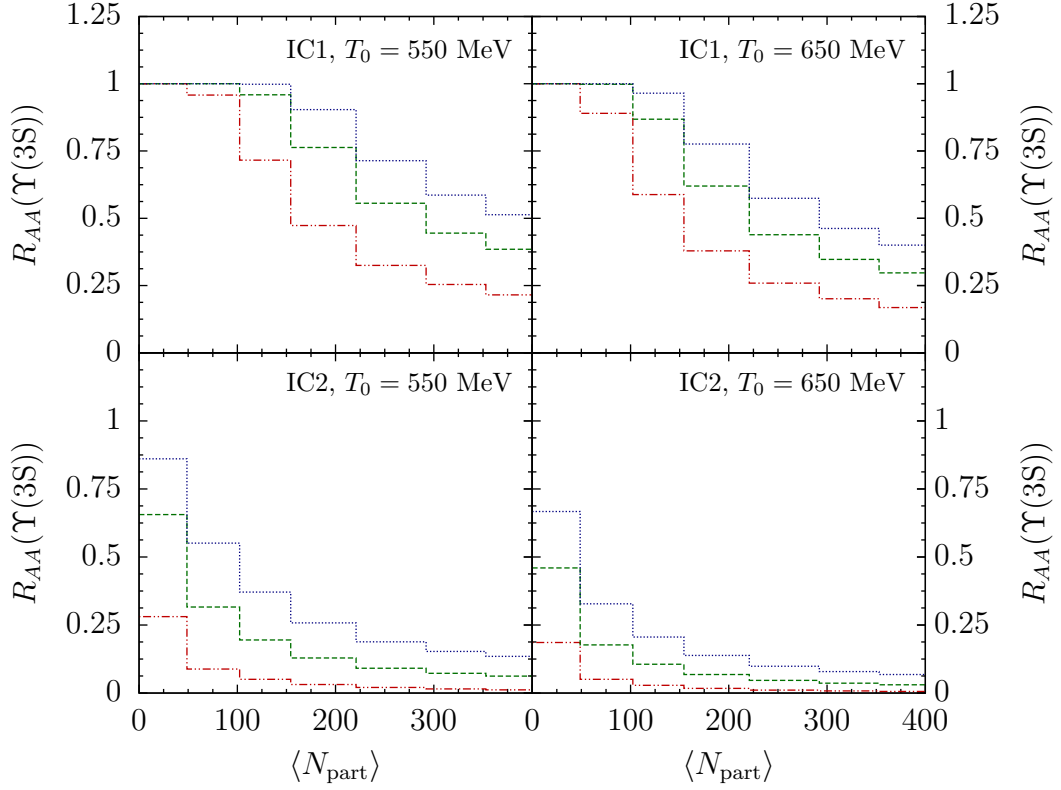


Figure 6.4: Results for  $R_{AA}(\Upsilon(3S))$  as a function of centrality, averaged over  $p_T$ , plotted for  $\tau_{F,nl} = 0.1, 0.3, 0.5$  fm/c (red, green, blue lines, respectively).

pression in heavy ion collisions by means of a non-relativistic, complex potential model, with parameters guided by LQCD results. Momentum-space anisotropies are taken into account both in the potential model and in the viscous, hydrodynamical model of the longitudinally expanding fireball.

While the model is able to reproduce RHIC and LHC data, including the effect of  $\Upsilon(1S)$ -feed down from excited states, it does not account for transverse expansion of the fireball and the full decay cascade. Also the running coupling is fixed in the potential model.

It is also worth noting that Alford and Strickland (2013) have investigated the dissociation of  $\Upsilon$  and  $J/\psi$  for a vacuum Cornell potential and their mixing with  $\eta_b$  and  $\eta_c$ , respectively, as induced by the strong magnetic fields present in the initial phase of a nucleus-nucleus collision.

While the effect appears to be significant for  $J/\psi$  production it amounts only to 2% for the  $\Upsilon$ . However, the effect is expected to be stronger in a thermal medium and for excited quarkonia. Since we have seen the strong effect of missing feed-down on the  $\Upsilon(1S)$  in chapters 5 and 6, there is the possibility of indirect  $\Upsilon(1S)$  suppression through strong magnetic fields.

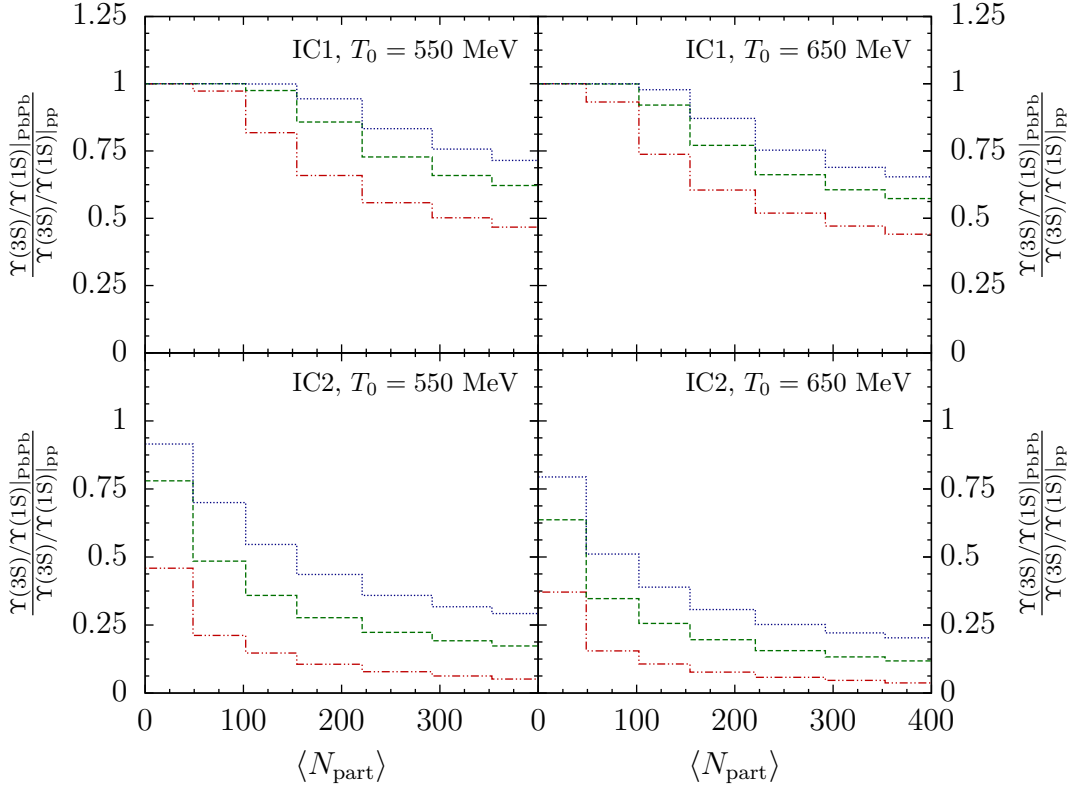


Figure 6.5: Results for  $\frac{\Upsilon(3S)/\Upsilon(1S)|_{\text{PbPb}}}{\Upsilon(3S)/\Upsilon(1S)|_{\text{pp}}}$  as a function of centrality, averaged over  $p_T$ , plotted for  $\tau_{F,nl} = 0.1, 0.3, 0.5$  fm/c (red, green, blue lines, respectively).

### 6.3 Summary and conclusions

Let us now summarize the essence of the model proposed in this thesis so we can properly interpret the results presented in the last section.

The model is based on the assumption that bottomia, and in particular the  $\Upsilon(1S)$ , are very stable bound states so that only very few processes can contribute to their suppression in the QGP. Therefore only the three processes of color screening, gluodissociation and collisional damping are considered.

Due to the large mass of the bottom quark non-relativistic methods become applicable. Hence, the framework of EFT and in particular pNRQCD represent a good starting point to treat bottomia immersed in a thermal medium. Keeping in mind the scale hierarchy exploited in the EFT framework it becomes clear that highly excited states can not be treated by means of pure pNRQCD (see tabs. B.5 - B.7). Since our potential model is motivated by pNRQCD, however, we have included the non-perturbative string

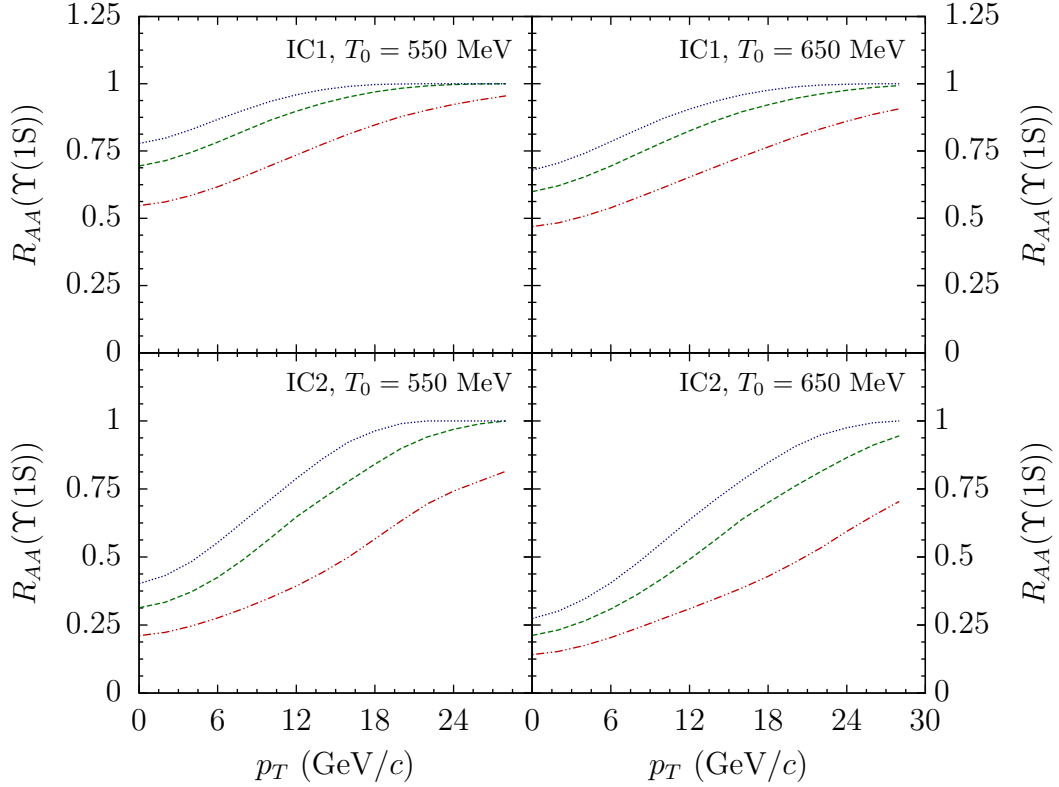


Figure 6.6: Results for  $R_{AA}(\Upsilon(1S))$  as a function of  $p_T$ , averaged over centrality, plotted for  $\tau_{F,nl} = 0.1, 0.3, 0.5$  fm/c (red, green, blue lines, respectively).

contribution into the interaction potentials to try and justify the treatment of very important states  $\chi_b(2P)$ ,  $\Upsilon(3S)$  and  $\chi_b(3P)$ .

A major improvement over our recent work (Brezinski and Wolschin, 2012; Nendzig and Wolschin, 2013) is the inclusion of the running coupling into the Schrödinger equation. Not only does the running of the coupling increase the melting temperatures, especially for the excited states, but the increased ultra soft coupling also results in a significantly larger gluodissociation decay width.

The in-medium decay widths and melting temperatures obtained in this way are then inserted into a hydrodynamical model of the fireball, where the QGP is treated as a relativistic, perfect fluid. The evolution of the fireball temperature and transverse velocity is calculated numerically, where we have improved the model significantly, compared to Nendzig and Wolschin (2013), by taking into account the transverse expansion. Furthermore, we account for finite transverse momenta of bottomia and their relative velocities with respect to the surrounding QGP by means of an effective temperature.

In this way we are able to quantify the amount of suppression of bot-

tomia in the QGP in terms of a QGP-suppression factor  $R_{AA}^{\text{QGP}}$ . The final suppression factor  $R_{AA}$  is then calculated from  $R_{AA}^{\text{QGP}}$  by performing a decay cascade calculation and compared to the available data.

Comparing the results for the QGP-suppression factor  $R_{AA}^{\text{QGP}}(\Upsilon(1S))$  in fig. 5.5 with the results for  $R_{AA}(\Upsilon(1S))$  in fig. 6.1 shows that, depending on the parameters, missing feed-down from the excited states constitutes a major or even the largest part of the  $\Upsilon(1S)$ -suppression. Missing feed-down is, however, only a result of the strong suppression of the excited states in the QGP and is therefore not regarded as an independent process.

The relatively simple picture exploited in this model, which presently does not include CNM effects, is supported to a large extent by experimental data (see figs. 6.1, 6.2 and 6.3 as well as tabs. 6.1 and 6.2). On the other hand, the model deviates from experiment on the relative strength of the suppression of the  $\Upsilon(1S)$  ground state and the excited  $\Upsilon(2S)$  and  $\Upsilon(3S)$  states. While the deviation is quite significant for IC1, it is not so prominent if IC2 is used. However, it appears unlikely to us that this issue can be cured by a clever choice of parameters alone.

It appears doubtful to us whether stronger, relative suppression of the excited states can be attained by inclusion of CNM effects as they should influence all states almost equally and therefore essentially cancel out in the ratio.

We conjecture that a refined treatment of the formation times could resolve the issue since shorter formation times for the excited states would result in stronger suppression. However, this would also result in additional suppression of the  $\Upsilon(1S)$  by missing feed-down. Consequently the suppression pattern can only be improved by means of modified formation times if a good balance between these two effects can be found.

The model presented in this thesis is able to reproduce experimental data to a good extent, but the current picture has to be refined if higher accuracy is desired. The broad range of different approaches in the field shows, however, that a full account of the phenomenon of  $\Upsilon$  suppression in relativistic heavy ion collisions at the LHC is a very ambitious goal.

Straightforward improvements of the model are e.g. the inclusion of CNM effects, statistical recombination or considering the effect of an anisotropic, effective temperature in the QGP.

Probably the most interesting, outstanding problem concerns the gluodissociation cross section. If the full, complex Hamiltonian is considered for the intermediate octet states, instead of the pure Coulomb Hamiltonian as in this thesis, the subsequent calculation changes dramatically. This and other interesting, theoretical questions, however, are left for future work.

# Acknowledgments

## I wish to thank...

- ... my supervisor Prof. Dr. *Georg Wolschin* who introduced me to this interesting topic that allowed me to jump from the world of the really big into the world of the really small. Also I would like to thank him for all the time he invested in me, always being patient (even when he had a lot of work), and for his help, encouragement and advice in all concerns.
- ... the IMPRS-PTFS, especially Dr. *Werner Rodejohann*, for granting financial support that allowed me to graduate and to visit international conferences; but also *Britta Schwarz* for always friendly support (and because she saved my application from getting lost only a few days before the deadline).
- ... *Johannes, Francesco* and *Thilo* because all their work and effort contributed substantially to my thesis and helped a lot to improve it.
- ... Priv.-Doz. Dr. *Klaus Reygers* for agreeing to be my second referee and part of my committee and for useful tips about the Glauber calculation.
- ... Prof. Dr. *Carlo Ewerz* and Prof. Dr. *Johanna Stachel* because they agreed to be my co-supervisors and for many helpful suggestions and discussions that improved my thesis.
- ... Prof. Dr. *Matthias Bartelmann* and Prof. Dr. *Eva Grebel* for agreeing to be part of my committee.
- ... Dr. *Dimitri Antonov*, Prof. Dr. *Jean-Paul Blaizot* and Prof. Dr. *Michael Strickland* for many interesting and helpful discussions, tips, suggestions, hints etc.
- ... Dr. *Stefan Floerchinger* for helping me to check the hydro-code.

... my parents *Enno* and *Beate*, who have always supported me in every possible way, my grandfather *Norbert*, because he awakened my enthusiasm for astronomy and physics in general, my grandmother *Karin* for culinary support and my grandfather *Dieter* for his interest and support.

... my parents-in-law *Sabine* and *Anton* and my grandparents-in-law *Gina* and *Rudi*, who supported me in many ways.

... *Lucy* and *Ponne*, who cross-checked my notes by sleeping on them.

... *Simone*, the most lovely and supporting wife that one can wish for.

# Appendix A

## Basic calculations in finite temperature field theory

To keep this work as self-contained as possible we briefly recall some basic expressions and calculations of thermal field theory in section A.1. The one-loop gluon polarization tensor needed in chapter 2 is calculated in the HTL approximation in section A.2. For a more detailed information see e.g. Kapusta (1989); Le Bellac (2000); Blaizot and Iancu (2002).

### A.1 Thermal propagators

First we derive the thermal propagator for a scalar field. The result can then be used to conveniently derive expressions for the thermal propagators of fermions and photons. In turn, the gluon propagator may be readily obtained from the photon propagator.

The thermal propagator of a scalar satisfies

$$(-\partial^2 + m^2) \Delta(x) = \delta^4(x), \quad \Delta(\tau - \beta, \vec{x}) = \pm \Delta(\tau, \vec{x}), \quad (\text{A.1})$$

where  $x = (\tau, \vec{x})$  and  $\partial^2 = \partial_\tau^2 + \Delta$ . The periodic condition is relevant for bosons and the antiperiodic for fermions. The most convenient representation of this propagator is  $\Delta(\tau, \vec{k})$ , where a spatial Fourier transform has been performed. Since the propagator is (anti-) periodic in the imaginary time  $\tau$ , we may write it as

$$\Delta(\tau, \vec{k}) = \frac{1}{\beta} \sum_{n=-\infty}^{\infty} \frac{e^{-i\omega_n \tau}}{\omega_n^2 + \omega_k^2}, \quad \omega_k = \sqrt{\vec{k}^2 + m^2} \quad (\text{A.2})$$

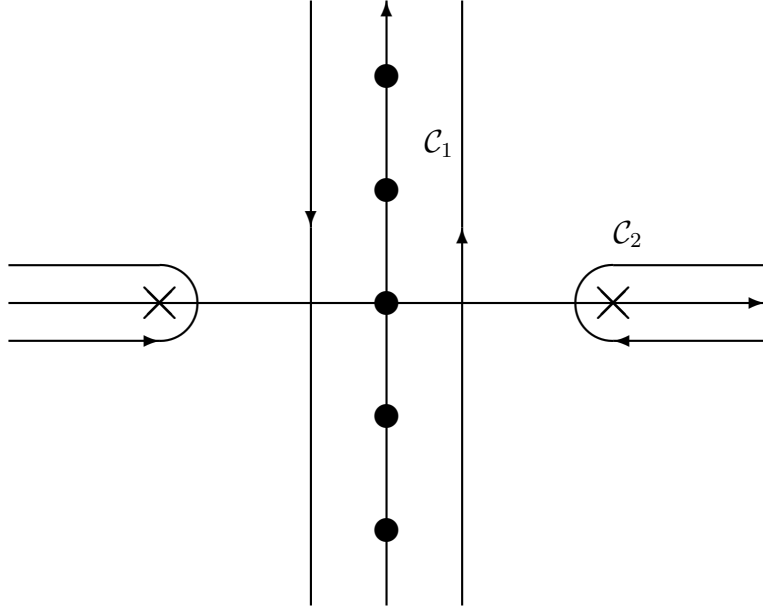


Figure A.1: Contour for the thermal propagator in eq. (A.2). The choice of  $\mathcal{C}_1$  yields the sum over Matsubara frequencies, while  $\mathcal{C}_2$  yields the residues of the two poles at  $\pm\omega_k$ .

where  $\omega_n = 2\pi n/\beta$  (bosons) or  $\omega_n = 2\pi(n + 1/2)/\beta$  (fermions) for  $n \in \mathbb{N}$ . In many cases it is convenient to rewrite the frequency sum in eq. (A.2) as

$$\frac{1}{\beta} \sum_{n=0}^{\infty} f(i\omega_n) = \int_{\mathcal{C}} \frac{dk^0}{2\pi i} \frac{f(k^0)}{2} \begin{cases} \coth(\beta k^0/2), & \text{periodic} \\ \tanh(\beta k^0/2), & \text{antiperiodic} \end{cases}, \quad (\text{A.3})$$

where the contour  $\mathcal{C} = \mathcal{C}_1$  is depicted in fig. A.1. This expression may be rewritten as

$$\begin{aligned} \frac{1}{\beta} \sum_{n=0}^{\infty} f(i\omega_n) &= \int_{-i\infty+\varepsilon}^{i\infty+\varepsilon} \frac{dk^0}{2\pi i} f(k^0) \left( \frac{1}{2} + \frac{1}{\pm \exp[\beta k^0] - 1} \right) \\ &\quad - \int_{i\infty-\varepsilon}^{-i\infty-\varepsilon} \frac{dk^0}{2\pi i} f(k^0) \left( \frac{1}{2} + \frac{1}{\pm \exp[-\beta k^0] - 1} \right), \end{aligned} \quad (\text{A.4})$$

where the upper (lower) sign refers to the (anti-) periodic case. Let us now define

$$n^{\pm}(k^0) = \frac{1}{e^{\beta k^0} \mp 1}, \quad (\text{A.5})$$

where  $n^+ = N$  is the Bose-Einstein distribution and  $n^- = n$  is the Fermi-Dirac distribution. The sum then reads

$$\frac{1}{\beta} \sum_{n=0}^{\infty} f(i\omega_n) = \int_{-i\infty+\varepsilon}^{i\infty+\varepsilon} \frac{dk^0}{2\pi i} (f(k^0) + f(-k^0)) \left( \frac{1}{2} \pm n^{\pm}(k^0) \right). \quad (\text{A.6})$$

The first term on the right-hand side represents the vacuum contribution to the frequency sum and the second term the medium contribution. The vacuum part is already present at  $T = 0$ , while the medium contribution exists only for finite temperature.

We may now write the scalar propagator in eq. (A.2) as

$$\Delta(\tau, \vec{k}) = \int_{-i\infty}^{i\infty} \frac{dk^0}{2\pi i} \frac{e^{-k^0\tau}}{-k^{02} + \omega_k^2} \pm \int_{-i\infty+\varepsilon}^{i\infty+\varepsilon} \frac{dk^0}{2\pi i} \frac{e^{k^0\tau} + e^{-k^0\tau}}{-k^{02} + \omega_k^2} n^{\pm}(k^0). \quad (\text{A.7})$$

The contour in the second integral may be deformed into  $\mathcal{C}_2$  (see fig. A.1) hereby picking up the pole at  $k^0 = \omega_k$ ,

$$\Delta(\tau, \vec{k}) = \frac{\Theta(\tau)e^{-\omega_k\tau} + \Theta(-\tau)e^{\omega_k\tau}}{2\omega_k} \pm \frac{e^{\omega_k\tau} + e^{-\omega_k\tau}}{2\omega_k} n^{\pm}(\omega_k). \quad (\text{A.8})$$

Another, very convenient way to express the thermal propagator is to use the the free particle spectral function,

$$\begin{aligned} \rho_0(k) &= 2\pi \operatorname{sgn}(k^0) \delta(k^2 + m^2) \\ &= \frac{\pi}{\omega_k} (\delta(k^0 - \omega_k) - \delta(k^0 + \omega_k)), \end{aligned} \quad (\text{A.9})$$

so that eq. (A.2) becomes

$$\Delta(\tau, \vec{k}) = \int \frac{dk^0}{2\pi} e^{-k^0\tau} \rho_0(k) (\Theta(\tau) \pm n^{\pm}(k^0)). \quad (\text{A.10})$$

Using the identity

$$n^{\pm}(-x) = \mp(1 \pm n^{\pm}(x)), \quad (\text{A.11})$$

one can show the equivalence between eqs. (A.8) and (A.10). From these results, we may readily derive the thermal fermion propagator, which is given by

$$S(k) = (-\not{k} + m)\Delta(k), \quad S(\tau - \beta, \vec{k}) = -S(\tau, \vec{k}). \quad (\text{A.12})$$

Since the fermion propagator satisfies antiperiodic boundary conditions, we have

$$S(\tau, \vec{k}) = \int \frac{dk^0}{2\pi} e^{-k^0\tau} \rho_0(k) (-\not{k} + m) (\Theta(\tau) - n(k^0)). \quad (\text{A.13})$$

The thermal photon propagator is also readily obtained in principle from the scalar field propagator. However, due to gauge freedom one can not give a general expression. Specializing to  $R_\xi$ -gauge, for example, yields

$$\Delta_{\mu\nu}(k) = \eta_{\mu\nu}\Delta(k) + (\xi - 1)k_\mu k_\nu \Delta^2(k). \quad (\text{A.14})$$

In this thesis we make use of Coulomb-gauge which is appropriate for the non-relativistic treatment of the heavy quarks. In this gauge, the thermal photon propagator reads

$$\begin{pmatrix} \Delta_{00}(k) & \Delta_{0i}(k) \\ \Delta_{i0}(k) & \Delta_{ij}(k) \end{pmatrix} = \begin{pmatrix} -\Delta(k) & 0 \\ 0 & \delta_{ij}\Delta(k) - k_i k_j \Delta^2(k) \end{pmatrix}. \quad (\text{A.15})$$

## A.2 The polarization tensor

Let us now calculate the one-loop gluon polarization tensor  $\Pi^{\mu\nu}$  as given in eq. (2.25) in Coulomb gauge. It contains contributions from light quarks, which can be treated as massless. As a function of the complex variable  $q^0$ , the polarization tensor reads

$$\Pi^{\mu\nu}(q^0, \vec{q}) = -\frac{N_{\text{dof}} g^2}{2\beta} \int \frac{d^3 p}{(2\pi)^3} \sum_{m=0}^{\infty} \text{Tr} [S(i\omega_m, \vec{p}) \gamma^\mu S(i\omega_m - q^0, \vec{p} - \vec{q}) \gamma^\nu], \quad (\text{A.16})$$

where  $N_{\text{dof}}$  is the number of the light fermion degrees of freedom. Since we are interested in a QCD plasma we have inserted an additional factor of  $1/2$  in this expression which arises from the trace over color indices.

By means of the identity

$$\frac{1}{\beta} \sum_{n=0}^{\infty} e^{i\omega_n \tau} = \sum_{l=-\infty}^{\infty} (-1)^l \delta(\tau - l\beta), \quad (\text{A.17})$$

we may rewrite the polarization tensor as

$$\Pi^{\mu\nu}(q) = \frac{N_{\text{dof}} g^2}{2} \int \frac{d^3 p}{(2\pi)^3} \int_0^\beta d\tau e^{-q^0 \tau} \text{Tr} [S(\beta - \tau, \vec{p}) \gamma^\mu S(\tau, \vec{p} - \vec{q}) \gamma^\nu], \quad (\text{A.18})$$

where

$$S(i\omega_n, \vec{p}) = \int_0^\beta d\tau e^{i\omega_n \tau} S(\tau, \vec{p}), \quad S(\tau, \vec{p}) = \sum_{n=0}^{\infty} e^{-i\omega_n \tau} S(i\omega_n, \vec{p}). \quad (\text{A.19})$$

Inserting the expression (A.13) into eq. (A.18) and writing  $p_1 = p$ ,  $p_2 = p - q$  yields

$$\begin{aligned} \frac{2\Pi^{\mu\nu}(q)}{N_{\text{dof}}g^2} &= \int \frac{d^3p}{(2\pi)^3} \int_0^\beta d\tau e^{-q^0\tau} \text{Tr} [S(\beta - \tau, \vec{p}_1)\gamma^\mu S(\tau, \vec{p}_2)\gamma^\nu] \\ &= \int \frac{d^3p}{(2\pi)^3} \frac{dp_1^0 dp_2^0}{(2\pi)^2} \int_0^\beta d\tau e^{-p_1^0\beta + (p_1^0 - p_2^0 - q^0)\tau} \rho_0(p_1)\rho_0(p_2) \\ &\quad \cdot \text{Tr}[\not{p}_1 \gamma^\mu \not{p}_2 \gamma^\nu] (1 - n(p_1^0))(1 - n(p_2^0)). \end{aligned} \quad (\text{A.20})$$

Calculating the trace and using the  $\delta$ -functions from the spectral functions yields

$$\begin{aligned} \frac{\Pi(q)}{N_{\text{dof}}g^2} &= 2 \int \frac{d^3p}{(2\pi)^3} \frac{dp_1^0 dp_2^0}{(2\pi)^2} \frac{n(p_2^0) - n(p_1^0)}{q^0 + p_2^0 - p_1^0} \rho_0(p_1)\rho_0(p_2) \\ &\quad \cdot \begin{pmatrix} -p_1^0 p_2^0 - \vec{p}_1 \vec{p}_2 & -\vec{p}_1 p_2^0 - \vec{p}_2 p_1^0 \\ -\vec{p}_2 p_1^0 - \vec{p}_1 p_2^0 & \mathbf{1}(p_1 p_2) - \vec{p}_1 \otimes \vec{p}_2 - \vec{p}_2 \otimes \vec{p}_1 \end{pmatrix} \\ &= \int \frac{d^3p}{(2\pi)^3 \omega_1 \omega_2} \left[ \frac{n_2 - n_1}{q^0{}^2 - (\omega_1 - \omega_2)^2} \right. \\ &\quad \cdot \begin{pmatrix} -(\omega_1 - \omega_2)(\vec{p}_1 \vec{p}_2 + \omega_1 \omega_2) & -q^0(\vec{p}_2 \omega_1 + \vec{p}_1 \omega_2) \\ -q^0(\vec{p}_2 \omega_1 + \vec{p}_1 \omega_2) & (\omega_1 - \omega_2)(\mathbf{1}(\vec{p}_1 \vec{p}_2 - \omega_1 \omega_2) - \vec{p}_1 \otimes \vec{p}_2 - \vec{p}_2 \otimes \vec{p}_1) \end{pmatrix} \\ &\quad \left. - \frac{1 - n_1 - n_2}{q^0{}^2 - (\omega_1 + \omega_2)^2} \right. \\ &\quad \left. \cdot \begin{pmatrix} (\omega_1 + \omega_2)(\vec{p}_1 \vec{p}_2 - \omega_1 \omega_2) & -iq^0(\vec{p}_2 \omega_1 - \vec{p}_1 \omega_2) \\ -iq^0(\vec{p}_2 \omega_1 - \vec{p}_1 \omega_2) & (\omega_1 + \omega_2)(\mathbf{1}(\vec{p}_1 \vec{p}_2 + \omega_1 \omega_2) - \vec{p}_1 \otimes \vec{p}_2 - \vec{p}_2 \otimes \vec{p}_1) \end{pmatrix} \right]. \end{aligned} \quad (\text{A.21})$$

Taking the limit  $T \rightarrow 0$  of this expression would yield  $n_{1/2} \rightarrow 0$  so only the vacuum polarization,  $\Pi_{(0)} = \Pi|_{T=0}$ , remains.

In the HTL approximation, valid at high temperature, only the term  $\propto (n_2 - n_1)$  in eq. (A.21) contributes, since the dominant contribution comes from loop momenta  $p \sim T$ , whereas the external momenta are of order  $q \sim m_D \ll T$  (see e.g. Beraudo et al., 2008; Blaizot and Iancu, 2002).

In this case we may approximate

$$\omega_2 \approx p - q \cos \theta, \quad n_1 - n_2 \approx (\omega_1 - \omega_2)(\partial_\omega n)|_{\omega=p}, \quad (\text{A.22})$$

and obtain for the polarization tensor

$$\frac{\Pi(q)}{N_{\text{dof}}g^2} = \int \frac{d^3p}{(2\pi)^3} \frac{\partial_p n q \cos \theta}{q^{0^2} - q^2 \cos^2 \theta} \begin{pmatrix} 2q \cos \theta & \frac{q^0}{\omega_1 \omega_2} (\vec{p}_2 \omega_1 + \vec{p}_1 \omega_2) \\ \frac{q^0}{\omega_1 \omega_2} (\vec{p}_2 \omega_1 + \vec{p}_1 \omega_2) & \frac{q \cos \theta}{\omega_1 \omega_2} (\vec{p}_1 \otimes \vec{p}_2 + \vec{p}_2 \otimes \vec{p}_1) \end{pmatrix}. \quad (\text{A.23})$$

The 00-component of the polarization tensor is readily calculated,

$$\begin{aligned} \frac{\Pi^{00}(q)}{N_{\text{dof}}g^2} &= \int \frac{dp p^2}{2\pi^2} \partial_p n \int_{-1}^1 d \cos \theta \frac{q^2 \cos^2 \theta}{q^{0^2} - q^2 \cos^2 \theta} \\ &= \frac{1}{3\beta^2} \left( 1 - \frac{q^0}{|\vec{q}|} \text{artanh} \frac{|\vec{q}|}{q^0} \right). \end{aligned} \quad (\text{A.24})$$

We define the Debye screening mass via

$$m_D^2 = \frac{N_{\text{dof}} g^2}{3 \beta^2}, \quad (\text{A.25})$$

to obtain

$$\Pi^{00}(q) = m_D^2 \left( 1 - \frac{q^0}{|\vec{q}|} \text{artanh} \frac{|\vec{q}|}{q^0} \right). \quad (\text{A.26})$$

Without loss of generality we take  $\vec{q} = q \vec{e}_z$  so  $\theta$  becomes the azimuth angle and we obtain for the  $i0$  and  $ij$  components of the polarization tensor

$$\begin{aligned} \frac{\Pi^{i0}(q)}{N_{\text{dof}}g^2} &= \delta^{i3} \int \frac{dp p^2 d \cos \theta}{(2\pi)^2} \frac{\partial_p n q \cos \theta}{q^{0^2} - q^2 \cos^2 \theta} \frac{q^0}{\omega_2} ((\omega_1 + \omega_2) \cos \theta - q) \propto \frac{\vec{q}}{q}, \\ \frac{\Pi^{ij}(q)}{N_{\text{dof}}g^2} &= \int \frac{dp p^2 d \cos \theta}{(2\pi)^2} \frac{\partial_p n q \cos \theta}{q^{0^2} - q^2 \cos^2 \theta} \frac{q \cos \theta}{\omega_1 \omega_2} \\ &\quad \cdot (p^2 \sin^2 \theta h^{ij} + 2(p^2 \cos^2 \theta - pq \cos \theta) P^{ij}) \\ &= \Pi_{\perp} h^{ij} + \Pi_{\parallel} P^{ij}, \end{aligned} \quad (\text{A.27})$$

where  $P^{ij} = \delta^{i3} \delta^{j3} = (\vec{q} \otimes \vec{q} / q^2)^{ij}$  and  $h^{ij} = \delta^{ij} - P^{ij}$ . Thus we can see that, if the polarization tensor is sandwiched between the gauge field  $A$ , as in eq. (2.24), the contribution of  $\Pi^{i0}$  vanishes since  $\vec{q} \vec{A}(q) = 0$  in Coulomb gauge.

# Appendix B

## Data tables

In this appendix we present tabulated data obtained from the theoretical model, which have been used in the figures of chapters 3 and 6.

### B.1 Results from the potential model

We present data on the partial decay widths  $\Gamma_{\text{damp}}$  and  $\Gamma_{\text{diss}}$ , obtained from the potential model, supplemented by the scales involved in the calculation.

Table B.1: Data on the  $\Upsilon(1S)$  from the potential model using the potential (3.12).

$T$ (MeV)	$m_D$ (MeV)	$\langle 1/r \rangle$ (MeV)	$\langle  V_{\text{eff}}  \rangle$ (MeV)	$E$ (MeV)	$\Gamma_{\text{damp}}$ (MeV)	$\Gamma_{\text{diss}}$ (MeV)
170	523.975	1481.42	1024.23	-565.725	29.7602	3.47212
180	543.693	1480.27	1011.22	-553.400	30.3093	4.80572
190	563.435	1479.23	999.108	-541.881	30.6542	6.41841
200	583.179	1478.31	987.805	-531.082	30.7867	8.31872
210	602.909	1477.51	977.242	-520.924	30.6996	10.5103
220	622.613	1476.85	967.352	-511.335	30.3857	12.9928
230	642.283	1476.32	958.076	-502.250	29.8393	15.7625
240	661.913	1475.94	949.362	-493.610	29.0547	18.8132
250	681.500	1475.70	941.159	-485.358	28.0267	22.1372

Table B.2: Data on the  $\Upsilon(1S)$  from the potential model using the potential (3.8).

$T$ (MeV)	$m_D$ (MeV)	$\langle 1/r \rangle$ (MeV)	$\langle  V_{\text{eff}}  \rangle$ (MeV)	$E$ (MeV)	$\Gamma_{\text{damp}}$ (MeV)	$\Gamma_{\text{diss}}$ (MeV)
170	523.975	1423.23	786.300	-363.855	27.3595	7.78852
180	543.693	1417.62	765.991	-346.832	30.6275	10.3411

Continued on next page

Table B.2 – continued from previous page

$T$ (MeV)	$m_D$ (MeV)	$\langle 1/r \rangle$ (MeV)	$\langle  V_{\text{eff}}  \rangle$ (MeV)	$E$ (MeV)	$\Gamma_{\text{damp}}$ (MeV)	$\Gamma_{\text{diss}}$ (MeV)
190	563.435	1411.93	746.685	-330.814	34.1089	13.3121
200	583.179	1406.19	728.314	-315.723	37.8050	16.6998
210	602.909	1400.40	710.809	-301.483	41.7172	20.4984
220	622.613	1394.57	694.109	-288.025	45.8468	24.7002
230	642.283	1388.71	678.158	-275.285	50.1946	29.2969
240	661.913	1382.82	662.904	-263.205	54.7616	34.2802
250	681.500	1376.90	648.300	-251.731	59.5484	39.6421
260	701.039	1370.97	634.306	-240.813	64.5555	45.3762
270	720.529	1365.03	620.882	-230.408	69.7830	51.4775
280	739.969	1359.09	607.998	-220.476	75.2311	57.9422
290	759.358	1353.14	595.622	-210.979	80.8994	64.7684
300	778.696	1347.21	583.728	-201.884	86.7876	71.9559
310	797.982	1341.28	572.292	-193.160	92.8948	79.5062
320	817.217	1335.37	561.294	-184.779	99.2201	87.4222
330	836.401	1329.48	550.716	-176.716	105.762	95.7084
340	855.535	1323.62	540.539	-168.946	112.520	104.370
350	874.620	1317.78	530.751	-161.448	119.492	113.415
360	893.656	1311.99	521.337	-154.203	126.676	122.851
370	912.644	1306.23	512.287	-147.191	134.070	132.686
380	931.584	1300.51	503.589	-140.396	141.672	142.929
390	950.478	1294.84	495.236	-133.802	149.479	153.589
400	969.327	1289.22	487.218	-127.395	157.489	164.675
410	988.131	1283.65	479.530	-121.162	165.700	176.194
420	1006.89	1278.14	472.164	-115.090	174.109	188.154
430	1025.61	1272.68	465.116	-109.168	182.712	200.559
440	1044.28	1267.28	458.381	-103.387	191.507	213.410
450	1062.92	1261.93	451.955	-97.7352	200.492	226.708
460	1081.51	1256.65	445.833	-92.2048	209.662	240.448
470	1100.06	1251.44	440.014	-86.7876	219.016	254.620
480	1118.58	1246.28	434.495	-81.4761	228.549	269.210
490	1137.05	1241.19	429.273	-76.2633	238.260	284.196
500	1155.49	1236.16	424.346	-71.1426	248.145	299.550
510	1173.89	1231.19	419.713	-66.1088	258.202	315.238
520	1192.26	1226.29	415.373	-61.1559	268.426	331.214
530	1210.59	1221.45	411.324	-56.2790	278.816	347.426
540	1228.89	1216.67	407.564	-51.4734	289.369	363.812
550	1247.15	1211.95	404.094	-46.7348	300.082	380.299
560	1265.38	1207.30	400.911	-42.0593	310.952	396.811
570	1283.58	1202.70	398.016	-37.4432	321.977	413.256
580	1301.74	1198.17	395.405	-32.8831	333.153	429.541
590	1319.87	1193.69	393.080	-28.3761	344.480	445.563
600	1337.97	1189.27	391.038	-23.9186	355.953	461.219
610	1356.04	1184.91	389.277	-19.5084	367.571	476.403
620	1374.09	1180.60	387.796	-15.1429	379.332	491.009
630	1392.10	1176.35	386.593	-10.8195	391.233	504.934

Continued on next page

Table B.2 – continued from previous page

$T$ (MeV)	$m_D$ (MeV)	$\langle 1/r \rangle$ (MeV)	$\langle  V_{\text{eff}}  \rangle$ (MeV)	$E$ (MeV)	$\Gamma_{\text{damp}}$ (MeV)	$\Gamma_{\text{diss}}$ (MeV)
640	1410.08	1172.14	385.668	-6.53661	403.273	518.085
650	1428.04	1167.99	385.016	-2.29187	415.448	530.375

Table B.3: Data on the  $\chi_b(1P)$  from the potential model using the potential (3.8).

$T$ (MeV)	$m_D$ (MeV)	$\langle 1/r \rangle$ (MeV)	$\langle  V_{\text{eff}}  \rangle$ (MeV)	$E$ (MeV)	$\Gamma_{\text{damp}}$ (MeV)	$\Gamma_{\text{diss}}$ (MeV)
170	523.975	634.428	469.571	-127.343	112.291	54.3876
180	543.693	628.870	450.575	-112.124	126.209	67.6851
190	563.435	623.383	433.043	-97.7730	141.074	82.9315
200	583.179	617.996	416.954	-84.1807	156.875	100.354
210	602.909	612.731	402.288	-71.2430	173.595	120.206
220	622.613	607.606	389.031	-58.8663	191.216	142.742
230	642.283	602.635	377.172	-46.9671	209.712	168.170
240	661.913	597.827	366.706	-35.4732	229.058	196.583
250	681.500	593.188	357.628	-24.3223	249.228	227.860
260	701.039	588.719	349.935	-13.4612	270.191	261.542
270	720.529	584.420	343.624	-2.84475	291.923	296.719

Table B.4: Data on the  $\Upsilon(2S)$  from the potential model using the potential (3.8).

$T$ (MeV)	$m_D$ (MeV)	$\langle 1/r \rangle$ (MeV)	$\langle  V_{\text{eff}}  \rangle$ (MeV)	$E$ (MeV)	$\Gamma_{\text{damp}}$ (MeV)	$\Gamma_{\text{diss}}$ (MeV)
170	523.975	628.734	472.651	-134.978	137.402	75.3499
180	543.693	622.904	456.350	-122.576	153.337	88.8035
190	563.435	617.232	441.484	-110.968	170.189	103.064
200	583.179	611.731	428.018	-100.057	187.937	118.099
210	602.909	606.409	415.927	-89.7545	206.558	133.856
220	622.613	601.271	405.185	-79.9808	226.028	150.231
230	642.283	596.319	395.776	-70.6679	246.324	167.051
240	661.913	591.552	387.680	-61.7541	267.419	184.051
250	681.500	586.966	380.887	-53.1884	289.289	200.867
260	701.039	582.555	375.382	-44.9259	311.910	217.036
270	720.529	578.314	371.153	-36.9290	335.258	232.033
280	739.969	574.236	368.183	-29.1648	359.310	245.310
290	759.358	570.311	366.455	-21.6061	384.045	256.379
300	778.696	566.533	365.944	-14.2291	409.443	264.872
310	797.982	562.893	366.625	-7.01377	435.484	270.608

Table B.5: Data on the  $\chi_b(2P)$  from the potential model using the potential (3.8).

$T$ (MeV)	$m_D$ (MeV)	$\langle 1/r \rangle$ (MeV)	$\langle  V_{\text{eff}}  \rangle$ (MeV)	$E$ (MeV)	$\Gamma_{\text{damp}}$ (MeV)	$\Gamma_{\text{diss}}$ (MeV)
170	523.975	428.004	436.133	-47.0506	325.335	120.844
180	543.693	424.554	428.790	-33.5541	362.547	136.431
190	563.435	421.287	424.080	-20.3909	401.642	150.776
200	583.179	418.195	422.015	-7.48848	442.545	163.282

Table B.6: Data on the  $\Upsilon(3S)$  from the potential model using the potential (3.8).

$T$ (MeV)	$m_D$ (MeV)	$\langle 1/r \rangle$ (MeV)	$\langle  V_{\text{eff}}  \rangle$ (MeV)	$E$ (MeV)	$\Gamma_{\text{damp}}$ (MeV)	$\Gamma_{\text{diss}}$ (MeV)
170	523.975	426.747	449.144	-63.4477	343.634	115.549
180	543.693	423.397	443.030	-51.7507	381.608	127.626
190	563.435	420.228	439.404	-40.4093	421.388	138.457
200	583.179	417.230	438.273	-29.3603	462.903	147.718
210	602.909	414.393	439.623	-18.5499	506.088	155.203
220	622.613	411.707	443.415	-7.93449	550.885	160.853

Table B.7: Data on the  $\chi_b(3P)$  from the potential model using the potential (3.8).

$T$ (MeV)	$m_D$ (MeV)	$\langle 1/r \rangle$ (MeV)	$\langle  V_{\text{eff}}  \rangle$ (MeV)	$E$ (MeV)	$\Gamma_{\text{damp}}$ (MeV)	$\Gamma_{\text{diss}}$ (MeV)
170	523.975	353.132	546.879	-8.87933	633.336	114.209

## B.2 Suppression factors and double ratios

We present data on the suppression factors  $R_{AA}(\Upsilon(nS))$  and double ratios  $\frac{[\Upsilon(nS)/\Upsilon(1S)]_{\text{PbPb}}}{[\Upsilon(nS)/\Upsilon(1S)]_{pp}}$  as  $p_T$ -averaged functions of centrality and centrality-averaged functions of  $p_T$ . Minimum bias results are shown in tabs. 6.1 and 6.2.

Table B.8: Suppression factors  $R_{AA}(\Upsilon(nS))$  and double ratios  $\frac{[\Upsilon(nS)/\Upsilon(1S)]_{\text{PbPb}}}{[\Upsilon(nS)/\Upsilon(1S)]_{pp}}$  as functions of centrality using IC1,  $T_0 = 550$  MeV,  $\tau_{nl} = 0.1$  fm/ $c$ , averaged over  $p_T$ .

Centrality bin	$R_{AA}(\Upsilon(1S))$	$R_{AA}(\Upsilon(2S))$	$R_{AA}(\Upsilon(3S))$	$\frac{[\Upsilon(2S)]_{\text{PbPb}}}{[\Upsilon(1S)]_{pp}}$	$\frac{[\Upsilon(3S)]_{\text{PbPb}}}{[\Upsilon(1S)]_{pp}}$
0 - 5%	0.454	0.305	0.215	0.669	0.467

Continued on next page

Table B.8 – continued from previous page

Centrality bin	$R_{AA}(\Upsilon(1S))$	$R_{AA}(\Upsilon(2S))$	$R_{AA}(\Upsilon(3S))$	$\frac{[\Upsilon(2S)]_{PbPb}}{[\Upsilon(1S)]_{pp}}$	$\frac{[\Upsilon(3S)]_{PbPb}}{[\Upsilon(1S)]_{pp}}$
5 - 10%	0.501	0.356	0.254	0.708	0.502
10 - 20%	0.580	0.450	0.325	0.775	0.558
20 - 30%	0.718	0.633	0.473	0.882	0.659
30 - 40%	0.881	0.840	0.716	0.955	0.818
40 - 50%	0.986	0.981	0.958	0.996	0.973
50 - 100%	1	1	1	1	1

Table B.9: Suppression factors  $R_{AA}(\Upsilon(nS))$  and double ratios  $\frac{[\Upsilon(nS)/\Upsilon(1S)]_{PbPb}}{[\Upsilon(nS)/\Upsilon(1S)]_{pp}}$  as functions of centrality using IC1,  $T_0 = 550$  MeV,  $\tau_{nl} = 0.5$  fm/c, averaged over  $p_T$ .

Centrality bin	$R_{AA}(\Upsilon(1S))$	$R_{AA}(\Upsilon(2S))$	$R_{AA}(\Upsilon(3S))$	$\frac{[\Upsilon(2S)]_{PbPb}}{[\Upsilon(1S)]_{pp}}$	$\frac{[\Upsilon(3S)]_{PbPb}}{[\Upsilon(1S)]_{pp}}$
0 - 5%	0.714	0.613	0.513	0.856	0.715
5 - 10%	0.773	0.685	0.586	0.887	0.757
10 - 20%	0.858	0.799	0.714	0.933	0.833
20 - 30%	0.961	0.946	0.904	0.985	0.944
30 - 40%	1	0.999	0.998	1	0.999
40 - 50%	1	1	1	1	1
50 - 100%	1	1	1	1	1

Table B.10: Suppression factors  $R_{AA}(\Upsilon(nS))$  and double ratios  $\frac{[\Upsilon(nS)/\Upsilon(1S)]_{PbPb}}{[\Upsilon(nS)/\Upsilon(1S)]_{pp}}$  as functions of centrality using IC1,  $T_0 = 650$  MeV,  $\tau_{nl} = 0.1$  fm/c, averaged over  $p_T$ .

Centrality bin	$R_{AA}(\Upsilon(1S))$	$R_{AA}(\Upsilon(2S))$	$R_{AA}(\Upsilon(3S))$	$\frac{[\Upsilon(2S)]_{PbPb}}{[\Upsilon(1S)]_{pp}}$	$\frac{[\Upsilon(3S)]_{PbPb}}{[\Upsilon(1S)]_{pp}}$
0 - 5%	0.375	0.235	0.168	0.623	0.441
5 - 10%	0.421	0.276	0.201	0.654	0.471
10 - 20%	0.496	0.353	0.259	0.711	0.519
20 - 30%	0.625	0.508	0.379	0.813	0.605
30 - 40%	0.800	0.739	0.588	0.925	0.738
40 - 50%	0.958	0.943	0.890	0.985	0.932
50 - 100%	1	1	1	1	1

Table B.11: Suppression factors  $R_{AA}(\Upsilon(nS))$  and double ratios  $\frac{[\Upsilon(nS)/\Upsilon(1S)]_{\text{PbPb}}}{[\Upsilon(nS)/\Upsilon(1S)]_{pp}}$  as functions of centrality using IC1,  $T_0 = 650$  MeV,  $\tau_{nl} = 0.5$  fm/ $c$ , averaged over  $p_T$ .

Centrality bin	$R_{AA}(\Upsilon(1S))$	$R_{AA}(\Upsilon(2S))$	$R_{AA}(\Upsilon(3S))$	$\frac{[\Upsilon(2S)]_{\text{PbPb}}}{[\Upsilon(1S)]_{pp}}$	$\frac{[\Upsilon(3S)]_{\text{PbPb}}}{[\Upsilon(1S)]_{pp}}$
0 - 5%	0.605	0.488	0.400	0.803	0.654
5 - 10%	0.665	0.557	0.462	0.835	0.689
10 - 20%	0.759	0.671	0.574	0.884	0.753
20 - 30%	0.893	0.849	0.776	0.952	0.871
30 - 40%	0.987	0.983	0.965	0.995	0.978
40 - 50%	1	1	1	1	1
50 - 100%	1	1	1	1	1

Table B.12: Suppression factors  $R_{AA}(\Upsilon(nS))$  and double ratios  $\frac{[\Upsilon(nS)/\Upsilon(1S)]_{\text{PbPb}}}{[\Upsilon(nS)/\Upsilon(1S)]_{pp}}$  as functions of centrality using IC2,  $T_0 = 550$  MeV,  $\tau_{nl} = 0.1$  fm/ $c$ , averaged over  $p_T$ .

Centrality bin	$R_{AA}(\Upsilon(1S))$	$R_{AA}(\Upsilon(2S))$	$R_{AA}(\Upsilon(3S))$	$\frac{[\Upsilon(2S)]_{\text{PbPb}}}{[\Upsilon(1S)]_{pp}}$	$\frac{[\Upsilon(3S)]_{\text{PbPb}}}{[\Upsilon(1S)]_{pp}}$
0 - 5%	0.213	0.0386	0.012	0.16	0.0517
5 - 10%	0.226	0.0457	0.0152	0.182	0.0627
10 - 20%	0.247	0.0583	0.0206	0.215	0.0785
20 - 30%	0.283	0.0841	0.0314	0.277	0.106
30 - 40%	0.332	0.129	0.0506	0.372	0.147
40 - 50%	0.404	0.214	0.0882	0.518	0.212
50 - 100%	0.609	0.492	0.281	0.806	0.459

Table B.13: Suppression factors  $R_{AA}(\Upsilon(nS))$  and double ratios  $\frac{[\Upsilon(nS)/\Upsilon(1S)]_{\text{PbPb}}}{[\Upsilon(nS)/\Upsilon(1S)]_{pp}}$  as functions of centrality using IC2,  $T_0 = 550$  MeV,  $\tau_{nl} = 0.5$  fm/ $c$ , averaged over  $p_T$ .

Centrality bin	$R_{AA}(\Upsilon(1S))$	$R_{AA}(\Upsilon(2S))$	$R_{AA}(\Upsilon(3S))$	$\frac{[\Upsilon(2S)]_{\text{PbPb}}}{[\Upsilon(1S)]_{pp}}$	$\frac{[\Upsilon(3S)]_{\text{PbPb}}}{[\Upsilon(1S)]_{pp}}$
0 - 5%	0.422	0.242	0.135	0.546	0.292
5 - 10%	0.448	0.269	0.153	0.577	0.317
10 - 20%	0.492	0.317	0.188	0.625	0.359
20 - 30%	0.567	0.403	0.258	0.698	0.436
30 - 40%	0.663	0.526	0.371	0.786	0.546
40 - 50%	0.782	0.691	0.551	0.882	0.700
50 - 100%	0.943	0.922	0.861	0.977	0.915

Table B.14: Suppression factors  $R_{AA}(\Upsilon(nS))$  and double ratios  $\frac{[\Upsilon(nS)/\Upsilon(1S)]_{\text{PbPb}}}{[\Upsilon(nS)/\Upsilon(1S)]_{pp}}$  as functions of centrality using IC2,  $T_0 = 650$  MeV,  $\tau_{nl} = 0.1$  fm/c, averaged over  $p_T$ .

Centrality bin	$R_{AA}(\Upsilon(1S))$	$R_{AA}(\Upsilon(2S))$	$R_{AA}(\Upsilon(3S))$	$\frac{[\Upsilon(2S)]_{\text{PbPb}}}{[\Upsilon(2S)]_{pp}}$	$\frac{[\Upsilon(3S)]_{\text{PbPb}}}{[\Upsilon(3S)]_{pp}}$
0 - 5%	0.145	0.0185	0.00596	0.108	0.0371
5 - 10%	0.157	0.0225	0.00792	0.125	0.0464
10 - 20%	0.176	0.0294	0.0110	0.149	0.0580
20 - 30%	0.209	0.0434	0.0172	0.190	0.0772
30 - 40%	0.253	0.0686	0.0283	0.253	0.107
40 - 50%	0.315	0.118	0.0507	0.357	0.155
50 - 100%	0.494	0.336	0.186	0.676	0.371

Table B.15: Suppression factors  $R_{AA}(\Upsilon(nS))$  and double ratios  $\frac{[\Upsilon(nS)/\Upsilon(1S)]_{\text{PbPb}}}{[\Upsilon(nS)/\Upsilon(1S)]_{pp}}$  as functions of centrality using IC2,  $T_0 = 650$  MeV,  $\tau_{nl} = 0.5$  fm/c, averaged over  $p_T$ .

Centrality bin	$R_{AA}(\Upsilon(1S))$	$R_{AA}(\Upsilon(2S))$	$R_{AA}(\Upsilon(3S))$	$\frac{[\Upsilon(2S)]_{\text{PbPb}}}{[\Upsilon(2S)]_{pp}}$	$\frac{[\Upsilon(3S)]_{\text{PbPb}}}{[\Upsilon(3S)]_{pp}}$
0 - 5%	0.295	0.131	0.0683	0.406	0.203
5 - 10%	0.316	0.148	0.079	0.433	0.221
10 - 20%	0.352	0.180	0.0985	0.479	0.252
20 - 30%	0.416	0.242	0.138	0.556	0.307
30 - 40%	0.504	0.338	0.206	0.652	0.389
40 - 50%	0.625	0.479	0.328	0.759	0.511
50 - 100%	0.84	0.774	0.667	0.922	0.794

Table B.16: Suppression factors  $R_{AA}(\Upsilon(nS))$  and double ratios  $\frac{[\Upsilon(nS)/\Upsilon(1S)]_{\text{PbPb}}}{[\Upsilon(nS)/\Upsilon(1S)]_{pp}}$  as functions of  $p_T$  using IC1,  $T_0 = 550$  MeV,  $\tau_{nl} = 0.1$  fm/c, averaged over  $p_T$ .

$p_T$ (GeV)	$R_{AA}(\Upsilon(1S))$	$R_{AA}(\Upsilon(2S))$	$R_{AA}(\Upsilon(3S))$	$\frac{[\Upsilon(2S)]_{\text{PbPb}}}{[\Upsilon(2S)]_{pp}}$	$\frac{[\Upsilon(3S)]_{\text{PbPb}}}{[\Upsilon(3S)]_{pp}}$
0	0.547	0.423	0.319	0.774	0.584
2	0.561	0.437	0.330	0.779	0.588
4	0.585	0.464	0.349	0.793	0.596
6	0.617	0.501	0.377	0.812	0.610
8	0.655	0.546	0.411	0.834	0.627
10	0.695	0.597	0.451	0.860	0.649
12	0.735	0.651	0.493	0.886	0.671
14	0.775	0.705	0.541	0.909	0.699
16	0.813	0.755	0.590	0.929	0.726
18	0.847	0.799	0.639	0.943	0.755
20	0.878	0.836	0.691	0.952	0.787

Continued on next page

Table B.16 – continued from previous page

$p_T$ (GeV)	$R_{AA}(\Upsilon(1S))$	$R_{AA}(\Upsilon(2S))$	$R_{AA}(\Upsilon(3S))$	$\frac{[\Upsilon(2S)]_{PbPb}}{[\Upsilon(1S)]_{pp}}$	$\frac{[\Upsilon(3S)]_{PbPb}}{[\Upsilon(1S)]_{pp}}$
22	0.902	0.865	0.740	0.959	0.820
24	0.923	0.894	0.787	0.968	0.852
26	0.940	0.918	0.832	0.977	0.884
28	0.955	0.940	0.872	0.984	0.912

Table B.17: Suppression factors  $R_{AA}(\Upsilon(nS))$  and double ratios  $\frac{[\Upsilon(nS)/\Upsilon(1S)]_{PbPb}}{[\Upsilon(nS)/\Upsilon(1S)]_{pp}}$  as functions of  $p_T$  using IC1,  $T_0 = 550$  MeV,  $\tau_{nl} = 0.5$  fm/c, averaged over  $p_T$ .

$p_T$ (GeV)	$R_{AA}(\Upsilon(1S))$	$R_{AA}(\Upsilon(2S))$	$R_{AA}(\Upsilon(3S))$	$\frac{[\Upsilon(2S)]_{PbPb}}{[\Upsilon(1S)]_{pp}}$	$\frac{[\Upsilon(3S)]_{PbPb}}{[\Upsilon(1S)]_{pp}}$
0	0.778	0.699	0.611	0.899	0.786
2	0.798	0.724	0.637	0.907	0.797
4	0.830	0.766	0.677	0.922	0.816
6	0.867	0.813	0.730	0.939	0.843
8	0.902	0.862	0.788	0.955	0.873
10	0.934	0.906	0.843	0.970	0.903
12	0.959	0.942	0.895	0.983	0.933
14	0.978	0.970	0.937	0.992	0.958
16	0.990	0.987	0.968	0.997	0.977
18	0.997	0.995	0.987	0.999	0.991
20	0.999	0.999	0.998	1	0.998
22	1	1	1	1	1
24	1	1	1	1	1
26	1	1	1	1	1
28	1	1	1	1	1

Table B.18: Suppression factors  $R_{AA}(\Upsilon(nS))$  and double ratios  $\frac{[\Upsilon(nS)/\Upsilon(1S)]_{PbPb}}{[\Upsilon(nS)/\Upsilon(1S)]_{pp}}$  as functions of  $p_T$  using IC1,  $T_0 = 650$  MeV,  $\tau_{nl} = 0.1$  fm/c, averaged over  $p_T$ .

$p_T$ (GeV)	$R_{AA}(\Upsilon(1S))$	$R_{AA}(\Upsilon(2S))$	$R_{AA}(\Upsilon(3S))$	$\frac{[\Upsilon(2S)]_{PbPb}}{[\Upsilon(1S)]_{pp}}$	$\frac{[\Upsilon(3S)]_{PbPb}}{[\Upsilon(1S)]_{pp}}$
0	0.469	0.346	0.263	0.738	0.561
2	0.483	0.357	0.272	0.740	0.563
4	0.508	0.381	0.288	0.750	0.567
6	0.539	0.412	0.311	0.764	0.576
8	0.576	0.450	0.339	0.782	0.588
10	0.614	0.494	0.372	0.805	0.606
12	0.653	0.542	0.407	0.830	0.623
14	0.691	0.592	0.446	0.857	0.645
16	0.729	0.642	0.487	0.881	0.668

Continued on next page

Table B.18 – continued from previous page

$p_T$ (GeV)	$R_{AA}(\Upsilon(1S))$	$R_{AA}(\Upsilon(2S))$	$R_{AA}(\Upsilon(3S))$	$\frac{[\Upsilon(2S)]_{PbPb}}{[\Upsilon(1S)]_{pp}}$	$\frac{[\Upsilon(3S)]_{PbPb}}{[\Upsilon(1S)]_{pp}}$
18	0.765	0.691	0.528	0.903	0.691
20	0.801	0.739	0.572	0.923	0.715
22	0.832	0.780	0.616	0.937	0.741
24	0.861	0.816	0.660	0.948	0.766
26	0.886	0.845	0.705	0.954	0.795
28	0.907	0.871	0.747	0.961	0.824

Table B.19: Suppression factors  $R_{AA}(\Upsilon(nS))$  and double ratios  $\frac{[\Upsilon(nS)/\Upsilon(1S)]_{PbPb}}{[\Upsilon(nS)/\Upsilon(1S)]_{pp}}$  as functions of  $p_T$  using IC1,  $T_0 = 650$  MeV,  $\tau_{nl} = 0.5$  fm/c, averaged over  $p_T$ .

$p_T$ (GeV)	$R_{AA}(\Upsilon(1S))$	$R_{AA}(\Upsilon(2S))$	$R_{AA}(\Upsilon(3S))$	$\frac{[\Upsilon(2S)]_{PbPb}}{[\Upsilon(1S)]_{pp}}$	$\frac{[\Upsilon(3S)]_{PbPb}}{[\Upsilon(1S)]_{pp}}$
0	0.679	0.583	0.501	0.858	0.737
2	0.705	0.612	0.527	0.869	0.747
4	0.742	0.657	0.565	0.885	0.762
6	0.785	0.710	0.616	0.904	0.785
8	0.829	0.765	0.673	0.923	0.811
10	0.871	0.818	0.731	0.940	0.839
12	0.906	0.867	0.789	0.956	0.871
14	0.935	0.908	0.845	0.971	0.904
16	0.959	0.942	0.894	0.982	0.932
18	0.976	0.966	0.932	0.990	0.955
20	0.988	0.983	0.961	0.996	0.973
22	0.995	0.993	0.981	0.998	0.986
24	0.998	0.998	0.993	1	0.995
26	1	1	0.999	1	0.999
28	1	1	1	1	1

Table B.20: Suppression factors  $R_{AA}(\Upsilon(nS))$  and double ratios  $\frac{[\Upsilon(nS)/\Upsilon(1S)]_{PbPb}}{[\Upsilon(nS)/\Upsilon(1S)]_{pp}}$  as functions of  $p_T$  using IC2,  $T_0 = 550$  MeV,  $\tau_{nl} = 0.1$  fm/c, averaged over  $p_T$ .

$p_T$ (GeV)	$R_{AA}(\Upsilon(1S))$	$R_{AA}(\Upsilon(2S))$	$R_{AA}(\Upsilon(3S))$	$\frac{[\Upsilon(2S)]_{PbPb}}{[\Upsilon(1S)]_{pp}}$	$\frac{[\Upsilon(3S)]_{PbPb}}{[\Upsilon(1S)]_{pp}}$
0	0.211	0.0464	0.0192	0.220	0.0908
2	0.223	0.0506	0.0206	0.227	0.0925
4	0.246	0.0606	0.0237	0.247	0.0965
6	0.276	0.0772	0.0290	0.280	0.105
8	0.311	0.103	0.0365	0.329	0.117
10	0.350	0.140	0.0475	0.400	0.136
12	0.393	0.192	0.0617	0.489	0.157

Continued on next page

Table B.20 – continued from previous page

$p_T$ (GeV)	$R_{AA}(\Upsilon(1S))$	$R_{AA}(\Upsilon(2S))$	$R_{AA}(\Upsilon(3S))$	$\frac{[\Upsilon(2S)]_{PbPb}}{[\Upsilon(1S)]_{pp}}$	$\frac{[\Upsilon(3S)]_{PbPb}}{[\Upsilon(1S)]_{pp}}$
14	0.443	0.264	0.0823	0.595	0.186
16	0.500	0.354	0.109	0.707	0.217
18	0.566	0.454	0.144	0.803	0.254
20	0.633	0.527	0.189	0.833	0.298
22	0.695	0.581	0.246	0.836	0.354
24	0.742	0.636	0.316	0.857	0.425
26	0.779	0.690	0.403	0.886	0.517
28	0.815	0.743	0.502	0.912	0.616

Table B.21: Suppression factors  $R_{AA}(\Upsilon(nS))$  and double ratios  $\frac{[\Upsilon(nS)/\Upsilon(1S)]_{PbPb}}{[\Upsilon(nS)/\Upsilon(1S)]_{pp}}$  as functions of  $p_T$  using IC2,  $T_0 = 550$  MeV,  $\tau_{nl} = 0.5$  fm/c, averaged over  $p_T$ .

$p_T$ (GeV)	$R_{AA}(\Upsilon(1S))$	$R_{AA}(\Upsilon(2S))$	$R_{AA}(\Upsilon(3S))$	$\frac{[\Upsilon(2S)]_{PbPb}}{[\Upsilon(1S)]_{pp}}$	$\frac{[\Upsilon(3S)]_{PbPb}}{[\Upsilon(1S)]_{pp}}$
0	0.402	0.224	0.119	0.556	0.296
2	0.432	0.253	0.136	0.586	0.315
4	0.483	0.308	0.168	0.638	0.348
6	0.553	0.385	0.222	0.696	0.402
8	0.632	0.480	0.299	0.760	0.473
10	0.710	0.585	0.398	0.825	0.560
12	0.788	0.697	0.521	0.884	0.661
14	0.861	0.804	0.653	0.934	0.758
16	0.923	0.894	0.770	0.968	0.835
18	0.963	0.951	0.874	0.988	0.907
20	0.990	0.987	0.960	0.997	0.970
22	1	1	1	1	1
24	1	1	1	1	1
26	1	1	1	1	1
28	1	1	1	1	1

Table B.22: Suppression factors  $R_{AA}(\Upsilon(nS))$  and double ratios  $\frac{[\Upsilon(nS)/\Upsilon(1S)]_{PbPb}}{[\Upsilon(nS)/\Upsilon(1S)]_{pp}}$  as functions of  $p_T$  using IC2,  $T_0 = 650$  MeV,  $\tau_{nl} = 0.1$  fm/c, averaged over  $p_T$ .

$p_T$ (GeV)	$R_{AA}(\Upsilon(1S))$	$R_{AA}(\Upsilon(2S))$	$R_{AA}(\Upsilon(3S))$	$\frac{[\Upsilon(2S)]_{PbPb}}{[\Upsilon(1S)]_{pp}}$	$\frac{[\Upsilon(3S)]_{PbPb}}{[\Upsilon(1S)]_{pp}}$
0	0.141	0.0257	0.0116	0.183	0.0822
2	0.153	0.0280	0.0124	0.183	0.0813
4	0.175	0.0332	0.0143	0.189	0.0813
6	0.204	0.0415	0.0172	0.203	0.0842
8	0.238	0.0539	0.0214	0.226	0.0898

Continued on next page

Table B.22 – continued from previous page

$p_T$ (GeV)	$R_{AA}(\Upsilon(1S))$	$R_{AA}(\Upsilon(2S))$	$R_{AA}(\Upsilon(3S))$	$\frac{[\Upsilon(2S)]_{PbPb}}{[\Upsilon(1S)]_{pp}}$	$\frac{[\Upsilon(3S)]_{PbPb}}{[\Upsilon(1S)]_{pp}}$
10	0.274	0.0722	0.0273	0.264	0.0999
12	0.310	0.0979	0.0347	0.316	0.112
14	0.347	0.133	0.0452	0.385	0.130
16	0.386	0.180	0.0583	0.466	0.151
18	0.429	0.240	0.0751	0.559	0.175
20	0.479	0.318	0.097	0.663	0.203
22	0.533	0.403	0.125	0.757	0.234
24	0.594	0.490	0.159	0.825	0.268
26	0.651	0.543	0.202	0.834	0.310
28	0.704	0.590	0.253	0.838	0.359

Table B.23: Suppression factors  $R_{AA}(\Upsilon(nS))$  and double ratios  $\frac{[\Upsilon(nS)/\Upsilon(1S)]_{PbPb}}{[\Upsilon(nS)/\Upsilon(1S)]_{pp}}$  as functions of  $p_T$  using IC2,  $T_0 = 650$  MeV,  $\tau_{nl} = 0.5$  fm/c, averaged over  $p_T$ .

$p_T$ (GeV)	$R_{AA}(\Upsilon(1S))$	$R_{AA}(\Upsilon(2S))$	$R_{AA}(\Upsilon(3S))$	$\frac{[\Upsilon(2S)]_{PbPb}}{[\Upsilon(1S)]_{pp}}$	$\frac{[\Upsilon(3S)]_{PbPb}}{[\Upsilon(1S)]_{pp}}$
0	0.274	0.117	0.062	0.425	0.226
2	0.301	0.137	0.0717	0.455	0.238
4	0.346	0.175	0.0893	0.506	0.258
6	0.405	0.231	0.119	0.571	0.293
8	0.477	0.305	0.161	0.640	0.338
10	0.556	0.390	0.218	0.702	0.392
12	0.637	0.486	0.295	0.763	0.462
14	0.712	0.588	0.395	0.827	0.554
16	0.782	0.687	0.509	0.879	0.651
18	0.847	0.782	0.627	0.923	0.741
20	0.905	0.867	0.733	0.958	0.810
22	0.948	0.929	0.828	0.980	0.873
24	0.975	0.968	0.909	0.992	0.933
26	0.993	0.992	0.973	0.998	0.980
28	1	1	1	1	1



# Bibliography

- G. Aad et al. (ATLAS Collaboration), *Observation of a New  $\chi_b$  State in Radiative Transitions to  $\Upsilon(1S)$  and  $\Upsilon(2S)$  at ATLAS*, Phys. Rev. Lett. 108, 152001 (2012)
- G. Aad et al. (ATLAS Collaboration), *Observation of a Centrality-Dependent Dijet Asymmetry in Lead-Lead Collisions at  $\sqrt{s_{NN}} = 2.76$  TeV with the ATLAS Detector at the LHC*, Phys. Rev. Lett. 105, 252303 (2010)
- K. Aamodt et al. (ALICE Collaboration), *Higher Harmonic Anisotropic Flow Measurements of Charged Particles in Pb-Pb Collisions at  $\sqrt{s_{NN}} = 2.76$  TeV*, Phys. Rev. Lett. 107, 032301 (2011a)
- K. Aamodt et al. (ALICE Collaboration), *Centrality Dependence of the Charged-Particle Multiplicity Density at Midrapidity in Pb-Pb Collisions at  $\sqrt{s_{NN}} = 2.76$  TeV*, Phys. Rev. Lett. 106, 032301 (2011b)
- K. Aamodt et al. (ALICE Collaboration), *Charged-Particle Multiplicity Density at Midrapidity in Central Pb-Pb Collisions at  $\sqrt{s_{NN}} = 2.76$  TeV*, Phys. Rev. Lett. 105, 252301 (2010a)
- K. Aamodt et al. (ALICE Collaboration), *Elliptic flow of charged particles in Pb-Pb collisions at 2.76 TeV*, Phys. Rev. Lett. 105, 252302 (2010b)
- K. Aamodt et al. (ALICE Collaboration), *Two-pion Bose-Einstein correlations in central Pb-Pb collisions at  $\sqrt{s_{NN}} = 2.76$  TeV*, Phys. Lett. B 696, 328 (2011)
- F. Abe et al. (CDF Collaboration), *Evidence for top quark production in  $p\bar{p}$  collisions at  $\sqrt{s} = 1.8$  TeV*, Phys. Rev. D 50, 2966 (1994)
- M. Abramowitz and I. A. Stegun, *Handbook of mathematical functions with formulas, graphs and mathematical tables*, Dover Publications, New York (1968)

- M. C. Abreu et al. (NA50 Collaboration), *Evidence for deconfinement of quarks and gluons from the  $J/\psi$  suppression pattern measured in Pb-Pb collisions at the CERN-SPS*, Phys. Lett. B 477, 28 (2000)
- J. Adams et al. (STAR Collaboration), *Experimental and theoretical challenges in the search for the quark gluon plasma: The STAR Collaboration's critical assessment of the evidence from RHIC collisions*, Nucl. Phys. A 757, 102 (2005)
- K. Adcox et al. (PHENIX Collaboration), *Formation of dense partonic matter in relativistic nucleus-nucleus collisions at RHIC: Experimental evaluation by the PHENIX collaboration*, Nucl. Phys. A 757, 184 (2005)
- T. Affolder et al. (CDF Collaboration), *Production of  $\Upsilon(1S)$  Mesons from  $\chi_b$  Decays in  $p\bar{p}$  Collisions at  $\sqrt{s} = 1.8$  TeV*, Phys. Rev. Lett. 84, 2094 (2000)
- J. Alford and M. Strickland, *Charmonia and Bottomonia in a Magnetic Field*, Phys. Rev. D 88, 105017 (2013)
- I. Arsene et al. (BRAHMS Collaboration), *Quark gluon plasma and color glass condensate at RHIC? The Perspective from the BRAHMS experiment*, Nucl. Phys. A 757, 1 (2005)
- E. T. Atomssa et al. (PHENIX Collaboration),  *$J/\psi$  Elliptic Flow, High  $p_T$  Suppression and  $\Upsilon$  Measurements in A+A Collisions by the PHENIX Experiment.*, Nucl. Phys. A 830, 331 (2009)
- J. J. Aubert et al. (E598 Collaboration), *Experimental Observation of a Heavy Particle J*, Phys. Rev. Lett. 33, 1404 (1974)
- J.-E. Augustin et al. (SLAC-SP-017 Collaboration), *Discovery of a Narrow Resonance in  $e^+e^-$  Annihilation*, Phys. Rev. Lett. 33, 1406 (1974)
- B. Back et al. (PHOBOS Collaboration), *The PHOBOS perspective on discoveries at RHIC*, Nucl. Phys. A 757, 28 (2005)
- B. B. Back et al. (PHOBOS Collaboration), *Collision geometry scaling of Au+Au pseudorapidity density from  $\sqrt{s_{NN}} = 19.6$  to 200 GeV*, Phys. Rev. C 70, 021902 (2004)
- A. Bazavov et al. (HotQCD Collaboration), *The chiral and deconfinement aspects of the QCD transition*, Phys. Rev. D 85, 054503 (2012)

- A. Beraudo, J. P. Blaizot, P. Faccioli and G. Garberoglio, *A path integral for heavy quarks in a hot plasma*, Nucl. Phys. A 846, 104 (2010)
- A. Beraudo, J. P. Blaizot and C. Ratti, *Real and imaginary-time  $Q\bar{Q}$  correlators in a thermal medium*, Nucl. Phys. A 806, 312 (2008)
- J. Beringer et al. (Particle Data Group), *Review of Particle Physics*, Phys. Rev. D 86, 010001 (2012)
- S. Bethke, *The 2009 world average of  $\alpha_s$* , Eur. Phys. J. C 64, 689 (2009)
- S. Bethke, *World Summary of  $\alpha_s$  (2012)*, Nucl. Phys. B (Proc. Suppl.) 234, 229 (2013)
- G. Bhanot and M. E. Peskin, *Short-distance analysis for heavy-quark systems (II). Applications*, Nucl. Phys. B 156, 391 (1979)
- J. D. Bjorken, *Highly relativistic nucleus-nucleus collisions: The central rapidity region*, Phys. Rev. D 27, 140 (1983)
- J.-P. Blaizot and E. Iancu, *The quark-gluon plasma: collective dynamics and hard thermal loops*, Phys. Rep. 359, 355 (2002)
- G. T. Bodwin, E. Braaten and G. P. Lepage, *Rigorous QCD analysis of inclusive annihilation and production of heavy quarkonium*, Phys. Rev. D 51, 1125 (1995), Erratum-ibid. 55, 5853 (1997)
- E. Braaten, *Introduction to the NRQCD Factorization Approach to Heavy Quarkonium*, arXiv:hep-ph/9702225v1 (1997)
- N. Brambilla, M. A. Escobedo, J. Ghiglieri and A. Vairo, *Thermal width and gluo-dissociation of quarkonium in pNRQCD*, J. High Energy Phys. 12, 116 (2011)
- N. Brambilla, J. Ghiglieri, A. Vairo and P. Petreczky, *Static quark-antiquark pairs at finite temperature*, Phys. Rev. D 78, 014017 (2008)
- P. Braun-Munzinger and J. Stachel, *Charmonium from Statistical Hadronization of Heavy Quarks: A Probe for Deconfinement in the Quark-Gluon Plasma*, Landolt-Börnstein I 23, 424 (2010)
- P. Braun-Munzinger, J. Stachel, J. Wessels and N. Xu, *Thermal equilibration and expansion in nucleus-nucleus collisions at the AGS*, Phys. Lett. B 344, 43 (1995)

- F. Brezinski and G. Wolschin, *Gluodissociation and screening of  $\Upsilon$  states in PbPb collisions at  $\sqrt{s_{NN}} = 2.76$  TeV*, Phys. Lett. B 707, 534 (2012)
- W. E. Caswell and G. P. Lepage, *Effective lagrangians for bound state problems in QED, QCD, and other field theories*, Phys. Lett. B 167, 437 (1986)
- S. Chatrchyan et al. (CMS Collaboration), *Observation and studies of jet quenching in PbPb collisions at  $\sqrt{s_{NN}} = 2.76$  TeV*, Phys. Rev. C 84, 024906 (2011)
- S. Chatrchyan et al. (CMS Collaboration), *Observation of Sequential  $\Upsilon$  Suppression in PbPb Collisions*, Phys. Rev. Lett. 109, 222301 (2012)
- S. Chatrchyan et al. (CMS Collaboration), *Indications of Suppression of Excited  $\Upsilon$  States in Pb-Pb Collisions at  $\sqrt{s_{NN}} = 2.76$  TeV*, Phys. Rev. Lett. 107, 052302 (2011)
- M. Cheng et al. (RBC-Bielefeld), *The Transition temperature in QCD*, Phys. Rev. D 74, 054507 (2006)
- J. C. Collins and M. J. Perry, *Superdense Matter: Neutrons or Asymptotically Free Quarks?*, Phys. Rev. Lett. 34, 1353 (1975)
- R. Courant, K. Friedrichs and H. Lewy, *Über die partiellen Differenzgleichungen der mathematischen Physik*, Math. Ann. 100, 32 (1928)
- F. Daghighian and D. Silverman, *Relativistic formulation of the radiative transitions of charmonium and b-quarkonium*, Phys. Rev. D 36, 3401 (1987)
- H. de Vries, C. W. de Jager and C. de Vries, *Nuclear Charge-Density-Distribution Parameters from Electron Scattering*, At. Data Nucl. Data Tables 36, 495 (1987)
- A. Emerick, X. Zhao and R. Rapp, *Bottomonia in the Quark-Gluon Plasma and their Production at RHIC and LHC*, Eur. Phys. J. A 48, 72 (2012)
- M. A. Escobedo, F. Giannuzzi, M. Mannarelli and J. Soto, *Heavy quarkonium moving in a quark-gluon plasma*, Phys. Rev. D 87, 114005 (2013)
- M. A. Escobedo, J. Soto and M. Mannarelli, *Nonrelativistic bound states in a moving thermal bath*, Phys. Rev. D 84, 016008 (2011)
- L. L. Foldy and S. A. Wouthuysen, *On the Dirac Theory of Spin 1/2 Particles and Its Non-Relativistic Limit*, Phys. Rev. 78, 29 (1950)

- J. Ghiglieri, *Effective Field Theories of QCD for Heavy Quarkonia at Finite Temperature*, Ph.D. Thesis, Technische Universität München (2012)
- L. Grandchamp, S. Lumpkins, D. Sun, H. van Hees and R. Rapp, *Bottomonium production at RHIC and CERN LHC*, Phys. Rev. C 73, 064906 (2006)
- W. Greiner, S. Schramm and E. Stein, *Quantum Chromodynamics, Third Edition*, Springer, Berlin and Heidelberg (2007)
- D. J. Gross and F. Wilczek, *Ultraviolet Behavior of Non-Abelian Gauge Theories*, Phys. Rev. Lett. 30, 1343 (1973)
- S. S. Gubser, *Symmetry constraints on generalizations of Bjorken flow*, Phys. Rev. D 82, 085027 (2010)
- S. S. Gubser and A. Yarom, *Conformal hydrodynamics in Minkowski and de Sitter spacetimes*, Nucl. Phys. B 846, 469 (2011)
- S. W. Herb et al. (E288 Collaboration), *Observation of a Dimuon Resonance at 9.5 GeV in 400-GeV Proton-Nucleus Collisions*, Phys. Rev. Lett. 39, 252 (1977)
- A. Hujerir, M. Camenzind and B. W. Keil, *An implicit numerical algorithm for solving the general relativistic hydrodynamical equations around accreting compact objects*, New Astron. 13, 436 (2008)
- S. Jacobs, M. G. Olsson and C. Suchyta, III, *Comparing the Schrödinger and spinless Salpeter equations for heavy-quark bound states*, Phys. Rev. D 33, 3338 (1986)
- O. Kaczmarek and F. Zantow, *Static quark anti-quark interactions in zero and finite temperature QCD. I. Heavy quark free energies, running coupling and quarkonium binding*, Phys. Rev. D 71, 114510 (2005)
- J. I. Kapusta, *Finite-temperature field theory*, Cambridge University Press, Cambridge (1989)
- F. Karsch, M. T. Mehr and H. Satz, *Color screening and deconfinement for bound states of heavy quarks*, Z. Phys. C 37, 617 (1988)
- V. Khachatryan et al. (CMS Collaboration),  *$\Upsilon$  production cross section in pp collisions at  $\sqrt{s} = 7$  TeV*, Phys. Rev. D 83, 112004 (2011)

- D. E. Kharzeev, *Theoretical issues in  $J/\psi$  suppression*, J. Phys. G 34, 445 (2007)
- T. Kind, *Transverse expansion of the quark-gluon plasma in PbPb collisions at LHC energies*, B.Sc. Thesis, University of Heidelberg (2013)
- L. Kluberg and H. Satz, *Color Deconfinement and Charmonium Production in Nuclear Collisions*, Landolt-Börnstein I 23, 373 (2010)
- M. Laine, O. Philipsen, M. Tassler and P. Romatschke, *Real-time static potential in hot QCD*, J. High Energy Phys. 3, 54 (2007)
- J.-P. Lansberg,  *$J/\psi$ ,  $\psi'$  and  $\Upsilon$  Production at Hadron Colliders: a Review*, Int. J. Mod. Phys. A 21, 3857 (2006)
- M. Le Bellac, *Thermal Field Theory*, Cambridge University Press, Cambridge (2000)
- Y. Liu, C. M. Ko and T. Song, *Gluon dissociation of  $J/\psi$  beyond the dipole approximation*, arXiv1307.4427 (2013)
- L. Manceau (ALICE Collaboration), *Quarkonium measurements in Pb-Pb and p-Pb collisions with ALICE at the LHC*, arXiv:1307.3098 (2013)
- T. Matsui and H. Satz,  *$J/\psi$  Suppression by Quark-Gluon Plasma Formation*, Phys. Lett. B 178, 416 (1986)
- C. W. Misner, K. S. Thorne and J. A. Wheeler, *Gravitation*, W.H. Freeman and Co., New York (1973)
- K. Nakamura et al. (Particle Data Group), *Review of Particle Physics*, J. Phys. G 37, 075021 (2010)
- F. Nendzig and G. Wolschin,  *$\Upsilon$  suppression in PbPb collisions at energies available at the CERN Large Hadron Collider*, Phys. Rev. C 87, 024911 (2013)
- Y. Park, K.-I. Kim, T. Song, S. H. Lee and C.-Y. Wong, *Widths of quarkonia in quark gluon plasma*, Phys. Rev. C 76, 044907 (2007)
- B. K. Patra and D. K. Srivastava,  *$J/\psi$  suppression: gluonic dissociation vs. colour screening*, Phys. Lett. B 505, 113 (2001)
- M. Peskin and D. Schroeder, *An Introduction To Quantum Field Theory*, Westview Press, Boulder (1995)

- M. E. Peskin, *Short-distance analysis for heavy-quark systems (I). Diagrammatics*, Nucl. Phys. B 156, 365 (1979)
- A. Pineda and J. Soto, *Effective field theory for ultrasoft momenta in NRQCD and NRQED*, Nucl. Phys. B (Proc. Suppl.) 64, 428 (1998)
- H. D. Politzer, *Reliable Perturbative Results for Strong Interactions?*, Phys. Rev. Lett. 30, 1346 (1973)
- W. H. Press, S. A. Teukolsky, W. T. Vetterling and B. P. Flannery, *Numerical recipes in C++ : the art of scientific computing*, Cambridge University Press, New York (2002)
- K. Reygers (ALICE Collaboration), *A Quick Tour of Ultra-Relativistic Heavy-Ion Physics at the LHC*, arXiv:1208.1626v1 (2012)
- C. Silvestre et al. (CMS Collaboration), *Quarkonia measurements by the CMS experiment in pp and Pb-Pb collisions*, J. Phys. G 38, 124033 (2011)
- T. Song, K. C. Han and C. M. Ko, *Charmonium production in relativistic heavy-ion collisions*, Phys. Rev. C 84, 034907 (2011)
- T. Song, K. C. Han and C. M. Ko, *Bottomonia suppression in heavy-ion collisions*, Phys. Rev. C 85, 014902 (2012)
- T. Song and S. H. Lee, *Quarkonium-hadron interactions in perturbative QCD*, Phys. Rev. D 72, 034002 (2005)
- M. A. Srednicki, *Quantum Field Theory*, Cambridge University Press, Cambridge (2007)
- M. Strickland, *Thermal  $\Upsilon(1s)$  and  $\chi_{b1}$  suppression in  $\sqrt{s_{NN}} = 2.76$  TeV Pb-Pb collisions at the LHC*, Phys. Rev. Lett. 107, 132301 (2011)
- M. Strickland and D. Bazow, *Thermal Bottomonium Suppression at RHIC and LHC*, Nucl. Phys. A 879, 25 (2012)
- G. 't Hooft, *The birth of asymptotic freedom*, Nucl. Phys. B 254, 11 (1985)
- F. Vaccaro, *The influence of the  $\chi_b(3P)$  state on the decay cascade of the  $\Upsilon$  meson in PbPb collisions at LHC energies*, B.Sc. Thesis, University of Heidelberg (2013)
- F. Vaccaro, F. Nendzig and G. Wolschin, *The influence of the  $\chi_b(3P)$  state on the decay cascade of bottomium in PbPb collisions at LHC energies*, Europhys. Lett. 102, 42001 (2013)

- K. G. Wilson, *Confinement of quarks*, Phys. Rev. D 10, 2445 (1974)
- K. Yagi, T. Hatsuda and Y. Miake, *Quark-Gluon Plasma*, Cambridge University Press, Cambridge (2008)
- X. Zhao and R. Rapp, *Charmonium in Medium: From Correlators to Experiment*, Phys. Rev. C 82, 064905 (2010)
- X. Zhao and R. Rapp, *Medium modifications and production of charmonia at LHC*, Nucl. Phys. A 859, 114 (2011)